NUMERICAL SIMULATION OF MULTIPHASE FLOWS IN MICROCHANNELS USING THE LATTICE BOLTZMANN METHOD

by
Luz Amaya-Bower

A dissertation submitted to the Graduate Faculty in Mechanical Engineering in partial fulfillment of the requirements for the degree of Doctor of Philosophy,
The City University of New York
2010

This manuscript has been read and accepted for the Graduate Faculty in Mechanical Engineering in satisfaction of the dissertation requirement for the degree of Doctor of Philosophy.

8/12/2010	**Prof. Taehun Lee**
Date	Prof. Taehun Lee, Chair of Examining Committee
8/12/2010	**Dean Mumtaz Kassir**
Date	Dean Mumtaz Kassir, Executive Officer

Prof. Shahriar Afkhami

Prof. Masahiro Kawaji

Prof. Jeff Morris

Prof. Charles B. Watkins

Supervisory Committee

THE CITY UNIVERSITY OF NEW YORK

Abstract

by
Luz Amaya-Bower
Adviser: Professor Taehun Lee

Dynamics of multiphase systems in micro-fluidic devices is a topic of great interest in many industrial applications such as chemical synthesis, DNA analysis, enhanced micromixing, and power generation. Due to the small transverse dimensions, microchannels provide a great surface to volume ratio, offering an enhanced heat and transfer efficiency. In addition, they provide a great alternative for many chemical reactions by minimizing the amount of reactants needed. Different from large scale channels, bubbles can create significant problems in micro-fluidic devices by altering or blocking the flow. On the other hand, controllable addition of bubbles is desired to improve mixing and heat transfer in microsystems. Therefore it is important to understand clearly the dynamic behavior of multiphase systems, from the point of formation to transport along the microchannel. Bubble formation dynamics is governed by the set-up geometry and ratio between interfacial and viscous forces in the system. Multiphase flow transport along microchannel is determined by wall surface wettability, initial fluid conditions, and velocities. A stable Lattice Boltzmann Method (LBM) based on the Cahn-Hilliard diffuse interface approach is used for the

simulation of bubble formation and motion along the microchannel. Initial validation of the model is presented for the dynamics of a single bubble rising in unconfined and confined domains.

Acknowledgments

I would like to thank first God, for allowing me to get this far and being with me every step of the way. Even though it is impossible to mention all the people that have helped me in this process, I must say that I am eternally grateful for their support and encouragement. I would like to extent my gratitude to my mentor, Dr. Taehun Lee for his words of advice and wisdom. Thank you for showing me the way to achieve my goals to the best of my abilities. To those professors who have helped me accomplish this work with financial and intellectual support: Dr. Jeffrey Morris, Dr. Yiannis Andreopoulos, Dr. Charles B. Watkins, Dr. Masahiro Kawaji, and Prof. Gary Benenson. To all my family and friends who have gone above and beyond to help me to reach this point in my life. To my parents, Alonso and Susy, for teaching me that the important things in life are obtained by perseverance and hard work. To my brother Javier, for his unconditional love and advice. To my best friend and sister Karla, for showing me the path of success. To the Martinez family for giving me a home and enduring the difficult times. Finally, to my husband Kris, who provides me with the strength and the laughter to take the challenges every day.

Contents

Abstract **iv**

Acknowledgments **vi**

1 Nomenclature **1**

2 Introduction **6**

2.1 Applications 7

2.1.1 Chemical Synthesis: Colloidal Silica 7

2.1.2 Monolith Reactors 9

2.1.3 Microencapsulation 9

2.2 CFD Models for Multiphase Microsystems 10

2.2.1 Mixing Area 11

2.2.2 Segregated Flow Area 16

3 Motivation and Objectives **19**

4 Lattice Boltzmann Method **22**

4.1 Diffuse Interface - Cahn-Hilliard Model 28

4.2 Wetting Phenomena and Contact Angles 29

5 Single Bubble Rising in Unconfined Domain **31**

5.1 Background 31

5.2 Numerical Method Validation 35

5.2.1 Grid Resolution Dependence 35

5.2.2 Domain Size Dependence 36
5.2.3 Density Ratio Dependence 38
5.2.4 Viscosity Ratio Dependence 41
5.2.5 Interface Thickness Dependence 42
5.2.6 Surface Tension Dependence 44
5.2.7 Application of Buoyancy Force Dependence 45
5.3 Numerical Results 46
5.3.1 Terminal Velocity and Shape 47
5.3.2 Comparison with Correlation 63

6 Single Bubble Rising in a Square Channel 66
6.1 Background 66
6.2 Test Cases and Computational Setup 69
6.3 Validation: Comparison with Experimental Results 72
6.4 Final Shape 73
6.4.1 Final Shape vs. Bo 80
6.4.2 Film Thickness vs. k 80
6.4.3 Deformation Parameter vs. k 82
6.5 Streamlines and Vorticity Contours 82
6.6 Pressure Contours 93
6.7 Inclined Channel 94
6.7.1 Final Shape 94
6.7.2 Velocity vs. Inclination 98
6.7.3 Streamlines and Vorticity Contours 98
6.7.4 Pressure Contours 103

7 Formation Process in a Microchannel 105
7.1 Background 105
7.2 Simulation Set Up 107
7.3 Validation Test 108
7.3.1 Grid Resolution 109
7.3.2 Domain Size 110

7.3.3 Density Ratio . . . 111
7.3.4 Contact Angle . . . 113
7.4 Comparison to Experimental Results . . . 116
7.4.1 Formation Process . . . 116
7.4.2 Evolution of W_m . . . 118
7.4.3 Final shape and Dimension of Bubble . . . 118
7.5 Numerical Results . . . 119
7.5.1 Droplet Formation . . . 120
7.5.2 Bubble Formation . . . 126
7.6 $3D$ Results . . . 131
7.6.1 Droplet Formation . . . 133
7.6.2 Bubble Formation . . . 134

8 Summary and Future Work **137**
8.1 Summary . . . 137
8.2 Future Work . . . 141

A Modified Particle Distribution Functions **143**

B Discretization of First and Second Derivatives **144**
B.1 $D2Q9$ Model . . . 144
B.2 $D3Q19$ Model . . . 145

Bibliography **146**

List of Tables

5.1 Values of Bo and Mo. 49
5.2 Comparison of 3D Simulation results and experimental results based on the study by Bhaga and Weber [53]. 49
5.3 Comparison of 3D Simulation results and previous simulation results based on Hua *et al.* [65, 72] and Bonometti and Magnaudet [74]. . . . 50
5.4 Comparison of 3D simulation terminal Re results with different viscosity ratios. 51

6.1 Values of Bo, Mo and density ratio in each case from experimental study by Li *et al.* [99]. 70

List of Figures

2.1 Mixing geometries. 7
2.2 LFR and SFR schematics [7]. 8
2.3 Circular and rectangular monolithic structures. 9
2.4 Design of drop-based microfluidic device for encapsulating single cells [10]. 10
2.5 Influence of Ca on flow patterns. 12
2.6 Comparison between simulation and experiment [18]. 12
2.7 Gas-liquid velocity ratio comparison [23]. 14
2.8 Inlet tee size comparison [23]. 14
2.9 Tee orientations comparison [23]. 15
2.10 Contact angle comparison [26]. 16
2.11 Hydrophillic flow regimes [27]. 17
2.12 Hydrophobic flow regimes [27]. 18
2.13 Slug rising at different Ca [29]. 18

4.1 Lattice models. 24
4.2 Interfacial tension acting on contact line. 29

5.1 Shape regime map [52]. 33
5.2 Effect of grid resolution on terminal shape at $T = 10$. 36
5.3 Effect of grid resolution on terminal Re. 37
5.4 Effect of radial domain size on terminal shape at $T = 10$. 38
5.5 Effect of radial domain size on terminal Re. 39
5.6 Effect of density ratio on terminal Re. 39
5.7 Effect of density ratio on terminal shape at $T = 10$. 40

5.8 Effect of viscosity ratio on terminal Re. 41
5.9 Effect of viscosity ratio on terminal shape at $T = 10$. 42
5.10 Effect of interface thickness on terminal Re at $T = 10$. 43
5.11 Effect of interface thickness on terminal shape at $T = 10$. 44
5.12 Dimensionless error as function of U_y with different interface thicknesses D at $50,000$ iterations. Domain size is 100×100, bubble radius $d_0 = 50$, $\rho_l = 1.0$, $\rho_g = 0.1$, $\tau_l = 0.5$ and $\tau_g = 0.5$. 45
5.13 Effect of surface tension on terminal shape at $T = 10$. 46
5.14 Effect of the method of application of buoyancy force at $T = 4.5$. . . 47
5.15 Shape regime map for bubbles in liquids: S, spherical; OE, oblate ellipsoid; OED, oblate ellipsoidal (disk-like and wobbling); OEC, oblate ellipsoidal cap; SCC, spherical cap with closed, steady wake; SCO, spherical cap with open, unsteady wake; SKS, skirted with smooth, steady skirt; SKW, skirted with wavy, unsteady skirt [53]. 48
5.16 Shape and position evolution for cases A and B. 52
5.17 Shape and position evolution for cases C and D. 53
5.18 Shape and position evolution for cases E and F. 54
5.19 Shape and position evolution for cases G and H. 54
5.20 Streamlines for cases A and B. 55
5.21 Streamlines for cases C and D. 56
5.22 Streamlines for cases E and F. 57
5.23 Streamlines for cases G and H. 57
5.24 Pressure contours for case A. P_{tot} is total pressure, P is the sum of static and dynamic part, p_0 is the thermodynamic part, and p_c is the curvature part. 59
5.25 Pressure contours for case B. P_{tot} is total pressure, P is the sum of static and dynamic part, p_0 is the thermodynamic part, and p_c is the curvature part. 59
5.26 Pressure contours for case C. P_{tot} is total pressure, P is the sum of static and dynamic part, p_0 is the thermodynamic part, and p_c is the curvature part. 60

5.27 Pressure contours for case D. P_{tot} is total pressure, P is the sum of static and dynamic part, p_0 is the thermodynamic part, and p_c is the curvature part. 60
5.28 Pressure contours for case E. P_{tot} is total pressure, P is the sum of static and dynamic part, p_0 is the thermodynamic part, and p_c is the curvature part. 61
5.29 Pressure contours for case F. P_{tot} is total pressure, P is the sum of static and dynamic part, p_0 is the thermodynamic part, and p_c is the curvature part. 61
5.30 Pressure contours for case G. P_{tot} is total pressure, P is the sum of static and dynamic part, p_0 is the thermodynamic part, and p_c is the curvature part. 62
5.31 Pressure contours for case H. P_{tot} is total pressure, P is the sum of static and dynamic part, p_0 is the thermodynamic part, and p_c is the curvature part. 62
5.32 Drag coefficient comparison between experimental results from Bhaga and Weber [53] and simulation results. 63
5.33 Comparison of velocity number for simulation results and correlation [76]. 64

6.1 Effect of channel length on non-dimensional parameters in (a) film thickness δ and (b) deformation parameter Δ at $T = 10$ for case *GW1-1*. The channel lengths are $10R_c$, $15R_c$, $20R_c$ and $30R_c$. 71
6.2 Effect of grid resolution on final shape at T = 10 for case *SO4* at inclination of 75°. 72
6.3 Comparison of the final shapes between the LBE simulations and the experimental results by Li *et al.* [99] for four cases (a) *GW2-2*, (b) *GW3-2*, (c) *GW4-2*, and (d) *SO4*. The upper rows present the LBE simulations and the lower rows the experimental results. 74
6.4 Comparison of non-dimensional parameters (a) film thickness δ and (b) deformation parameter Δ between the LBE simulations and the experimental results by Li *et al.* [99] for cases *GW2-2* and *GW4-2*. . . 75

6.5 Simulation results for final shape at $T = 10$ and for $k = 0.6$ for all cases organized in three groups. (a) *GW-1*, (b) *GW-2*, and (c) *SO*. . . 76
6.6 Simulation results for final shape at $T = 10$ and $k = 0.8$ for all cases organized in three groups. (a) *GW-1*, (b) *GW-2*, and (c) *SO*. 77
6.7 Simulation results for final shape at $T = 10$ and $k = 1.05$ for all cases organized in three groups. (a) *GW-1*, (b) *GW-2*, and (c) *SO*. 78
6.8 Simulation results for final shape at $T = 10$ and $k = 1.25$ for all cases organized in three groups. (a) *GW-1*, (b) *GW-2*, and (c) *SO*. 79
6.9 Effect of Bo on final shape at $T = 10$ for cases two cases (a) *GW2* and (b) *GW3*. 81
6.10 Evolution of film thickness δ as function of k for all cases organized in three groups. (a) *GW-1*, (b) *GW-2*, and (c) *SO*. 83
6.11 Evolution of deformation parameter Δ as function of k for all cases organized in three groups. (a) *GW-1*, (b) *GW-2*, and (c) *SO*. 84
6.12 Streamlines in the XY plane at $T = 10$ for all cases organized in three groups. (a) *GW-1*, (b) *GW-2*, and (c) *SO*. 85
6.13 Streamlines and vorticity contours in the XZ plane at four elevations for cases two cases, the upper row presents case *GW1-1* and the lower row case *GW2-1*. 87
6.14 Streamlines and vorticity contours in the XZ plane at four elevations for cases two cases, the upper row presents case *GW3-1* and the lower row case *GW2-2*. 88
6.15 Streamlines and vorticity contours in the XZ plane at four elevations for cases two cases, the upper row presents case *GW3-2* and the lower row case *GW4-2*. 89
6.16 Streamlines and vorticity contours in the XZ plane at four elevations for cases two cases, the upper row presents case *GW5-2* and the lower row case *SO2*. 90
6.17 Streamlines and vorticity contours in the XZ plane at four elevations for cases two cases, the upper row presents case *SO3* and the lower row case *SO4*. 91

6.18 Streamlines and vorticity contours in the XZ plane at four elevations for cases two cases, the upper row presents case *SO5* and the lower row case *SO6*. 92
6.19 Pressure contours: P_{tot} is the total pressure, P is the sum of static and dynamic part, p_0 is the thermodynamic part, and p_c is the curvature part. 95
6.20 Final shape at $T = 10$ for different inclination angles for cases *SO2*, *SO3* and *SO4*. 97
6.21 Effect of inclination angle on non-dimensional parameters for cases *SO2*, *SO3* and *SO4*. 98
6.22 Effect of inclination angle on Fr for cases *SO2*, *SO3* and *SO4*. 99
6.23 Streamlines in the XY plane at $T = 10$ for case *SO3* at inclination angles 30°, 45°, 60°,a 75°. 100
6.24 Streamlines and vorticity contours in the XZ plane at four elevations for case *SO3*, the upper row presents inclination angle 30° and the lower row 45°. 101
6.25 Streamlines and vorticity contours in the XZ plane at four elevations for case *SO3*, the upper row presents inclination angle 60° and the lower row 75°. 102
6.26 Pressure contours: P_{tot} is the total pressure, P is the sum of static and dynamic part, p_0 is the thermodynamic part, and p_c is the curvature part. 103

7.1 $2D$ Schematic diagram of T-junction. v_d and v_c are the mean velocities of the dispersed and continuous liquid respectively. η_d and η_c are the dynamic viscosities and ρ_d and ρ_c are the densities. 108
7.2 Graphical representation of W_m and L_{bu}. 109
7.3 Effect of grid resolution on terminal shape for $Ca = 0.005$, $Q = 0.8$, and $\lambda = 1$, $\theta_{eq} = 30°$ at $T = 12$. 110
7.4 Effect of grid resolution on the evolution of L_{bu} and W_m for $Ca = 0.005$, $Q = 0.8$, $\lambda = 1$, and $\theta_{eq} = 30°$ at $T = 12$. 111

7.5 Effect of domain size on terminal shape for $Ca = 0.005$, $Q = 0.8$, $\lambda = 1$, and $\theta_{eq} = 30°$ at $T = 12$. 112
7.6 Effect of domain size on the evolution of L_{bu} and W_m for $Ca = 0.005$, $Q = 0.8$, $\lambda = 1$, and $\theta_{eq} = 30°$ at $T = 12$. 112
7.7 Effect of density ratio on terminal shape. 114
7.8 Effect of contact angle θ_{eq} on bubble terminal shape for $\theta_{eq} = 30°$, $\theta_{eq} = 60°$, $\theta_{eq} = 90°$, $\theta_{eq} = 120°$, and $\theta_{eq} = 150°$ with $Ca = 0.005$, $Q = 0.8$, $\rho_{ratio} = 0.001$, and $\lambda = 1$ at $T = 15$. 115
7.9 Effect of contact angle θ_{eq} on bubble terminal shape for $\theta_{eq} = 30°$, $\theta_{eq} = 90°$ and $\theta_{eq} = 150°$ with $Ca = 0.005$, $Ca = 0.01$, and $Ca = 1$. $Q = 0.8$, $\rho_{ratio} = 0.001$, and $\lambda = 1$ at $T = 15$. 115
7.10 Effect of contact angle θ_{eq} on droplet terminal shape for $\theta_{eq} = 30°$, $\theta_{eq} = 90°$ and $\theta_{eq} = 150°$ with $Ca = 0.005$, $Ca = 0.05$, and $Ca = 0.5$. $Q = 0.25$ and $\lambda = 1$ at $T = 12$. 116
7.11 Comparison of shape in the formation process for ethanol and air and $Q = 1.5$. Top row presents the simulation results and lower row are experimental results by van Steijn *et al.* [118]. 117
7.12 Comparison of velocity field in the formation process for ethanol and air and $Q = 1.5$. Top presents the simulation results and lower row are experimental results by van Steijn *et al.* [118]. 118
7.13 Comparison of evolution of W_m for experimental results by van Steijn *et al.* [118] and simulated results for ethanol and air and $Q = 1.5$. . . 119
7.14 Effect of Ca on droplet formation for $Ca = 0.5$, $Ca = 0.1$, $Ca = 0.05$, $Ca = 0.01$, and $Ca = 0.005$ with $Q = 0.25$, $\lambda = 1$, and $\theta_{eq} = 150°$ at $T = 7.5$. 121
7.15 Effect of Ca on (a) T_p and (b) D_p for cases in the dripping regime with $Q = 0.25$, $\lambda = 1$ and $\theta_{eq} = 150°$. 122
7.16 Effect of Ca on (a) W_m and (b) L_{dr}/H for cases in the dripping regime with $Q = 0.25$, $\lambda = 1$ and $\theta_{eq} = 150°$. 122

7.17 Effect of Q on droplet formation for $Q = 0.25$ and $Q = 2.5$ with $Ca = 0.005$, $Ca = 0.01$, $Ca = 0.05$, $Ca = 0.1$, and $Ca = 0.5$ for $\lambda = 1$, and $\theta_{eq} = 150°$ at $T = 7.5$. 123
7.18 Droplet formation for $Ca = 0.005$, $Ca = 0.01$, $Ca = 0.05$, $Ca = 0.1$, and $Ca = 0.5$. $Q = 0.25$, $\lambda = 0.5$, and $\theta_{eq} = 150°$ at $T = 7.5$. 125
7.19 Effect of λ on (a) T_p and (b) D_p for cases in the dripping regime with $Q = 0.25$, $\lambda = 1$ and $\theta_{eq} = 150°$. 125
7.20 Effect of λ on (a) W_m and (b) L_{dr}/H for cases in the dripping regime with $Q = 0.25$, $\lambda = 1$ and $\theta_{eq} = 150°$. 126
7.21 Effect of Ca on bubble formation for $Ca = 1.0$, $Ca = 0.5$, $Ca = 0.1$, $Ca = 0.01$, and $Ca = 0.005$ with $Q = 1.0$, $\lambda = 0.02$, $\rho_{ratio} = 0.001$, and $\theta_{eq} = 30°$ at $T = 18.0$. 127
7.22 Effect of Q on bubble formation in the squeezing regime for $Q = 0.5$, $Q = 1.5$, $Q = 3.0$, and $Q = 4.5$ with $Ca = 0.005$, $\lambda = 0.02$, $\rho_{ratio} = 0.01$, and $\theta_{eq} = 30°$ at $T = 18.0$. 128
7.23 Effect of Q on the non-dimensional length of the bubble in the squeezing regime with $Ca = 0.005$, $\lambda = 0.02$, $\rho_{ratio} = 0.01$, and $\theta_{eq} = 30°$ at $T = 18.0$. 128
7.24 Effect of Q on bubble formation in the dripping regime for $Q = 0.3$, $Q = 0.5$, $Q = 1.0$, and $Q = 3.0$ with $Ca = 0.05$, $\lambda = 0.02$, $\rho_{ratio} = 0.01$, and $\theta_{eq} = 30°$ at $T = 18.0$. 129
7.25 Effect of Q on bubble formation in the jetting regime for $Q = 0.3$, $Q = 0.5$, $Q = 1.0$, and $Q = 3.0$ with $Ca = 0.5$, $\lambda = 0.02$, $\rho_{ratio} = 0.01$, and $\theta_{eq} = 30°$ at $T = 18.0$. 129
7.26 Effect of λ on bubble formation in the squeezing regime for $\lambda = 1.0$, $\lambda = 0.1$, $\lambda = 0.05$, and $\lambda = 0.02$ with $Ca = 0.005$, $Q = 0.5$, $\rho_{ratio} = 0.001$, and $\theta_{eq} = 30°$ at $T = 18.0$. 130
7.27 Effect of λ on bubble formation in the dripping regime for $\lambda = 1.0$, $\lambda = 0.1$, $\lambda = 0.05$, and $\lambda = 0.02$ with $Ca = 0.05$, $Q = 0.3$, $\theta_{eq} = 30°$ at $T = 18.0$. 131

7.28 Effect of λ on bubble formation in the dripping regime for $\lambda = 1.0$, $\lambda = 0.1$, $\lambda = 0.05$, and $\lambda = 0.02$ with $Ca = 0.05$, $Q = 0.5$, $\theta_{eq} = 30°$ at $T = 18.0$. 132
7.29 Effect of λ on bubble formation in the jetting regime for $\lambda = 1.0$, $\lambda = 0.1$, $\lambda = 0.05$, and $\lambda = 0.02$ with $Ca = 0.5$, $Q = 0.3$, $\theta_{eq} = 30°$ at $T = 18.0$. 132
7.30 Effect of λ on bubble formation in the jetting regime for $\lambda = 1.0$, $\lambda = 0.1$, $\lambda = 0.05$, and $\lambda = 0.02$ for $Ca = 0.5$, $Q = 0.5$, $\theta_{eq} = 30°$ at $T = 18.0$. 133
7.31 $3D$ Simulation for droplet formation for $Ca = 0.5$, $\lambda = 1$, $Q = 0.25$, and $\theta_{eq} = 30°$. 134
7.32 $3D$ Simulation for droplet formation for $Ca0.005$, $\lambda = 1$, $Q = 0.25$, and $\theta_{eq} = 30°$. 134
7.33 $3D$ Simulation for bubble formation at $Ca = 1.0$, $\lambda = 1$, $Q = 1.0$, and $\theta_{eq} = 30°$. 135
7.34 $3D$ Simulation for bubble formation at $Ca = 0.01$, $\lambda = 1$, $Q = 1.0$, and $\theta_{eq} = 30°$. 135
7.35 $3D$ Simulation for bubble formation at $Ca = 0.005$, $\lambda = 1$, $Q = 1.0$, and $\theta_{eq} = 30°$. 136

Chapter 1

Nomenclature

a	Radius of the spherical bubble
A	Cross-sectional area normal to the bubble motion
a_1	Constant
b_1	Constant
Bo	Bond number defined as $Bo = \frac{g(\rho_l - \rho_g)R_c^2}{\sigma}$
C	Composition
Ca	Capillary number defined as $Ca = \frac{\eta_l U_t}{\sigma}$
Cn	Cahn number defined as $Cn = D/d_0$
C_d	Drag coefficient
c_s	Speed of sound
C_s	Composition at a solid surface
c_1	Constant
D	Numerical interface thickness
D_h	Hydraulic diameter
D_p	Pinch-off distance
d_1	Constant
$E(U_y)$	Dimensionless error as function of vertical velocity
d_0	Initial diameter of bubble
E_{mix}	Mixing energy density
E_0	Bulk energy

$\mathbf{e}_\alpha$	Microscopic particle velocity
$\mathbf{F}$	Averaged external force
F	Flow number
Fr	Froude number defined as $Fr = U_t\sqrt{\frac{\rho}{2R_c g(\rho_l-\rho_g)}}$
F_{bu}	Buoyancy force
F_{dr}	Drag force
f_α	Original particle distribution function to recover mass and momentum
g_α	Original particle distribution function to recover pressure and momentum
h_α	Original particle distribution function to recover composition
$\bar{g}_\alpha$	Modified particle distribution function to recover pressure and momentum
$\bar{h}_\alpha$	Modified particle distribution function to recover composition
f_α^{eq}	Original equilibrium function related to f_α
g_α^{eq}	Original equilibrium function related to g_α
h_α^{eq}	Original equilibrium function related to h_α
$\bar{g}_\alpha^{eq}$	Modified equilibrium distribution function related to $\bar{g}_\alpha$
$\bar{h}_\alpha^{eq}$	Modified equilibrium distribution function related to $\bar{h}_\alpha$
g	Gravitational acceleration
$\mathbf{G}$	Gravitational force defined as $\mathbf{G} = -\rho g \nabla h$
GW	Glycerine solution
h	Elevation from a reference point
H	Width of channel
I	Non-dimensional inertia defined as $I = Re/Ca$
I_c	Critical non-dimensional inertia
$\mathbf{J}$	Diffusive flow rate
k	Non-dimensional size of the bubble defined as $k = \frac{a}{R_c}$
L	Length of the channel
L_{bu}	Length of the bubble
L_{dr}	Length of the droplet
M	Mobility
Ma	Mach number
Mo	Morton number defined as $Mo = \frac{g(\rho_l-\rho_g)\eta_l^4}{\sigma^3\rho_l^2}$

$\mathbf{n}$	Unit normal vector
P	Sum of the dynamic and static parts of pressure
p_0	Thermodynamic pressure
p_1	Hydrodynamic pressure
p_c	Pressure due to curvature
P_{tot}	Total pressure
P_{top}	Pressure at highest point in the domain
P_{btop}	Pressure at highest point in the bubble
Q	Volumetric flow ratio defined as $Q = Q_d/Q_c$
R_c	Characteristic length
$R_{h,v}$	Horizontal and vertical radii of moving bubble
Re	Reynolds number defined as $Re = \frac{\rho_l U_t d_0}{\eta_l}$
SO	Sodium iodide solutions
t	Time
T	Non-dimensional time defined as $T = t/t_{n1,n2,n3}$
T_c	Formation time for a cycle
t_{n1}	Simulation time defined as $t_{n1} = \sqrt{d_0/g}$
t_{n2}	Simulation time defined as $t_{n2} = \sqrt{R_c/g}$
t_{n3}	Simulation time defined as $t_{n3} = H/v_d$
t_α	Weighting factor for the $D3Q19$ model
T_p	Pinch-off time
$\mathbf{u}$	Macroscopic velocity
U_t	Steady terminal velocity
U_{c1}	Characteristic velocity defined as $U_{c1} = \sqrt{gd_0}$
U_{c2}	Characteristic velocity defined as $U_{c2} = \sqrt{gR_c}$
v	Mean velocity
V	Velocity number
W	Width of the channel
W_{bu}	Width of the bubble
W_m	Maximum width of dispersed fluid stream
We	Weber number defined as $We = \frac{\rho_l U_t^2 R_c}{\sigma}$

x	Space coordinate
y	Space coordinate
Y1-Y4	Location Markers
z	Coordinate normal to the plane interface

Greek letters

α	Lattice direction
$\alpha_{1,2}$	Constants
β	Constant
$\Gamma_\alpha(\mathbf{u})$	Function defined as f_α^{eq}/ρ
δ	Film thickness
Δ	Deformation parameter
δt	Time step
η	Mixture viscosity
θ	Inclination angle
θ_{eq}	Equilibrium contact angle
κ	Gradient parameter
λ	Viscosity ratio defined as $\lambda = \eta_d/\eta_c$
λ_1	Viscosity ratio defined as $\lambda_1 = \eta_l/\eta_g$
λ_r	Relaxation time
μ	Chemical potential
μ_0	Classical part of the chemical potential
ρ	Mixture density
ρ_{ave}	Average density
σ	Surface tension
τ	Dimensionless relaxation time
ϕ_c	Constant
ϕ_i	Constant coefficients

Subscripts

b	Bulk
c	Continuous fluid
d	Dispersed fluid
exp	Experimental Results
g	Gas
l	Liquid
s	Solid surface
sim	Simulation Results
V	Volume

Chapter 2

Introduction

Recently, there has been a growing interest in microscale systems in industrial applications which is mainly driven by reduction of cost, and increase of safety and efficiency. The use of two immiscible fluids in microchannel geometries has become a growing topic of interest in many industrial applications such as chemical processing, biomedical analysis, and material science in order to improve and extend the performance of single phase microsystems [1, 2, 3]. Introduction of a secondary immiscible fluid, creates new recirculation patterns, larger interfaces, and additional eddies, which improve reactants mixing and transverse channel transport. In addition, introduction of a secondary flow will also allow reduction of common single-phase flow issues, such as long diffusion times and axial dispersion. In principle, mixing in small spaces is based on two phenomena: diffusion and convection [4]. Initially diffusion was most frequently applied, taking advantage of reduction of distances and creating high concentration gradients. However, due to micro-manufacturing limitations and robustness issues, diffusion had its limits. Therefore, introduction of a secondary flow, a convective flow, improves mixing by the principle that it creates larger mixing interfaces. The most important factors that determine the type of flow that will be generated in a microchannel are the mixing geometry and fluid properties at inlet conditions.

Flow in a microchannel is divided into two equally important phenomena: development and transport of the flow. The development of the flow takes place at the

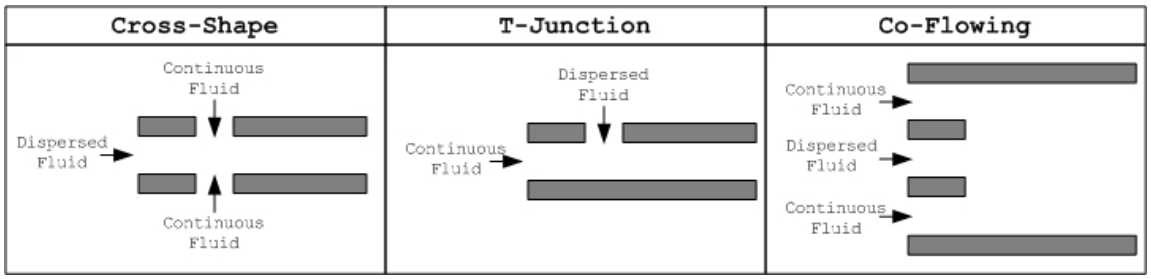

Figure 2.1: Mixing geometries.

mixing geometry section, where two fluids (continuous and dispersed) are introduced. Three of the most used mixing geometries are cross-shape, T-junction and co-flowing. A general configuration for each geometry is presented in Fig. 2.1. Once the flow is fully established, the transport of the flow takes place along the main channel. Dynamics of the flow along the microchannel is greatly dependent on the interaction between gas, liquid, and solid wall. This area is known as the segregated area, where the effect of wettability and contact angle would ultimately determine the behavior of the flow.

The following sections will introduce some of the applications and a review of the CFD models for multiphase flows in microfluidic devices.

2.1 Applications

In recent years there has been a significant progress in the development of microfluidic devices with applications in areas such as biochemical reactions [5], ultrasound imaging [6], chemical processing [1], biomedical analysis [2], material science [3], chemical synthesis [7], monolith reactors [8, 9], and microencapsulation [10]. A brief description of the last three applications will be provided in the following sections.

2.1.1 Chemical Synthesis: Colloidal Silica

Colloidal suspensions are used in many industrial applications, such as manufacturing of displays, optical coating, and photocatalyst support [7]. As many chemical compounds, their properties are direct result of the process to synthesize them. Synthesis

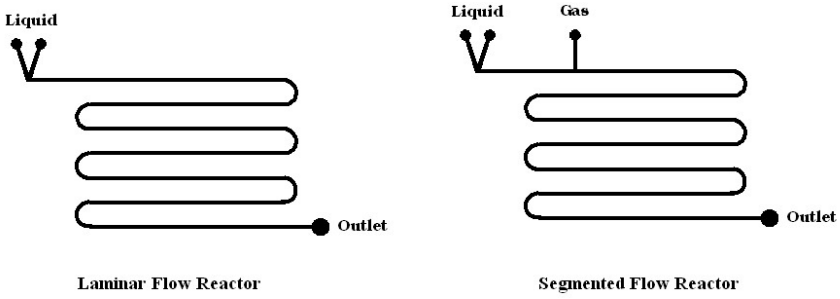

Figure 2.2: LFR and SFR schematics [7].

is usually performed using batch rectors. Two important advantages of these reactors are the flexibility and quality control. Batch reactors can be stopped, therefore providing flexibility in production to meet economical restrictions. In addition, each batch could have a different substance composition, providing a new specification in every process. Quality control can be performed by isolating a flaw to a specific batch, if needed. However, these reactors also have many disadvantages: due to their size, local concentration and temperature inhomogeneities can develop requiring constant stirring to maintain a homogeneous state. Moreover, their operating cost is very high. In recent years, reactors have been scaled down to microscales to provide a better control of size and composition of compound synthesis. Gas-liquid segmented flow microreactors are very useful because they can easily separate gas and liquid, dividing the liquid into small batches. Consequently, a more accelerated micromixing is achieved by taking advantage of small segments and recirculation.

In their study, Khan *et al.* [7], examined two different microfluidic reactor configurations for the synthesis of colloidal silica: Single-phase laminar flow reactor (LFR) and gas-liquid segmented flow reactor (SFR). A schematic of each reactor is given in Fig. 2.2

The evaluation of the reactors is mainly based on particle size distribution. For the laminar flow reactor design, uniform particle size is only feasible when flow conditions minimize axial dispersion. This is very difficult to accomplish, especially for low residence times. On the other hand, segmented flow reactors eliminate axial dispersion, producing monodisperse particle distribution. Their study concluded that gas-liquid

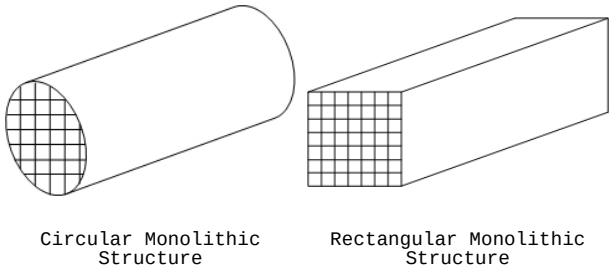

Figure 2.3: Circular and rectangular monolithic structures.

segmented flow reactors provide a great potential for the synthesis of colloidal silica and other chemicals.

2.1.2 Monolith Reactors

Chemical reactions frequently take place in packed-bed reactors. However, when the gas phase contains particulate matter, particles tend to clog the catalyst bed. In order to avoid this problem, parallel-plate reactors (monoliths) are used. A simplified schematic model of circular and rectangular monolith reactors is presented in Fig. 2.3. The reacting gas mixture flows between the parallel plates and the reaction takes place on the surface of the plates. Monolith reactors are particularly suitable for carrying out fast reactions in applications where space is limited. They also provide a novel and highly scalable solution to large-scale industrial applications. Monoliths were originally designed for single phase in the automobile catalyst converter, however a slug flow pattern was later introduced to enhance the mass transfer to the enzymes located at the channel walls. Currently monolith reactors are used in other areas such as hydrogenation reactions [11], selective catalytic reduction (SCR) to control power plant emissions [12], and environmental applications [13].

2.1.3 Microencapsulation

Microencapsulation is a process in which a particle is encased by a coat creating a capsule, in order to protect or immobilize the particle. This technique is widely

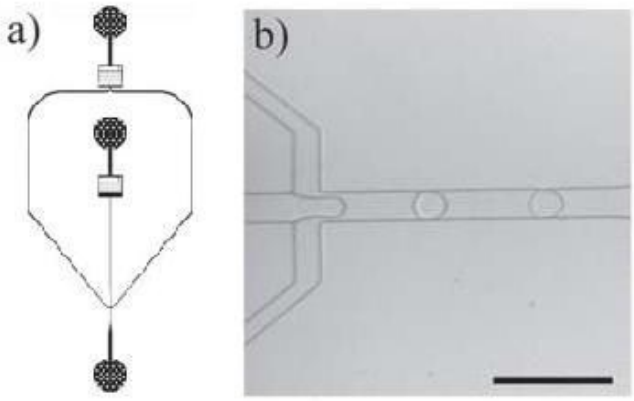

Figure 2.4: Design of drop-based microfluidic device for encapsulating single cells [10].

used in food, pharmaceutical, textile, and biomedical industries, see [10, 14, 15, 16]. An example in the food industry is taste masking, where an ingredient that has an unpleasant taste is encapsulated, so that the consumer can ingest it and take advantage of its benefits. In the biology field, microencapsulation is used to isolate single cells in order to gather statistical information of a large population of cells. This isolation is needed to avoid selection of cells based on the properties of the molecules they secrete, if there is no barrier against diffusion. Köster *et al.* [10] presented a drop-based microfluidic device which is used to encapsulate, incubate, and manipulate single cells in small drops. The device that is utilized for encapsulation is shown in Fig. 2.4. The flow focusing device to produce the drops is shown in (a). A closer look at the three inlet channels is presented in (b), where the middle channel contains cell suspension and the side channels the oil phase. Size and frequency of the drops are controlled by varying the overall flow rates.

2.2 CFD Models for Multiphase Microsystems

Simulation of microsystems could be divided in two main areas: Mixing area and segregated flow area. The following is a brief description of some CFD models that have been used to study each of these areas.

2.2.1 Mixing Area

Mixing geometry and fluid inlet conditions are the most important criteria to determine the type of flow that will be generated. Many experimental and numerical studies have been performed to establish a relationship between geometry, mass flow rate, and bubble dynamics. Three of the most used mixing geometries are cross-shape, T-junction and co-flowing. A general configuration for each geometry was previously presented in Fig. 2.1. The following sections introduce some of the numerical studies that have been performed for each geometry.

Cross-Shape Geometry

Cross-shape geometry produces a very stable and uniform flow. The gas coming from the horizontal channel forms an elongated bubble pinched off by the liquid coming perpendicularly. The size and the frequency of the bubble depend on the ratio of liquid and gas mass flow rates. Using this geometry Cubaud *et al.* [17] experimentally developed a two-phase transition map including five regimes (bubbly, wedging, slug, annular, and dry), providing transition criteria from one regime to the other based on flow rate ratio. Recently, Yu et at. [18] presented a numerical study on two-phase gas-liquid flows in microchannels using LBM. This model is based on a combination of models by Shan *et al.* [19], and Sankaranarayanan *et al.* [20]. This study establishes the importance of the capillary number (Ca), which is the ratio between viscosity and surface tension ($Ca = \frac{\eta v}{\sigma}$), in the flow patterns, especially in the break-up process and formation of bubbles. This confirms the experimental findings of Gunther *et al.* [21]. As capillary number decreases, the surface tension forces increases, therefore the bubble experiences less deformation. The influence of Ca can be seen on the simulation results by Yu *et al.* in Fig. 2.5.

Simulation results were compared to experimental studies. There was a significant difference between the results including break-up process, bubble shape, and bubble frequency. Authors believe that discrepancies are due to lack of proper wetting conditions in the model and that simulation was performed in $2D$. Comparison of experimental and simulation results are presented in Fig. 2.6.

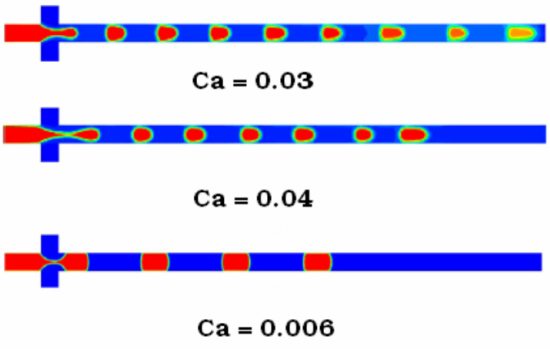

Figure 2.5: Influence of Ca on flow patterns.

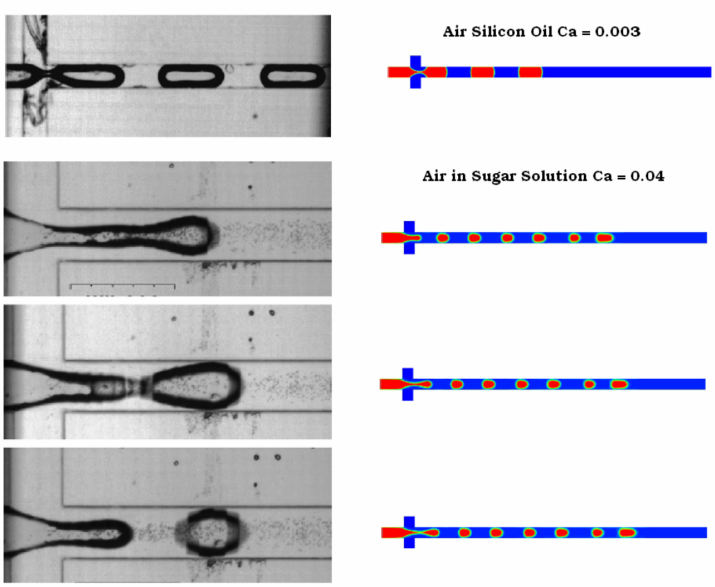

Figure 2.6: Comparison between simulation and experiment [18].

T-Junction Geometry

T-junction geometry is one of the most used geometries. In general, gas stream penetrates main channel from a perpendicular direction and bubble starts to grow. A distortion of bubble in the downstream direction is created by the pressure gradient and the flow in the main channel. As the bubble interface in the upstream side is approaching the edge, the neck connecting the bubble and the gas stream is reduced and finally broken. The gas plug continues downstream, while the gas stream starts the process all over again. Using this geometry, Garstecki *et al.* [22] demonstrated that at a low capillary number, the break-up process, usually referred to as *squeezing* is a balance of the hydrostatic pressure between both fluids. In addition, a scaling law was presented and verified, which relates the dimensions of channels, and mass flow rate ratio with the final length and diameter of the bubble. Qian and Lawal [23] presented a numerical study of Taylor flow in T-junction microchannels using FLUENT, a commercial package based on Volume of Fluid (VOF). Taylor flow is a special type of slug flow where bullet-shape bubbles are separated by liquid slugs. Simulations were performed using a continuum surface force (CSF) model [24], which adds surface tension calculations as a source term in the momentum equation. In addition, FLUENT uses a dynamic boundary condition in the case of wall adhesion. This boundary condition allows for adjustment of curvature of surface near the wall, and this new curvature is used to change the body force term in the surface tension calculation. In this study an analysis was performed comparing inlet condition and tee orientations.

Inlet conditions were modified by changing the inlet gas-liquid velocity ratio. As seen in Fig. 2.7, as velocity ratio is decreased, the flow pattern becomes bubblier and the void fraction increases. The relationship between velocity ratio and the flow regime generated was also seen in the Cubaud study [17], indicating that this type of relationship is independent of mixing geometry. What changes from one geometry to the next, is the transition or critical values from one regime to the other. It is also noted, that while maintaining mass flow rate constant, changing the dimension on the tee has a great effect on the size of the slugs. As shown in Fig. 2.8, the bubble size is directly proportional to the dimensions of the channel.

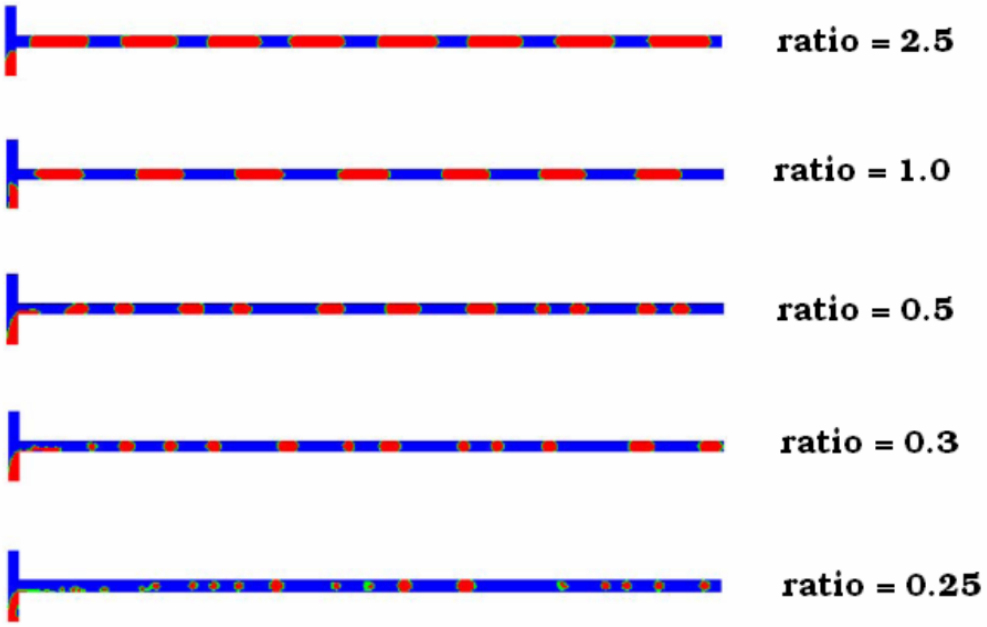

Figure 2.7: Gas-liquid velocity ratio comparison [23].

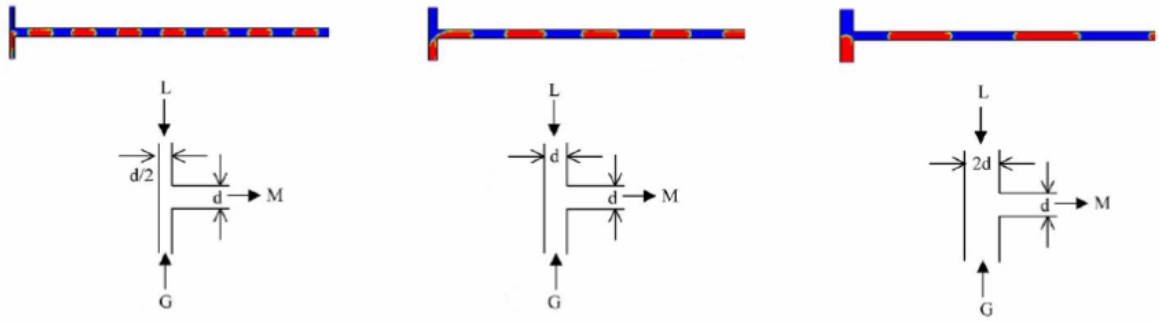

Figure 2.8: Inlet tee size comparison [23].

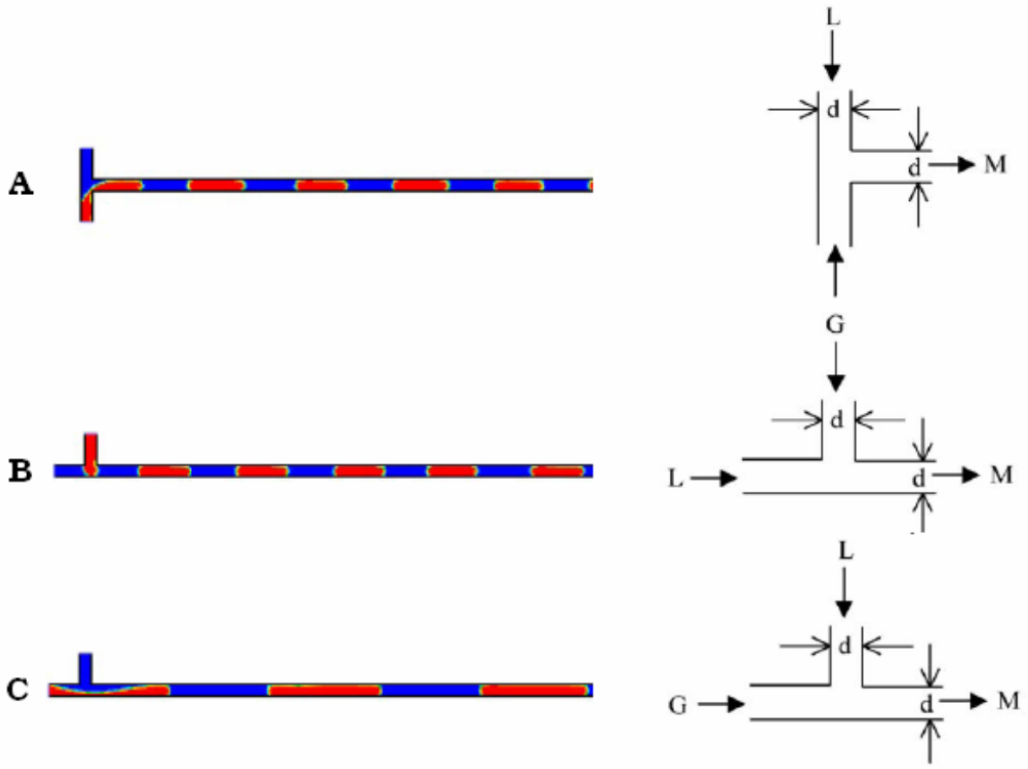

Figure 2.9: Tee orientations comparison [23].

This study compared three different tee orientations as shown in Fig. 2.9. It is noted that there is very little difference between (a) and (b), however, (c) creates longer slugs. It is recommended that the latter orientation should be avoided since it creates a smoother steam at mixing section, therefore creating a more difficult detachment process.

Co-Flowing Geometry

Co-flowing geometry is used to represent a liquid nozzle with an air injection system. In this geometry the bubble size and frequency is mainly determined by the exit velocity of gas stream. As investigated by Sevilla *et al.* [25], gas flow could transition from bubbling regime to jetting regime, if a critical value of gas-liquid velocity ratio is reached. Shao *et al.* [26] introduced a numerical study on the effect of inlet conditions

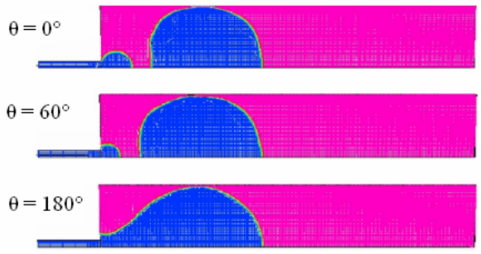

Figure 2.10: Contact angle comparison [26].

on the Taylor flow formation. Simulations were performed using ANSYS, a VOF commercial package. This study is focused on the effect of different inlet conditions. It was noted, that volume of the bubble is directly proportional to gas superficial velocity and bubble velocity is also directly proportional to surface tension. In addition, wetting condition of wall was investigated. Three different cases of contact angle were explored: $\theta_{eq} = 0^o$, $\theta_{eq} = 60^o$, and $\theta_{eq} = 180^o$. As seen in Fig. 2.10, larger contact angles favor the formation of larger bubbles. This study takes advantage of symmetry, only top part of simulation is presented. However, it does not explore the frequency of bubble formation, due to computational cost limitations.

2.2.2 Segregated Flow Area

Dynamics of bubble along the microchannel, referred to as segregated area, is greatly dependent on the interaction between gas, liquid, and solid wall. At this point, the effect of wettability and contact angle would ultimately determine the behavior of the bubble. Cubaud *et al.* [27] provide a comprehensive overview of the morphological changes of static and moving bubbles for different contact angles with hydrophillic and hydrophobic surfaces in square microchannels. For hydrophillic surfaces, bubble flow could be classified in five regimes (bubbly, wedging, slug, annular, and dry) as seen in Fig. 2.11. For hydrophobic surfaces, bubbles are not lubricated and depend on contact line friction. The flow could be divided in three regimes (isolated asymmetric bubble, wavy bubble, and scatter droplet flow) as shown in Fig. 2.12. A similar study was presented by Lee *et al.* [28] focusing in the influence of surface wettability on flow

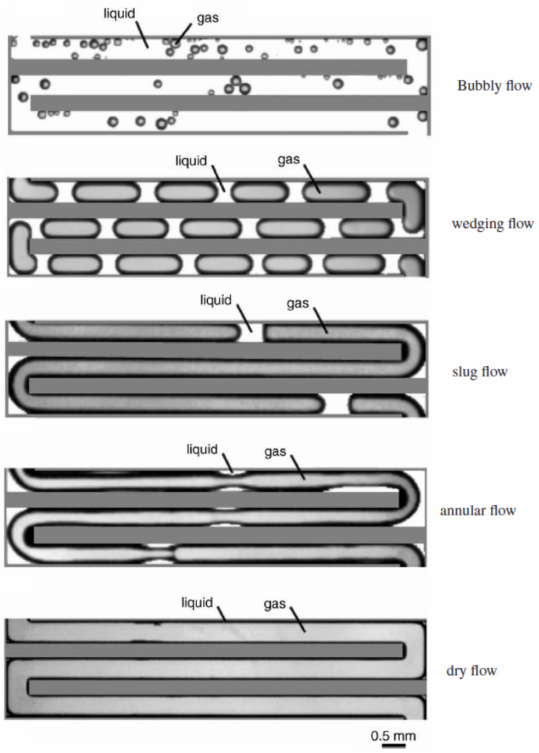

Figure 2.11: Hydrophillic flow regimes [27].

patterns in round mini-channels.

Various numerical studies have been performed for multiphase flows in microchannels. Most of these studies are based on the VOF approach, since it is a conservative method suitable to treat interface topological changes and calculate dynamic contact angle. Taha and Cui [29] model the velocity fields as function of Ca using FLUENT as shown in Fig. 2.13. Tseng *et al.* [30] investigated the influence of surface wettability on the filling process of liquid slugs. It was shown that hydrophobicity is the dominating factor in this process. Fang *et al.* [31] provide a numerical VOF study on contact angle hysteresis for microscale two-phase flows. It was shown that the asymmetric distribution of contact angle might be one of the most important factors in slug behavior on microchannels.

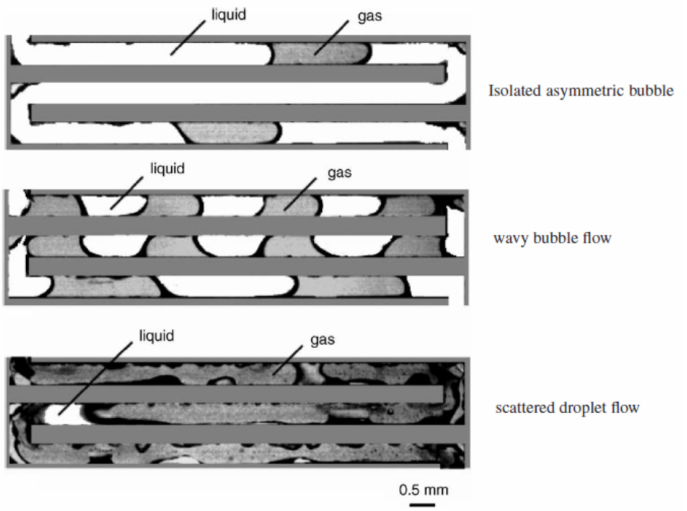

Figure 2.12: Hydrophobic flow regimes [27].

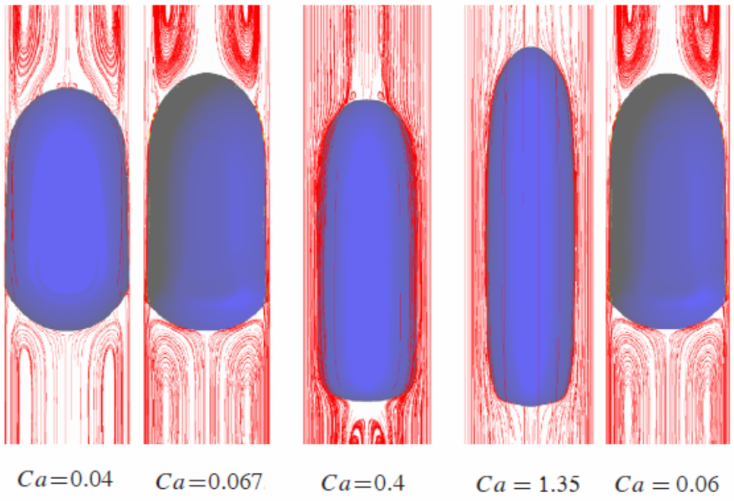

Figure 2.13: Slug rising at different Ca [29].

Chapter 3

Motivation and Objectives

As it was described before, understanding the behavior of multiphase flows in a microchannel could be divided into two main areas: mixing area and segregated flow area. Multiple numerical studies have been performed in each area, however there is not a comprehensive numerical study that takes into account both of the areas. For this reason, it is the motivation for this study, to utilize a Lattice Boltzmann Method to simulate the dynamics of bubble formation and motion along a microchannel. LBM is the numerical tool used in this study because of the great advantages it offers: ability to capture large topological changes at the interface, easy boundary condition implementation, accuracy, easy implementation, and can be fully parallelized.

It is important that each phenomenon (development and transport of the fluids) can be properly simulated in order to capture the complete dynamics of the flow. Therefore, this study is divided into different stages in order to manage the complexity of the problem, which represent the main objectives of this study.

Stage 1: Understanding Dynamics of Bubble Motion

The first stage is to evaluate the capabilities of the model to simulate dynamic behavior of a multiphase systems. This is done by simulating a single bubble rising in an unconfined domain. A comprehensive analysis is presented which includes eight different shape regimes, which are achieved by changing the values of Bo and Mo within the following ranges ($1 \times 10^{-5} < Mo < 3 \times 10^{4}$) and ($1 < Bo < 1 \times 10^{3}$).

In addition, simulations are performed using large density and viscosity ratios, 1000 and 100 respectively. This study will evaluate the topological changes, velocity and pressure profiles, and drag coefficient of the bubble while rising at different regimes, depending on the forces acting on the system. Moreover, the dependence of numerical parameters such as interface thickness, surface tension, viscosity, and density of surrounding on the terminal shape and Re are explored. Simulation results are compared with experimental results for each regime.

Stage 2: Understanding Effect of Confined Domains

The second stage is to introduce the effect of the walls by evaluating the dynamics of a bubble rising in a vertical and inclined square channel with large density and viscosity ratios. This study will investigate the effect of initial conditions, fluid properties, and inclination on the shape, velocity, vorticity, and pressure of the bubble as it rises. This is the beginning stage of evaluating the flow in the segregated area, which currently uses gravity as the driving force in the system.

Stage 3: Formation Process at Mixing Area

The third stage is to investigate the formation process using a T-junction mixing area. This stage is divided into two different parts, one investigates liquid-liquid systems and the other gas-liquid systems. In general, both parts investigate the effect of capillary number, viscosity ratio, flow ratio, and contact angle on the formation process of droplets and bubbles in a microchannel with a T-junction mixing geometry. This stage has two geometrical components: the mixing and the segregated area. The geometry used in the segregated area is similar to the one used in the second stage of this study. However, at this stage gravity is not used as the driving force in the system. Instead, a constant flow rate at each of the entrances becomes the driving mechanism in this system.

The contents of this study are organized as follows:

- Chapter 4 provides background material for Lattice Boltzmann Method, Cahn-Hilliard model, and wetting phenomena.

- Chapter 5 presents the study of a single bubble rising in an unconfined domain.
- Chapter 6 presents the study of a single bubble rising in a vertical and inclined square channel.
- Chapter 7 presents the study of droplet and bubble formation in a microchannel with T-junction.

Chapter 4

Lattice Boltzmann Method

The Lattice Boltzmann Method (LBM) model has been proven to be a very useful numerical method to simulate multiphase systems. The initial model was provided by Gunstensen *et al.* [32] introducing a LBM based on lattice gas model. Multiple variations have been introduced since then. Swift *et al.* [33] introduced a LBM using free-energy approach. In their model the equilibrium distribution function was modified to provide consistency between the pressure tensor and the pressure derived from free-energy. He et al.[34] proposed a new model that reduces the compressibility effect on the LBM. This is accomplished by explicitly eliminating terms of order of magnitude $O(Ma^2)$. Where Ma is the Mach number defined as the ratio between the speed of the object over the speed of sound. This approximation is in accordance with second order expansion in the Chapman-Enskog analysis. Shan *et al.* [19] incorporated the concept of microscopic mean-field interactions between particles into LBM. He *et al.* [36] combined LBM with an idea of level-set for multiphase by using an index function to track interface at different phases in order to simulate multiphase flow at nearly incompressible limit. Inamuro *et al.* [37, 38] introduced a modified LBM to deal with large density ratios. The modification uses Projection Method to calculate the velocity that satisfies continuity at every step. This is to minimize the effect of large density ratios that create spurious velocities. Later, Lee *et al.* [39] provided a detailed study on parasitic currents. The study suggests the possible elimination of parasitic currents can be accomplished if the potential form of the intermolecular

forced is used with a compact isotropic discretization. The latter, is the model used for this study. Mathematical details of this model will be presented in the following section.

LBM simulates fluids based on microscopic or mesoscopic kinetic models, which allows incorporation of underlying physics. The kinetic nature of LBM introduces important features [40, 41]:

- Convection operator is the particle velocity, which is linear. This indicates that a simple scheme could be used to solve an advection equation combined with a collision operator. This allows the recovery of a non-linear macroscopic equations using multi-scale expansion up to second order of accuracy in space and time.
- LBM in the nearly incompressible limit, could recover the incompressible Navier-Stokes Equation (NSE). In addition, pressure can be calculated using an equation of state, rather than solving the Poisson equation.
- LBM uses a minimal set of discrete velocities, reducing significantly the computational cost.

In a general form Lattice Boltzmann Equation (LBE) with Bhatnagar-Gross-Krook (BGK) collision operator is given by [42]

$$\frac{\partial f_\alpha}{\partial t} + \mathbf{e}_\alpha \cdot \nabla f_\alpha = -\frac{1}{\lambda_r}(f_\alpha^{eq} - f_\alpha) \tag{4.1}$$

where f_α is the particle distribution function along α direction, $\mathbf{e}_\alpha$ is the microscopic particle velocity, and λ_r is the relaxation time. The equilibrium distribution function f_α^{eq} is given by

$$f_\alpha^{eq} = t_\alpha \rho \left[1 + \frac{\mathbf{e}_\alpha \cdot \mathbf{u}}{c_s^2} + \frac{(\mathbf{e}_\alpha \cdot \mathbf{u})^2}{2c_s^4} - \frac{(\mathbf{u} \cdot \mathbf{u})}{2c_s^2}\right] \tag{4.2}$$

t_α being the weighting factor, ρ is the density, $\mathbf{u}$ is the macroscopic velocity, c_s is a constant.

The number of microscopic particle velocities is given by the type of lattice model used. Lattice models are usually described as D_nQ_m, where n is the dimension and

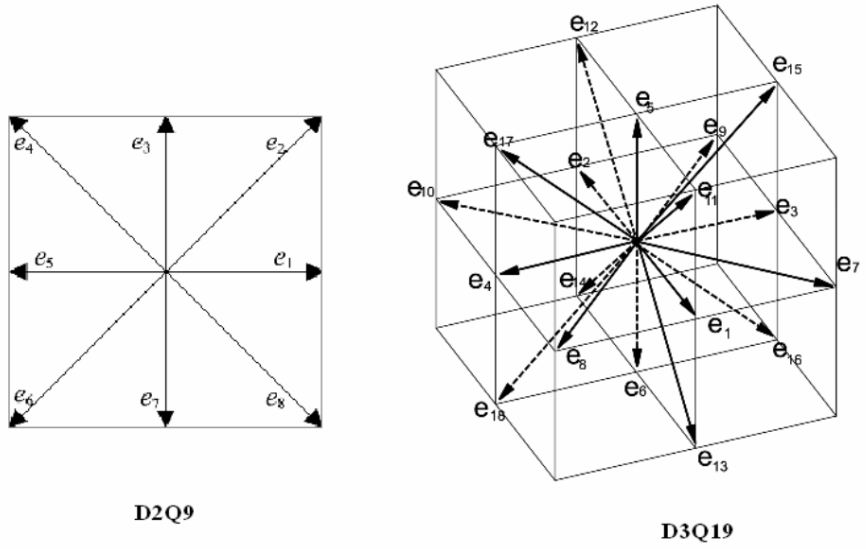

Figure 4.1: Lattice models.

m is number of α directions. Most common models used are $D2Q9$ and $D3Q19$, as could be seen in Fig. 4.1

Particles in LBM go through two different steps: streaming and collision. Particles live on the nodes of a discrete lattice. The particles jump from one lattice node to the next, according to their microscopic particle velocity, this is the streaming step. Then, the particles collide and get a new velocity, this is the collision step.

Macroscopic density ρ and velocity vector $\mathbf{u}$ are related to particle distribution by

$$\begin{aligned} \rho &= \sum_{\alpha} f_{\alpha} \\ \rho \mathbf{u} &= \sum_{\alpha} \mathbf{e}_{\alpha} f_{\alpha} \end{aligned} \tag{4.3}$$

This study uses a discrete Boltzmann Equation (DBE) with external force in the potential form described by Lee and Fisher [39] which can be written as

$$\frac{\partial f_{\alpha}}{\partial t} + \mathbf{e}_{\alpha} \cdot \nabla f_{\alpha} = -\frac{1}{\lambda_r} \left(f_{\alpha} - f_{\alpha}^{eq} \right) + \frac{1}{\rho c_s^2} \left(\mathbf{e}_{\alpha} - \mathbf{u} \right) \cdot (\mathbf{F} + \mathbf{G}) f_{\alpha}^{eq} \tag{4.4}$$

where equilibrium distribution function f_{α}^{eq} is given by Eq. (4.2) and $\mathbf{F}$ represents

the averaged external force exerted on each particle. $\mathbf{F}$ is obtained by taking into account the free energy of a system [35]. In a system of immiscible incompressible fluids, external force represents the intermolecular attraction by using the mean-field approximation, the exclusion-volume of molecules [36], and the hydrodynamic pressure gradient, yielding

$$\mathbf{F} = \nabla \rho c_s^2 - \nabla p_1 - C \nabla \mu \tag{4.5}$$

where p_1 is the hydrodynamic pressure used to enforce incompressibility and μ is the chemical potential. $\mathbf{G}$ represents the gravitational force which takes the form $\mathbf{G} = -\rho g \nabla h$, where g is the gravitational acceleration and h is the elevation from a reference point so that $\partial_y h = 1$, but $\partial_x h = 0$.

Eq. (4.4) recovers the *mass* and *momentum* equations. However, a transformation of the DBE is necessary to eliminate acoustic waves at the low frequency limit and to improve stability. He *et al.* [36] first used the transformation to obtain the pressure evolution equation. This study uses the following new particle distribution function [35, 43]

$$g_\alpha = f_\alpha c_s^2 + (p_1 + \rho_l g h - \rho c_s^2) \Gamma_\alpha(0) \tag{4.6}$$

in which $\Gamma_\alpha(\mathbf{u}) = f_\alpha^{eq}/\rho$ and ρ_l is the density of liquid. Taking the total derivative $D_t = \partial_t + \mathbf{e}_\alpha \cdot \nabla$ of the new variable g_α gives

$$\begin{aligned} &\frac{\partial g_\alpha}{\partial t} + \mathbf{e}_\alpha \cdot \nabla g_\alpha = -\frac{1}{\lambda_r} \left(g_\alpha - g_\alpha^{eq} \right) \\ &+ (\mathbf{e}_\alpha - \mathbf{u}) \cdot \left[\nabla \rho c_s^2 \left(\Gamma_\alpha - \Gamma_\alpha(0) \right) - \left(C \nabla \mu + \rho g \nabla h \right) \Gamma_\alpha \right] \\ &+ \mathbf{e}_\alpha \cdot \left(\rho_l g \nabla h \right) \Gamma_\alpha(0), \end{aligned} \tag{4.7}$$

where the new equilibrium g_α^{eq} is

$$g_\alpha^{eq} = t_\alpha \left[P + \rho c_s^2 \left(\frac{\mathbf{e}_\alpha \cdot \mathbf{u}}{c_s^2} + \frac{(\mathbf{e}_\alpha \cdot \mathbf{u})^2}{2 c_s^4} - \frac{(\mathbf{u} \cdot \mathbf{u})}{2 c_s^2} \right) \right], \tag{4.8}$$

in which $P = p_1 + \rho_l gh$. Using dimensional analysis, it could be shown that in the case of low Ma the ratio of the dynamic and static pressures to the thermodynamic pressure p_0 is $P/p_0 \sim O(Ma^2)$, indicating that all thermodynamic quantities can be assumed to be independent of the dynamic pressure [44]. In the derivation of Eq. (4.7), the terms with $\mathbf{u}\cdot\nabla P$ are omitted since they are $O(Ma^3)$. LBE is obtained by discretizing Eq. (4.7) along characteristics over the time step δt:

$$\begin{aligned}\bar{g}_\alpha(\mathbf{x}+\mathbf{e}_\alpha\delta t, t+\delta t) - \bar{g}_\alpha(\mathbf{x},t) = &-\frac{1}{\tau+0.5}(\bar{g}_\alpha - \bar{g}_\alpha^{eq})|_{(\mathbf{x},t)} \\ &+\delta t(\mathbf{e}_\alpha - \mathbf{u})\cdot[\nabla\rho c_s^2(\Gamma_\alpha - \Gamma_\alpha(0)) - (C\nabla\mu + \rho g\nabla h)\,\Gamma_\alpha]_{(\mathbf{x},t)} \\ &+\delta t\mathbf{e}_\alpha\cdot(\rho_l g\nabla h)\,\Gamma(0)_\alpha|_{(\mathbf{x},t)}.\end{aligned} \tag{4.9}$$

In Eq. (4.9), the modified particle distribution function $\bar{g}_\alpha$ and equilibrium distribution function $\bar{g}_\alpha^{eq}$ are introduced (see Appendix).

The macroscopic equations recovered from Eq. (4.7) using the Chapman-Enskog expansion are the *momentum* and *pressure* equations described as follows:

$$\rho\left(\frac{\partial\mathbf{u}}{\partial t} + \mathbf{u}\cdot\nabla\mathbf{u}\right) = -\nabla P - C\nabla\mu + \nabla\cdot\eta\left[\nabla\mathbf{u} + (\nabla\mathbf{u})^T\right] + (\rho-\rho_l)\mathbf{g}, \tag{4.10}$$

$$\frac{\partial P}{\partial t} + \rho c_s^2\nabla\cdot\mathbf{u} = 0, \tag{4.11}$$

where η is the mixture viscosity that is related to the dimensionless relaxation time (τ) by $\eta = c_s^2\rho\tau\delta t$.

From the Cahn-Hilliard model [45] it is known that the behavior of a multi-component system out of equilibrium is governed by the evolution equation of the composition C.

$$\frac{\partial C}{\partial t} + \mathbf{u}\cdot\nabla C = \nabla\cdot(M\nabla\mu)\,. \tag{4.12}$$

where $M > 0$ is the mobility. C and ρ have a linear relationship given by

$$\rho = \rho_l C + \rho_g(1-C) \tag{4.13}$$

where ρ_g indicates density of gas.

A new density function is necessary to recover the evolution equation of the composition C. The new density function could be simply obtained by $h_\alpha = \frac{C}{\rho} f_\alpha$ and $h_\alpha^{eq} = \frac{C}{\rho} f_\alpha^{eq}$. Taking total derivative D_t of the new density function h_α and taking into account Eq. (4.12) produces

$$\begin{aligned} \tfrac{\partial h_\alpha}{\partial t} + \mathbf{e}_\alpha \cdot \nabla h_\alpha = -\tfrac{1}{\lambda_r} \left(h_\alpha - h_\alpha^{eq}\right) \\ + \left(\mathbf{e}_\alpha - \mathbf{u}\right) \cdot \left[\nabla C - \tfrac{C}{\rho c_s^2} \left(\nabla p_1 + C \nabla \mu\right)\right] \Gamma_\alpha + \nabla \cdot \left(M \nabla \mu\right) \Gamma_\alpha, \end{aligned} \tag{4.14}$$

where

$$h_\alpha^{eq} = t_\alpha C \left[1 + \frac{\mathbf{e}_\alpha \cdot \mathbf{u}}{c_s^2} + \frac{\left(\mathbf{e}_\alpha \cdot \mathbf{u}\right)^2}{2c_s^4} - \frac{\left(\mathbf{u} \cdot \mathbf{u}\right)}{2c_s^2}\right]. \tag{4.15}$$

The modified particle distribution function $\bar{h}_\alpha$ and LBE for $\bar{h}_\alpha$ can be derived similarly to equations presented in the appendix. Calculating the zeroth and first moment of the modified particle distribution function, yields the composition, momentum and a combination of static and dynamic pressure.

$$\begin{aligned} C &= \textstyle\sum_\alpha \bar{h}_\alpha + \frac{\delta t}{2} \nabla \cdot \left(M \nabla \mu\right), \\ \rho c_s^2 \mathbf{u} &= \textstyle\sum_\alpha \mathbf{e}_\alpha \bar{g}_\alpha - \frac{\delta t}{2} C \nabla \mu, \\ P &= \textstyle\sum_\alpha \bar{g}_\alpha + \frac{\delta t}{2} \mathbf{u} \cdot \nabla \rho c_s^2. \end{aligned} \tag{4.16}$$

In order to obtain composition C using Eq. (4.16) an implicit calculation is required since chemical potential μ is a function of C, as it is described in the following section. Our model takes this value from the previous time step explicitly [46]. For the discretization of forcing terms, see [39].

The LBM used in this study includes two different parts: diffuse interface model and wetting boundary condition. The following sections will provide an introduction to each of these parts.

4.1 Diffuse Interface - Cahn-Hilliard Model

The interface between two species is produced by the system's need to minimize energy. At molecular level the energy of interaction of two molecules of different species is larger than the energy for two of same species. Therefore, if molecules of different species are separated the energy will be reduced. If molecules of one species are added to the other, energy is increased and system tends to separate them, making composition, C, a key thermodynamic variable in the behavior of the mixture. Cahn and Hilliard [45] postulated that the mixing energy density for the isothermal system takes the following form:

$$E_{mix}\left(C, \nabla C\right) = E_0\left(C\right) + \frac{\kappa}{2}|\nabla C|^2 \tag{4.17}$$

where κ is the gradient parameter. Assuming that the bulk energy E_0 is given by a double-well potential function

$$E_0\left(C\right) \approx \beta C^2\left(C-1\right)^2, \tag{4.18}$$

where β is a constant. The classical part of chemical potential is the rate of change of E_0 with respect to C

$$\mu_0 = \frac{\partial E_0}{\partial C}. \tag{4.19}$$

The equilibrium profile is determined such that the energy is minimized and reads $\mu = \mu_0 - \kappa\nabla^2 C = const$ in 1D. In a plane interface at equilibrium, the interface profile is

$$C\left(z\right) = \frac{1}{2} + \frac{1}{2}\tanh\left(\frac{2z}{D}\right), \tag{4.20}$$

where D is the numerical interface thickness, which is chosen based on accuracy and stability. Given D and β, one can compute the gradient parameter κ and the surface tension force σ:

$$\kappa = \frac{\beta D^2}{8}, \quad \sigma = \frac{\sqrt{2\kappa\beta}}{6}. \tag{4.21}$$

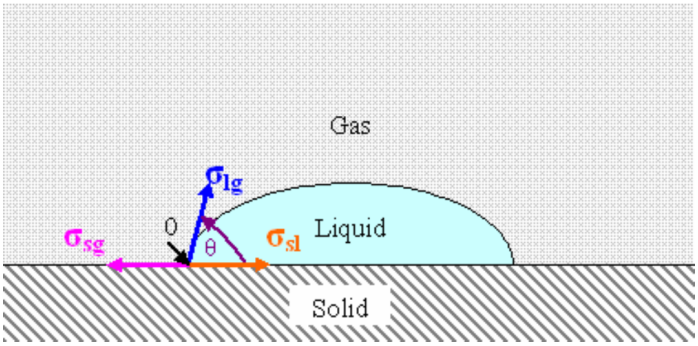

Figure 4.2: Interfacial tension acting on contact line.

In the convective Cahn-Hilliard equation, the diffusive flow rate $\mathbf{j}$ is assumed to be proportional to a thermodynamic driving force, which is proportional the gradient of the chemical potential [47]

$$\mathbf{j} = -M\nabla\mu, \tag{4.22}$$

where M is the mobility. Mixing energy is minimized through bulk diffusion and the behavior of the system out of equilibrium is dictated by the evolution equation for the composition C as given in Eq. (4.12).

4.2 Wetting Phenomena and Contact Angles

Wettability of a liquid is described as the affinity of liquids for solids. Wettability is quantified with a contact angle θ_{eq}, defined as the angle between liquid-gas interface and solid surface measured from point 0 as shown in Fig. 4.2. In this figure there are three interfaces: liquid-gas, solid-liquid and solid-gas. Each of these interfaces has an interfacial tension associated to them, σ_{lg}, σ_{sl} and σ_{sg} respectively. At equilibrium, the force balance at point 0 in the horizontal direction indicates that $\sigma_{lg}\cos\theta_{eq} = \sigma_{sg} - \sigma_{sl}$. This is referred to as the Young's Equation.

Given the contact angle, the degree of wettability of a fluid can be determined. If $\theta_{eq} = 0^o$, it is said that liquid completely wets the surface. If $0^o < \theta_{eq} < 90^o$ liquid is classified as wetting. For $90^o < \theta_{eq} < 180^o$ liquid is referred to as non-wetting and $\theta_{eq} = 180^o$ liquid is completely non-wetting. As liquid starts moving along the surface,

there might be a change on the contact angle depending of the wetting properties of the fluid. In addition, due to surface inhomogeneity, roughness and impurities, usually there is a difference between the advancing and receding angles, usually referred to as contact angle hysteresis.

Evaluation of interfacial tensions can be accomplished by introducing the total free energy, which is a combination of bulk free energy Ψ_b and surface free energy Ψ_s

$$\Psi_b + \Psi_s = \int_V (E_0(C) + \frac{\kappa}{2}|\nabla C|^2)dV + \int_S (\phi_0 - \phi_1 C_s + \phi_2 C_s^2 - \phi_3 C_s^2 + \cdots)dS \quad (4.23)$$

where ϕ_i with $i = 0, 1, 2$ are constant coefficients. Using the same principle used in the diffuse interface method, chemical potential of the bulk and the surface can be obtained by taking the derivative of the total free energy with respect to C. Using the chemical potential, the value of the three interfacial tensions σ_{lg}, σ_{sl} and σ_{sg} can be obtained.

The solution of Eq. (4.12) requires two boundary conditions. The boundary condition for $\nabla^2\mu$ ensures no mass flux due to the chemical potential gradient in the direction normal to the solid boundary,

$$\mathbf{n} \cdot \nabla\mu|_s = 0, \quad (4.24)$$

where $\mathbf{n}$ is the unit normal vector. The boundary condition for $\nabla^2 C$ can be established by minimizing the total free energy subject to the specified wall free energy. This study uses a cubic boundary condition is given as

$$\mathbf{n} \cdot \nabla C|_s = \frac{\phi_c}{\kappa}\left(C_s - C_s^2\right). \quad (4.25)$$

where C_s is the composition at a solid surface that generally differs from the bulk or equilibrium composition and ϕ_c is a constant related to the equilibrium contact angle θ_{eq} by $\phi_c = -\cos\theta_{eq}\sqrt{2\kappa\beta}$. Detailed derivation of these boundary conditions can be found in the study presented by Lee and Liu [48].

Chapter 5

Single Bubble Rising in Unconfined Domain

The first stage of this study is to understand the dynamic behavior of multiphase systems, which is done by simulating the dynamics of a bubble rising in an unconfined domain under the influence of buoyancy force.

5.1 Background

A bubble rising under the influence of gravitational force is one of the most common gas-liquid flow phenomena. Understanding the dynamic interaction between the phases is an important key for the design and operation of industrial applications such as gas-liquid column reactors [49, 50, 51]. Dynamic behavior of a rising bubble has been a subject of both experimental and numerical studies for many years. Experimental studies and correlations were reviewed by Clift *et al.* [52]. Later, a more comprehensive study was presented by Bhaga and Weber [53], introducing experimental data and correlations for bubble rise velocity and shape regimes. Rising of a bubble in a viscous fluid under the influence of gravitational forces can be generally grouped in three different regimes: Spherical, Ellipsoidal, and Spherical Cap as described in [52]. (Description of each regime will follow). These regimes are achieved, depending on the values of two non-dimensional quantities, as defined below:

Bond number:

$$Bo = \frac{g\triangle\rho d_0^2}{\sigma}, \tag{5.1}$$

Morton number:

$$Mo = \frac{g\triangle\rho\eta_l^4}{\sigma^3\rho_l^2}, \tag{5.2}$$

where d_0 is the initial bubble diameter, ρ_l is liquid density, η_l is liquid viscosity, $\triangle\rho = \rho_l - \rho_g$ is density difference between continuous medium and the dispersed fluid and σ is the surface tension. Bo is the ratio of the body forces (effective gravitational forces) and the surface tension, but it could also be considered as a dimensionless size of the bubble [54]. Mo provides a description of the properties of the surrounding fluid, mainly focusing on viscosity and surface tension. Using these non-dimensional parameters, the dynamics of a single bubble could be predicted. Clift *et al.* [52] introduced a bubble diagram to predict the terminal velocity and shape of a rising bubble at low density ratios, as can be seen in Fig. 5.1. This diagram uses Bo, Mo and Reynolds number, which is defined as follows:

Reynolds number:

$$Re = \frac{\rho_l U_t d_0}{\eta_l}, \tag{5.3}$$

where U_t is the terminal velocity of the bubble. Terminal velocity is defined as the steady velocity that the bubble reaches when there is a balance between buoyancy and drag forces. A general classification of the bubble is usually done depending on final shape or by the primary forces acting on the system. However, the transition areas from regime to regime are still not well defined. A brief description of each of the three main regimes: Spherical, Ellipsoidal, and Spherical Cap is provided as follows [52]:

- **Spherical Regime:** This regime is dominated by surface tension and viscous forces. Original size of the bubble is small, usually less than 1.3 *mm*. The shape of the bubble remains spherical or nearly-spherical. Usually the ratio of minor to major axis is less than 10%. In this regime, the terminal velocity is proportional to the size of the bubble. For pure systems, meaning systems which do not have contaminants at the interface, the evolution of terminal rising

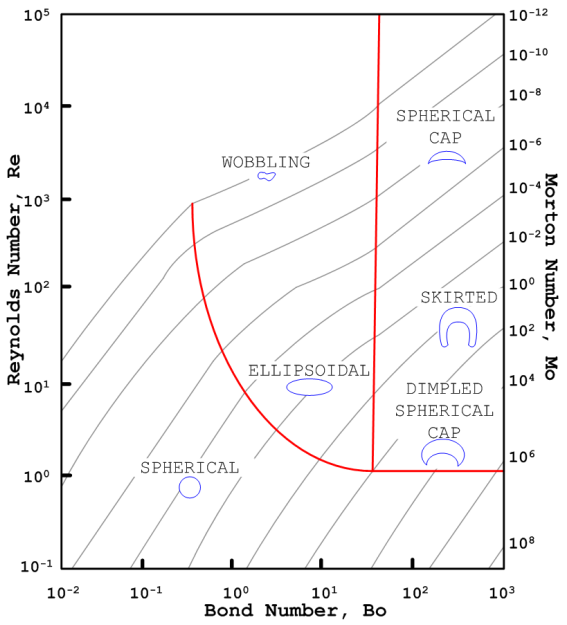

Figure 5.1: Shape regime map [52].

velocity can be described by Hadamard [55] and Rybczynski [56] as follows:

$$U_t = \frac{g d_0^2 \Delta\rho}{6\eta_l} \frac{(1 + (1/\lambda_1))}{(2 + 3(1/\lambda_1))}, \tag{5.4}$$

where $\lambda_1 = \eta_l/\eta_g$ is viscosity ratio.

- **Ellipsoidal Regime:** This regime is mainly dominated by surface tension. Bubble size is intermediate, typically from 1.3 to 6 mm, and the range for Bo is $0.25 < Bo < 40$. Final shape is usually oblate with convex interface if looking from inside. Generally, there is no fore-and-aft symmetry. In this regime, there is little viscous resistance to internal circulation, therefore drag and terminal velocity are very sensitive to contamination. Terminal velocity for pure systems is closely approximated by a correlation suggested by Mendelson [57] based on wave theory

$$U_t = \sqrt{\frac{2.14\sigma}{\rho_l d_0} + 0.505 g d_0}. \tag{5.5}$$

- **Spherical Cap Regime:** This regime is governed by inertia force. Bubble size is large, usually bigger than 6 *mm*. $Bo > 40$ and $Re > 1.2$. In this regime, terminal velocity of bubble is proportional to size. In addition, large inertia creates higher deformation by creating high pressure on the front and rear while low at the sides. Rising velocity can be described by a theory proposed by Davies and Taylor [58]

$$U_t = \frac{2}{3}\sqrt{\frac{gd_0}{2}\frac{\Delta\rho}{\rho_l}}. \tag{5.6}$$

Computational studies for multiphase flows have been performed using various numerical methods; see [41]. Specifically for bubble rising, numerical methods used include but are not limited to following computational studies. Chen *et al.* [59] evaluated dynamics of transformation from spherical to toroidal bubble using a VOF method. Tomiyama *et al.* [60] studied dynamic behavior in the regime of surface tension dominance. However, more recent studies have expanded evaluation to different shape regimes. Van Sint Annaland *et al.* [61] presented a 3D VOF algorithm using a new interface reconstructing technique based on piecewise linear interface representation. Later, Van Sint Annaland *et al.* [62] introduced a 3D front tracking model using new surface force to avoid the explicit computation of interface curvature. Bonometti and Magnaudet [63] explored the dynamics of a single rising bubble using a 3D algorithm which utilizes interface-capturing method for two-phase flows with high density and viscosity ratios. Smolianski *et al.* [64] proposed a numerical method to simulate single bubble and bubble swarms in ellipsoidal and spherical flow regimes, which accurately captures the change and the deformation of the interface. Hua *et al.* [65] used a front tracking algorithm to simulate dynamics of a single bubble in a 3D model.

The study of dynamics of a rising bubble using LBM have been explored by Sankaranarayanan *et al.* [66] using a multi-component model as described by [19], [67], and [68] as a benchmark study to gauge the capabilities of LBM to simulate bubbly flows, with a density ratio of 100, $Bo < 5$ and $Mo > 1\times10^{-6}$. Later, the same authors introduced a new implicit formulation in order to increase the range of dimensionless simulation parameters to $Bo < 10$ and $Mo > 1\times10^{-8}$ [20]. Takada *et al.* [69] provided

a comparison study for single and multiple bubbles rising between LBM and VOF. LBM simulation was performed using free energy based on the model by [33], and VOF simulation was done based on a model presented by Hirt and Nichols [70]. This study showed that LBM exhibited higher deformation than VOF, which was attributed to the uniformly applied buoyancy force in the LBM simulation. The free energy model described by [33] was also employed by Frank *et al.* [71], for a single bubble rising at $Re < 1.8$. They reported inadequate agreement with experimental results, largely because the simulations were performed in two-dimensions. A projection method was introduced by Inamuro *et al.* [37], where simulations with density ratios up to 1000 were achieved. Kurtoglu and Lin [54] presented a LBM based on phase-field approach [45] and total variation diminishing (TVD) discretization [43], and the simulation results were presented in the range of $Bo < 100$ and the density ratio of 2.45. Considering that gas-liquid systems in industrial practice typically have values of Mo and Bo in the range ($10^{-12} < Mo < 10^{6}$), and ($10^{-2} < Bo < 10^{4}$), and the density ratio of up to 1000, studies of a single bubble rising using LBM thus far, have been limited to a few shape regimes and low ranges of Bo, Mo, and density ratio used in the simulations.

5.2 Numerical Method Validation

In order to gauge the capabilities of the LBM algorithm, a series of 2D analyses are performed to evaluate the effect of important numerical parameters in the simulation. These parameters included grid resolution, domain size, density ratio, viscosity ratio, interface thickness, and surface tension. Unless otherwise mentioned, the evaluation is performed for fixed values of $Bo = 10$, $Mo = 2 \times 10^{-2}$, and $d_0 = 40$ in lattice unit.

5.2.1 Grid Resolution Dependence

A grid resolution analysis was performed using a grid size as a function of the initial diameter of the bubble $4d_0 \times 7d_0$. The sizes of the grids used in this analysis were 160×280, 320×560, and 640×1120. Note that plots presented in this task use

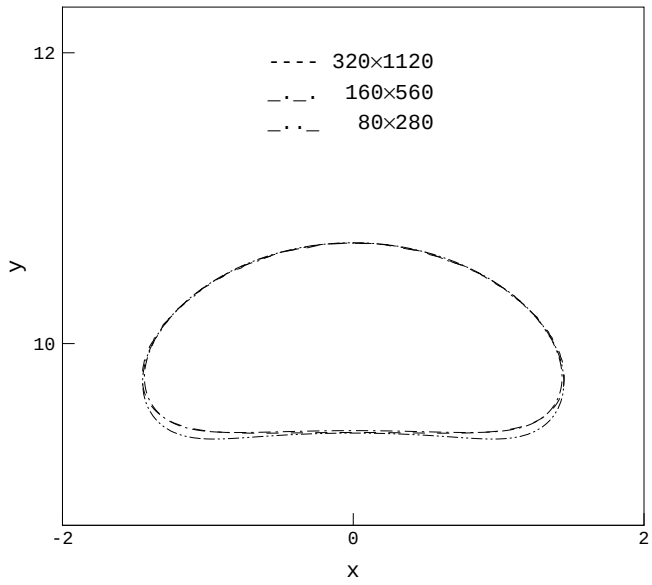

Figure 5.2: Effect of grid resolution on terminal shape at $T = 10$.

non-dimensional time $T = t/t_{n1}$, where $t_{n1} = \sqrt{d_0/g}$.As shown in Fig. 7.3, the effect of the grid resolution on the final shape is not very significant. Comparing grid sizes 320×560, and 640×1120, the final shape for each case is almost overlapping each other. However, the final shape in the coarse grid, 160×280, has a slight difference at the sides of the bubble, but overall the shape is properly maintained. In addition, Fig. 5.3 presents the effect of grid resolution on terminal Re indicating a percent difference no greater than 5% between the results. Considering the results provided by this analysis, it is determined that using the coarse grid in this study, corresponding to $d_0 = 40$ would provide reasonable accuracy and avoid high computational cost.

5.2.2 Domain Size Dependence

Simulations are performed in a confined domain, ergo boundary conditions are no-slip in all directions and bounce-back conditions are applied for both g_α and h_α. Analysis of domain size dependence is performed to determine the influence of the radial and vertical walls on bubble rising. In the radial direction, as domain increases, the

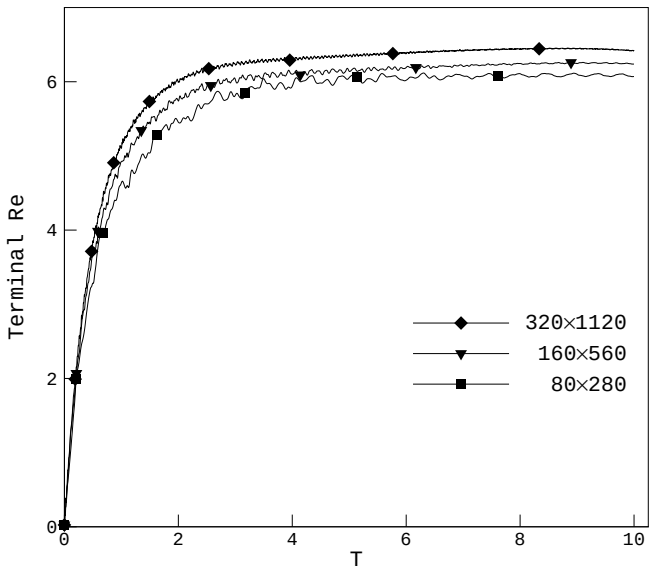

Figure 5.3: Effect of grid resolution on terminal Re.

viscous effect created by wall becomes less significant on the behavior of the bubble. Viscous effects caused by the walls will constrain the radial deformation and slow down the bubble. Therefore, it is critical to determine the minimum radial size of the computational domain that practically eliminates the wall effect on the dynamics of a rising bubble.

In order to determine the minimum radial size for 3D calculations, tests are performed by systematically increasing the radial size by multiples of d_0. A comparison on terminal shape and Re between different tests is presented. As shown in Fig. 5.4, the deformation of the bubble is less affected by wall when radial direction is $4d_0$. In addition the wall effect on terminal velocity is reduced significantly when the domain is $6d_0$, as could be seen in Fig. 5.5. However, the use of this dimension will become computationally costly in 3D calculations. When the domain size is less than $4d_0$, bubble velocity is decreased due to a higher wall viscous effect. In addition, this will reduce the vertical translation of the bubble and minimize the deformation radially. Therefore, to reduce this viscous effect a radial domain size of $4d_0$ is selected, since it has a difference of less than 10% and provides a final shape very close to that in a

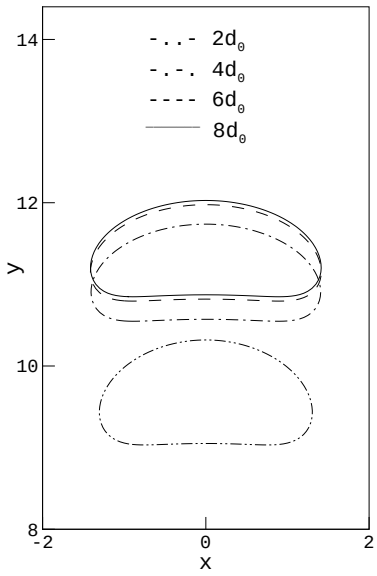

Figure 5.4: Effect of radial domain size on terminal shape at $T = 10$.

larger domain. This domain size provides a compromise between computational cost and simulation accuracy. The influence of the size on the vertical direction is not very significant as long as the bubble does not reach the top wall. The vertical size is different in each case, since the bubble displacement depends on the value of Re. For cases of $Re \sim 1$, vertical size is around $4d_0$. However, for $Re \sim 100$ size could be as high as $9d_0$. Similar validation was performed by [72], resulting in a radial domain of $4d_0$ and vertical of $12d_0$.

5.2.3 Density Ratio Dependence

Effect of density ratio is evaluated by comparing the terminal Re and shape of three different cases. A density ratio is defined as ρ_l/ρ_g and the test cases have density ratios of 10, 100, and 1000, while maintaining all other parameters constant. As shown in Fig. 5.6, the density ratio has a small effect on the final Re of the bubble. The difference between cases of the density ratios of 10 and 1000 is about 10%. The rising Re is influenced by the numerical value of gravity. Using non-dimensional numbers,

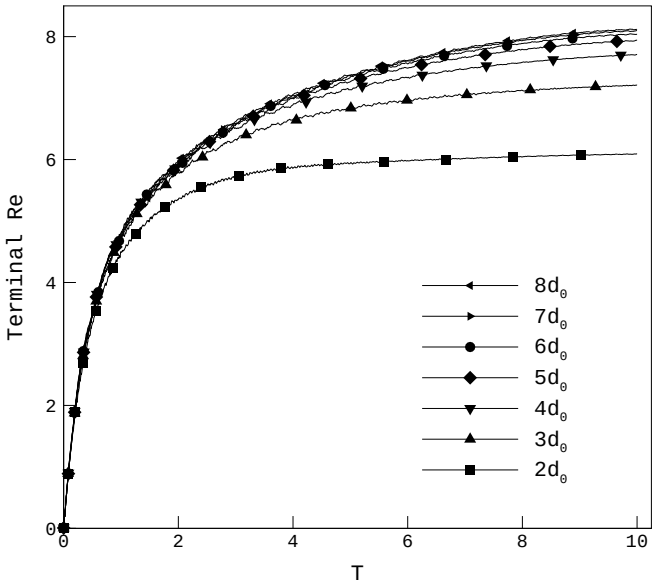

Figure 5.5: Effect of radial domain size on terminal Re.

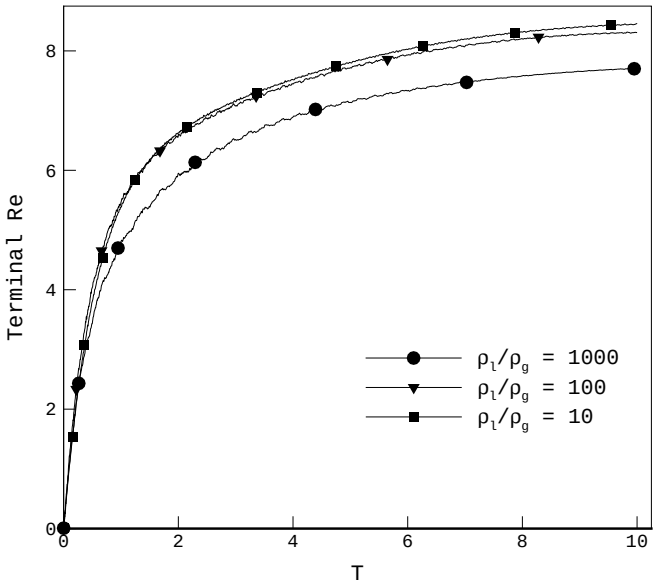

Figure 5.6: Effect of density ratio on terminal Re.

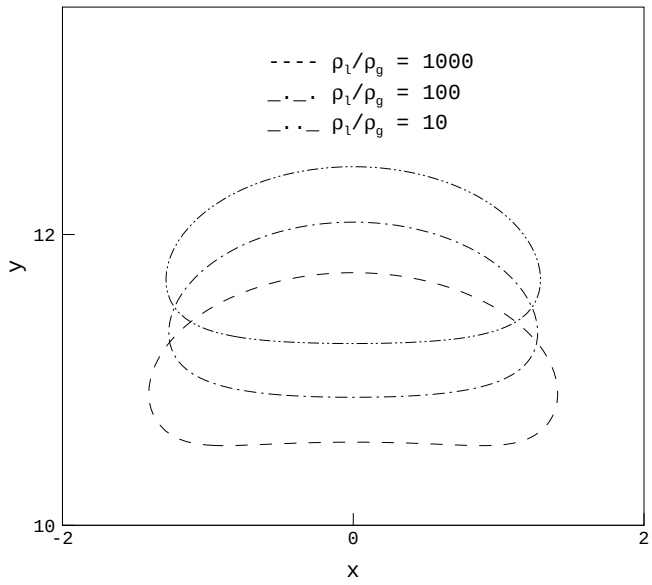

Figure 5.7: Effect of density ratio on terminal shape at $T = 10$.

it can be seen that gravity is inversely proportional to $\triangle\rho$. Assuming $\rho_l = 1$, $\Delta\rho$ for each case is 0.9, 0.99 and 0.999 respectively. Therefore, the difference between the numerical values of gravity in each case is also around 10%. Fig. 5.7 shows the final shape for all the cases at $T = 10$. As can be seen from the figure, a change on a density ratio has a small effect on final shape. Deformation mainly depends on the value of surface tension, which remains unchanged for all the test cases. However, the density ratio has an effect on final position. A higher density ratio provides a lower value of terminal Re, therefore the bubble will reach smaller distances in the same amount of time. A study presented by [72] investigated the effect of density ratio on terminal velocity and shape. Their conclusion indicates that the effect of density ratio is more significant in terminal velocity than on terminal shape. The results of their study agree with the results obtained in current validation.

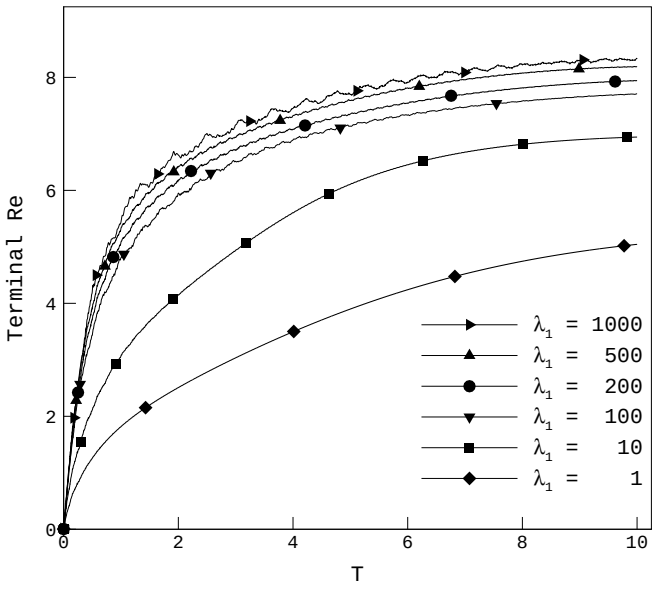

Figure 5.8: Effect of viscosity ratio on terminal Re.

5.2.4 Viscosity Ratio Dependence

In order to evaluate the effect of viscosity ratio, defined as $\lambda_1 = \eta_l/\eta_g$, on the dynamic behavior of a rising bubble, the six cases evaluated are $\lambda_1 = 1$, 10, 100, 200, 500 and 1000. As viscosity ratio decreases, the interface becomes more immobile and shear stress in the system becomes more significant. These factors make the bubble behave more like a rigid object and enhance the effect of the wall on the rising bubble. In addition, reduction of viscosity ratio has increased the internal circulation of the bubble, which delays the wake formation behind the bubble [52]. Therefore, when the viscosity ratio is at the lowest value studied here, 1, the terminal Re is considerably reduced and the bubble exhibits little deformation. The effect of modifying viscosity ratio can be seen in Fig. 5.8 for terminal Re. It is noted that as the value of viscosity ratio is increased, terminal Re tends to collapse into a single curve. Effect of viscosity ratio for terminal shape is presented in Fig. 5.9. These results show that there is very little change on the final shape is viscosity ratio is ≥ 500. However, terminal shapes for viscosity ratios ≥ 100 maintain same characteristics and profile. In general, using

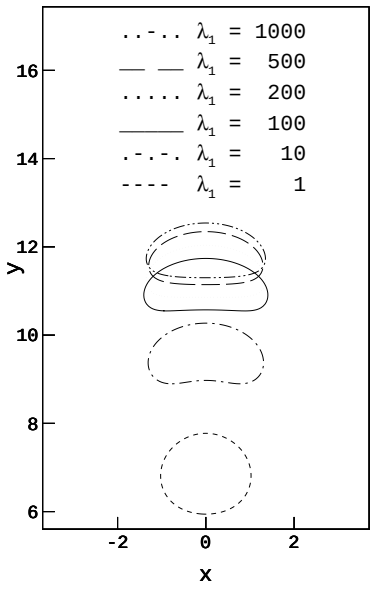

Figure 5.9: Effect of viscosity ratio on terminal shape at $T = 10$.

a high viscosity ratio is needed to achieve a high and accurate value of Re and reach a consistent final shape. The study by [72] also concluded that change on viscosity ratio has a strong effect on the terminal velocity as well as terminal shape, a viscosity ratio of 100 was used in their work.

5.2.5 Interface Thickness Dependence

Interface thickness D is a numerical value used in the diffuse interface method to improve stability and accuracy in the simulation. A dimensionless number that relates D and a characteristic length scale is the Cahn number (Cn), defined as $Cn = D/d_0$. As the value of D increases, a higher level of accuracy and stability in terms of numerical discretization is achieved while the description of phase interface deviates from the sharp interface limit. As can be seen in Figs. 5.10 and 5.11, change of Cn value does not have a significant effect on the terminal Re or shape of the bubble. Note that there is a lower stability limit in the value of $D \sim 3$, which is related to the number of grid points needed to resolve the interface region. The LBM model

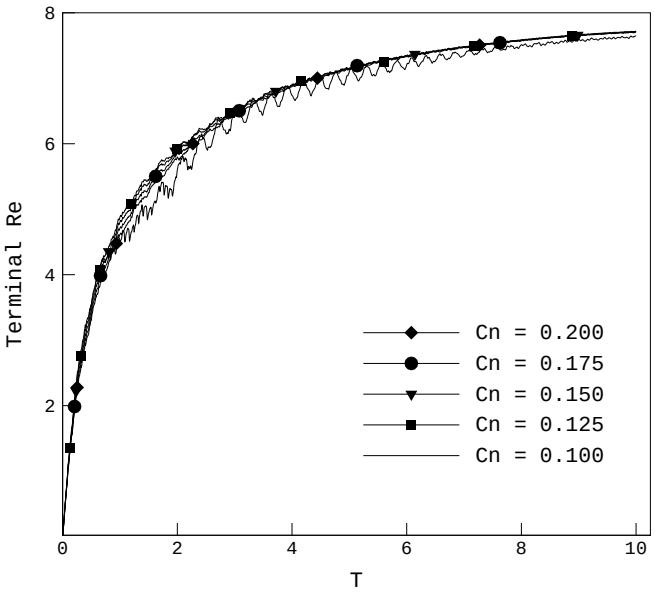

Figure 5.10: Effect of interface thickness on terminal Re at $T = 10$.

used in this study uses an isotropic discretization suggested by Lee and Fischer [39], in order to eliminate the parasitic currents in the system.

In addition to the evaluation of the effect of interface thickness on terminal Re and shape, numerical tests are also performed to ensure satisfaction of Galilean invariance. A lack of Galilean invariance is an undesirable feature of some two-phase flow LBM, and is due to unwanted terms proportional to $\mathbf{u} \cdot \nabla\rho$ in the recovering process of macroscopic governing equations [73]. Galilean invariance can be quantified by a dimensionless error as a function of U_y, a constant and homogeneous vertical velocity, defined as

$$E(U_y) = 1 - \frac{R_v}{R_h} \tag{5.7}$$

where R_v and R_h are the vertical and horizontal radii of a moving bubble measured after $50,000$ iterations respectively. Numerical tests are performed in order to determine $E(U_y)$ by varying the values of vertical velocity U_y from 5×10^{-3} to 8×10^{-2}, while maintaining identical numerical conditions: Square domain size of 100 grid points, bubble diameter 50 grid points, density and viscosity ratio 10, surface tension

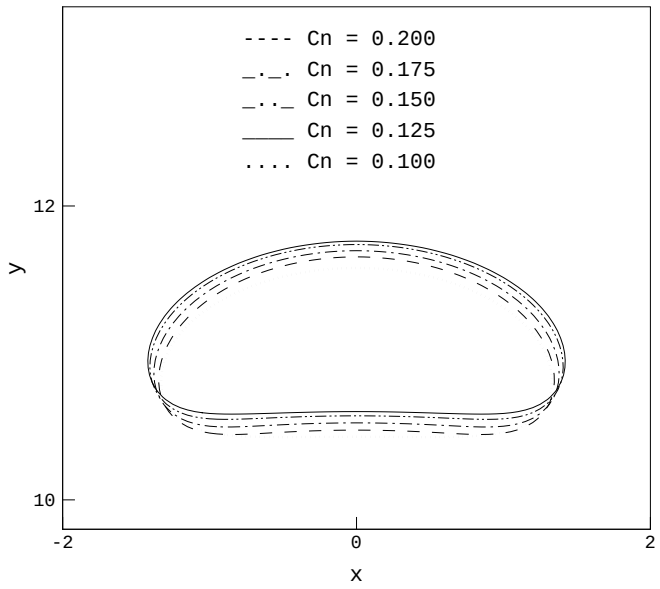

Figure 5.11: Effect of interface thickness on terminal shape at $T = 10$.

1×10^{-4} and relaxation time 0.5. As can be seen in the results plotted in Fig. 5.12, as the value of D increases, the dimensionless error remains unchanged and is parallel to second-order line. Therefore, the model used in this study satisfies Galilean invariance to second-order of accuracy in velocity, an expected and satisfactory accuracy for LBM.

5.2.6 Surface Tension Dependence

Surface tension is a measure of free energy per unit area at constant temperature. Evaluation of the effect of surface tension is performed by systematically changing the value of Bo. As described previously, Bo can be described as the dimensionless size of the bubble. Therefore, as Bo increases, inertia force has more influence on the bubble and higher deformation will be experienced by the bubble. Four different cases are performed at $Bo = 1$, 10, 100, and 1000. Terminal Re is maintained constant by changing the values of Mo accordingly. Results for final shape at $T = 10$ are presented in Fig. 5.13. As can be seen in the figure at $Bo = 1$, final shape remains

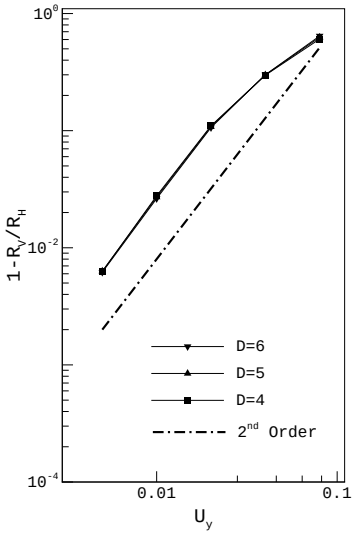

Figure 5.12: Dimensionless error as function of U_y with different interface thicknesses D at $50,000$ iterations. Domain size is 100×100, bubble radius $d_0 = 50$, $\rho_l = 1.0$, $\rho_g = 0.1$, $\tau_l = 0.5$ and $\tau_g = 0.5$.

almost spherical. When $Bo = 10$, the bubble is deformed mainly at the bottom, forming a spherical cap. The bubble becomes skirted when $Bo = 100$ and $Bo = 1000$, however, as can be seen when $Bo = 1000$ the skirt is wider, taller and thinner.

5.2.7 Application of Buoyancy Force Dependence

In order to establish the effect of the method of application of buoyancy force on the model, three different alternatives were explored. First, gravitational force $\mathbf{G}$ is defined so that the force is applied uniformly in all domain, $\mathbf{G} = -\rho g \nabla h$, as suggested by Takada *et al.* [69]. Second, force is defined so that it only affects the gas, equivalent to $\mathbf{G} = -(\rho - \rho_l) g \nabla h$. And, third, force is defined as it was suggested by Bunner and Tryggvason [75], $\mathbf{G} = -(\rho - \rho_{ave}) g \nabla h$, where ρ_{ave} is the average density, which is introduced to guarantee that the net momentum flux across the boundaries in the domain is zero. These three alternatives were tested in two different 2D cases, evaluating the possible change on deformation and terminal velocity. The parameters used in each case are as follows: test 1, $Bo = 32.2$, $Mo = 8.2 \times 10^{-4}$

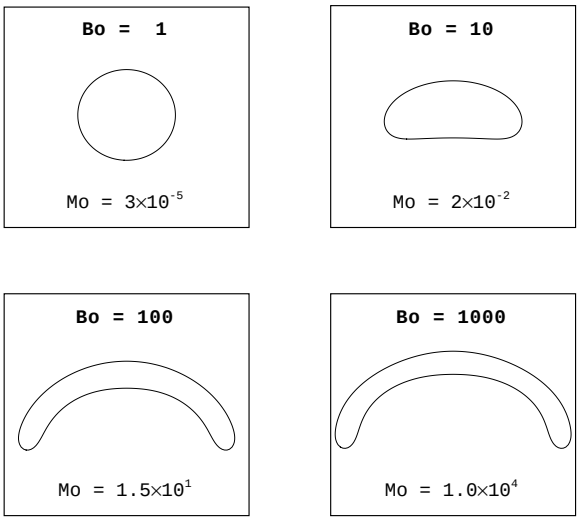

Figure 5.13: Effect of surface tension on terminal shape at $T = 10$.

and test 2, $Bo = 243$, $Mo = 266$. As can be seen in Fig. 5.14, the difference in the deformation in both test cases for the three alternatives is almost non-existent. In addition, the difference between the terminal Re is less than 1% in both test cases. This indicates that the method of application of buoyancy force in the system has no effect on the results for deformation and terminal velocity. This contradicts previous results obtained by Takada *et al.* [69], where a comparison study between VOF and LBM was performed for bubble rising. This study showed that LBM exhibited higher deformation than VOF, which was attributed to the uniformly applied buoyancy force in the LBM simulation.

5.3 Numerical Results

A new shape regime diagram based on Bo, Mo, and Re, was introduced by Bhaga and Weber [53]. This diagram has different locations for the transition lines and introduces additional shape regimes to the diagram introduced by Clift *et al.* [52]. This diagram is a rise velocity - volume relationship, represented as Re vs. Bo and

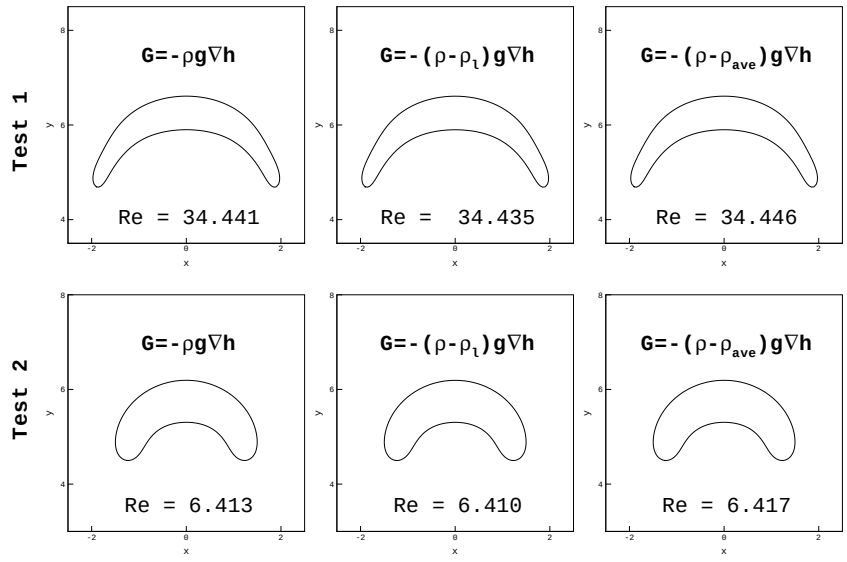

Figure 5.14: Effect of the method of application of buoyancy force at $T = 4.5$.

function of constant Mo. The new eight different shape regimes are: S, spherical; OE, oblate ellipsoid; OED, oblate ellipsoidal (disk-like and wobbling); OEC, oblate ellipsoidal cap; SCC, spherical cap with closed, steady wake; SCO, spherical cap with open, unsteady wake; SKS, skirted with smooth, steady skirt; SKW, skirted with wavy, unsteady skirt. The dynamics of single bubble rising has been previously explored numerically using LBM; however, previous studies have limited analysis on different flow regimes. In this study, numerical tests are performed by using LBM to simulate a case for each shape regime. Location of each test case in Bhaga's shape regime diagram is presented in Fig. 5.15. Table 5.1 provides the values of Bo and Mo used in each case. Five cases were selected from experimental results obtained by Bhaga and Weber. These cases are indicated with an asterisk * in the table.

5.3.1 Terminal Velocity and Shape

Results of 3D simulations are summarized in Tables 5.2 and 5.3. Table 5.2 provides a comparison between current 3D simulations and experimental results from Bhaga and

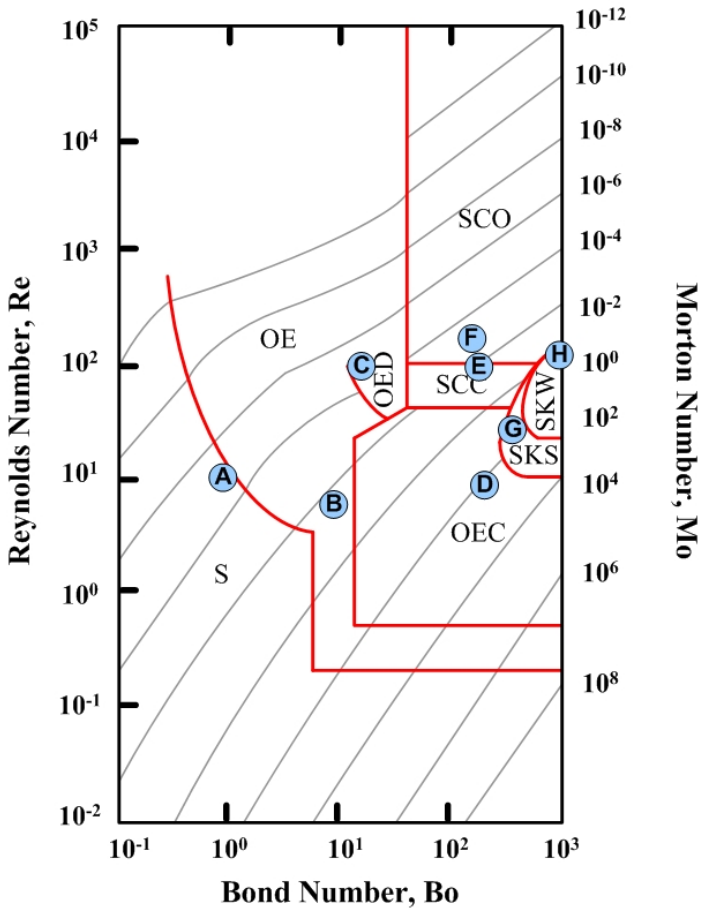

Figure 5.15: Shape regime map for bubbles in liquids: S, spherical; OE, oblate ellipsoid; OED, oblate ellipsoidal (disk-like and wobbling); OEC, oblate ellipsoidal cap; SCC, spherical cap with closed, steady wake; SCO, spherical cap with open, unsteady wake; SKS, skirted with smooth, steady skirt; SKW, skirted with wavy, unsteady skirt [53].

Table 5.1: Values of Bo and Mo.

Case	Bo	Mo
A Spherical	1.0×10^{0}	1.0×10^{-5}
B Oblate Ellipsoid	1.0×10^{1}	1.0×10^{-2}
C* Oblate Ellipsoidal Disk-like	3.2×10^{1}	8.2×10^{-4}
D* Oblate Ellipsoidal Cap	2.4×10^{2}	2.6×10^{2}

Case	Bo	Mo
E* Spherical Cap Closed Wake	1.2×10^{2}	4.6×10^{-3}
F Spherical Cap Open Wake	1.0×10^{2}	1.0×10^{-3}
G* Skirted Smooth Steady Skirt	3.4×10^{2}	4.3×10^{1}
H* Skirted Wavy Unsteady Skirt	6.4×10^{2}	4.3×10^{1}

Table 5.2: Comparison of 3D Simulation results and experimental results based on the study by Bhaga and Weber [53].

Case	Current Simulation Results	Experimental Results
C Re_{exp} = 55.3 Re_{sim} = 51.7		
D Re_{exp} = 7.8 Re_{sim} = 6.2	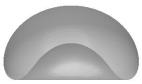	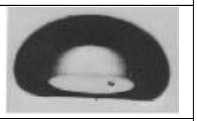
E Re_{exp} = 94.0 Re_{sim} = 78.9		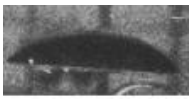
G Re_{exp} = 18.3 Re_{sim} = 15.2	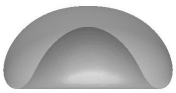	
H Re_{exp} = 30.3 Re_{sim} = 26.8		

Table 5.3: Comparison of 3D Simulation results and previous simulation results based on Hua *et al.* [65, 72] and Bonometti and Magnaudet [74].

Case	Current Simulated Results	Previous Simulation Results
A Re_{sim} = 8.9		 Case E [39] Re_{sim} ~ 10
B Re_{sim} = 9.5		 Case F [39] Re_{sim} ~ 10
C Re_{sim} = 51.7		 Case A2 [18] Re_{sim} = 54.8
D Re_{sim} = 6.2		 Case A3 [18] Re_{sim} = 7.6

Case	Current Simulated Results	Previous Simulation Results
E Re_{sim} = 78.9		 Case A8 [18] Re_{sim} = 88.7
F Re_{sim} = 106		 Case K [39] Re_{sim} ~ 100
G Re_{sim} = 15.2		 Case A5 [18] Re_{sim} = 17.8
H Re_{sim} = 26.8		 Case A5 [37] Re_{sim} = 29.9

Weber [53]. In this table, the first column provides the values of terminal Re obtained from the simulation and experimental results from Bhaga's shape regime map. The second column provides an illustration of the simulated final shape in each case. The third column provides experimental final shape in order to quantitatively compare the simulation results. Table 5.3 shows current results versus previous computational simulations. In this table, the first column provides the values of terminal Re obtained from the current simulation and simulation results based on Hua *et al.* [65], and [72] and Bonometti and Magnaudet [74]. The second column provides an illustration of the current simulated final shape in each case. The third column provides the final shape from previous simulation results. In general, simulation results for terminal Re tend to be slightly lower than experimental and previous simulation results. This pattern can be explained by three important factors: first, simulation domain was reduced in the radial direction to maintain computational cost reasonable. As shown in previous section, smaller radial size, provides lower terminal Re values. Second, experimental results were obtained based on small density ratio $\sim$ 1.5. However,

Table 5.4: Comparison of 3D simulation terminal Re results with different viscosity ratios.

CASE	**A** $\mathbf{Re_{exp} = 9.9}$	**B** $\mathbf{Re_{exp} = 10.1}$	**C** $\mathbf{Re_{exp} = 55.3}$	**D** $\mathbf{Re_{exp} = 7.8}$	**G** $\mathbf{Re_{exp} = 18.3}$	**H** $\mathbf{Re_{exp} = 30.3}$
$\mathbf{Re_{sim}}$ **at** $\mathbf{\lambda_1 = 100}$	$Re_{sim} = 7.6$	$Re_{sim} = 8.2$	$Re_{sim} = 47.8$	$Re_{sim} = 5.6$	$Re_{sim} = 13.5$	$Re_{sim} = 21.7$
$\mathbf{Re_{sim}}$ **at** λ_1	$Re_{sim} = 8.9$ $\lambda_1 = 1000$	$Re_{sim} = 9.5$ $\lambda_1 = 1000$	$Re_{sim} = 51.7$ $\lambda_1 = 200$	$Re_{sim} = 6.2$ $\lambda_1 = 500$	$Re_{sim} = 15.2$ $\lambda_1 = 500$	$Re_{sim} = 26.8$ $\lambda_1 = 300$

simulations were carried out with density ratio of 1000. Higher value of density ratio can also decrease the value of terminal Re, as it was shown in previous section. Third, experimental results were obtained with large viscosity ratio $\sim 10^4$. Simulation results were originally performed using a viscosity ratio of 100 producing low terminal Re. As shown in previous section, a high viscosity ratio is necessary to obtain high terminal Re values. Unfortunately, increasing the value of viscosity ratio creates instability in the simulation for cases with high Re and deformation. Therefore, computations with higher viscosity ratios were performed in most of the cases, while maintaining numerical stability, from 200 to 1000. It is noted that using a higher viscosity ratio provides a higher terminal Re, as shown in Table 5.4. Cases A and B were performed using a viscosity ratio of 1000, increasing the terminal Re by 15%. Cases D and G were run with viscosity ratio of 500 raising terminal Re by at least 10%. Case H was done using viscosity ratio of 300, improving terminal Re by 20%. Case C was performed with viscosity ratio of 200, increasing terminal Re by 7.5%. Unfortunately, numerical stability was not reached for cases E and F. However, it is estimated that if this stability issue is resolved, the terminal Re would be raised in order to obtain more accurate results. Final simulation shapes are compared using second and third columns in Tables 5.2 and 5.3. It is the purpose of the comparison to gauge the capability of the model in order to capture the topological changes based on initial values of Bo and Mo. Variation of Bo and Mo provides a change on deformation and velocity, respectively. Deformation is directly proportional to Bo and velocity is

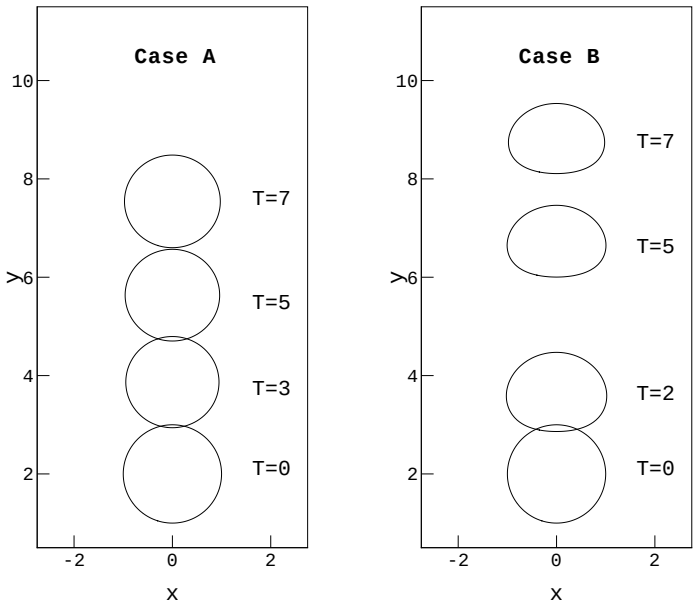

Figure 5.16: Shape and position evolution for cases A and B.

inversely proportional to Mo. Cases A and B have the lowest values of Bo therefore they experience the least amount of deformation. These cases are governed mainly by viscous and surface tension forces. On the other hand, cases E, F, G, and H have the highest value of Bo exhibiting greater deformation. These cases are dominated by inertia. However, cases E and F have lower values of Mo, therefore terminal Re tends to be higher. In addition, simulated results for these cases show that the bubble is transformed from a spherical cap to a toroidal bubble. Although these results are different from an experimental solution, this transformation has been obtained by other numerical studies, including [74], [72], and [63]. Bonometti and Magnaudet [63] established that the transition from spherical cap to a toroidal shape is very sensitive to grid resolution. Therefore, in order to capture a more accurate transition process, it is necessary to increase the grid resolution significantly. Overall, simulated final shapes exhibit the desired topological changes as described experimentally [53] and numerically [65], [72], and [74].

In order to provide a better description of the topological changes encountered in each case, Figs. 5.16 to 5.19 are presented. These figures provide the evolution of the

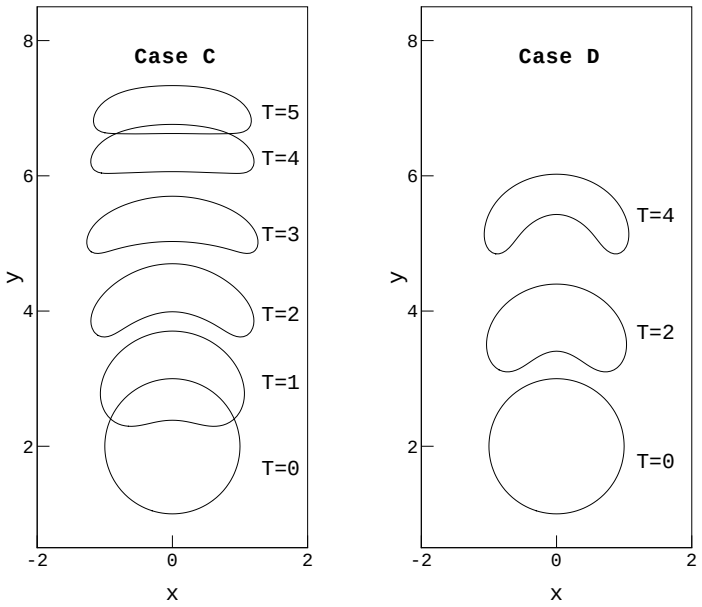

Figure 5.17: Shape and position evolution for cases C and D.

shape and the position for each case. As can be seen in Fig. 5.16, case A remains spherical throughout the trajectory. On the other hand, case B starts to have a deformation in the lower surface around $T = 2$ until it reaches an oblate ellipsoidal shape. Fig. 5.17 shows the evolution for cases C and D. In case C, bottom surface of the bubble starts to deform pushing side surfaces outward, creating a disk-like shape. In case D, the bottom surface is deformed until an oblate ellipsoidal cap is formed. Note that the bubble in case C reaches a higher position than in case D at the same T, due to a higher value of Re. Fig. 5.18 presents the evolution of the spherical cap cases E and F. As mentioned previously, these two cases transform from a spherical cap to a toroidal shape. This transformation takes place sooner in case F, due to its higher Re and its unsteady wake. Fig. 5.19 shows the evolution of the skirted cases G and H. The bottom surface of the bubble in case H has a higher deformation throughout the trajectory, due to a higher value of Bo, making inertia the dominating force in the system.

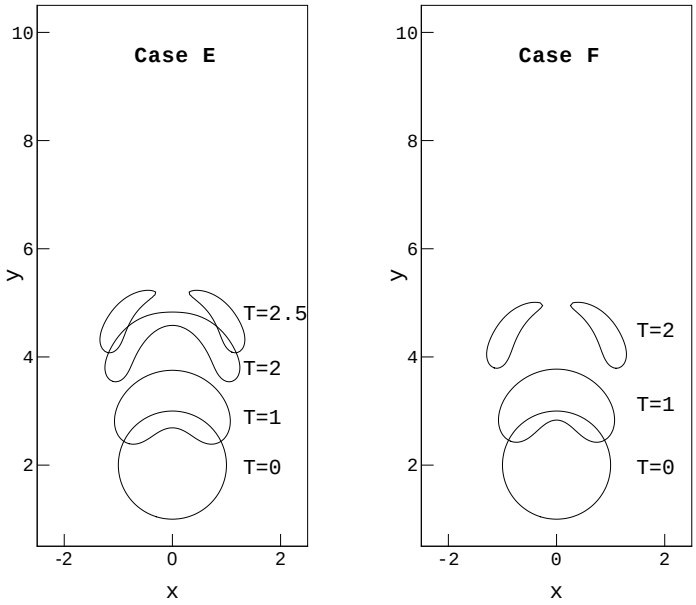

Figure 5.18: Shape and position evolution for cases E and F.

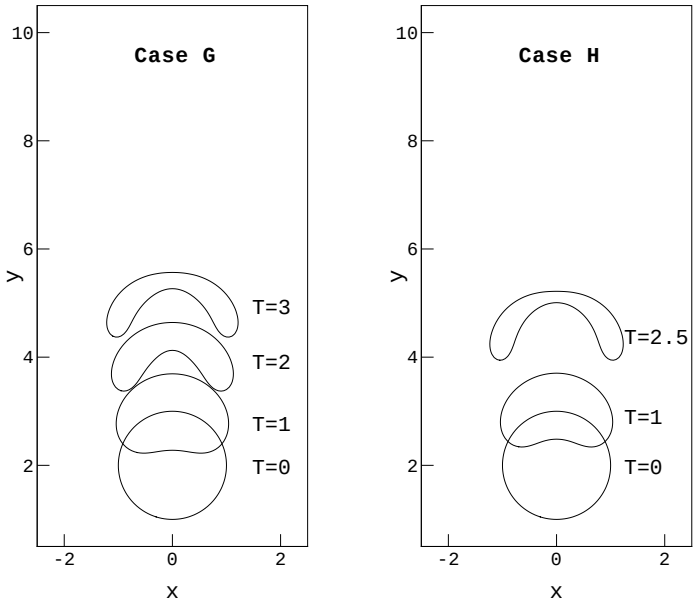

Figure 5.19: Shape and position evolution for cases G and H.

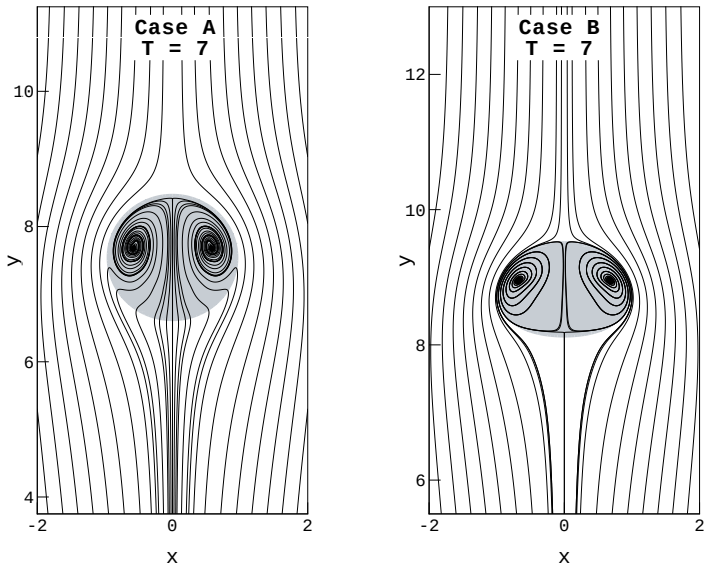

Figure 5.20: Streamlines for cases A and B.

Velocity and Pressure Fields

Figs. 5.20 to 5.23 present the streamlines for each case, at their final T. A closed toroidal wake region is formed at the back of the bubble as it rises. A recirculation pattern is produced within the wake. This wake is related to the degree of deformation, terminal Re, and the size of the bubble. Experimental observation of this wake region was performed by Bhaga and Weber [53] using H_2 tracers. It was noted that at higher volume, deformation, and Re, a larger wake region was formed. Cases A undergoes very little deformation and case B has a flatter bottom surface. Therefore, the wake produced behind the bubble is very small. Streamlines surround the periphery of the bubble, as could be seen in Fig. 5.20. On the other hand, cases G and H have high Re and deformation, therefore the wake region is larger. Another factor to quantify the wake size is the value of Bo, since it could be considered as the dimensionless size of the bubble. As Bo increases, so does the toroidal wake. Therefore, when comparing wake size between case E and F, and G and H, cases E and H will have higher wake regions since their Bo values are also higher, see Figs. 5.22

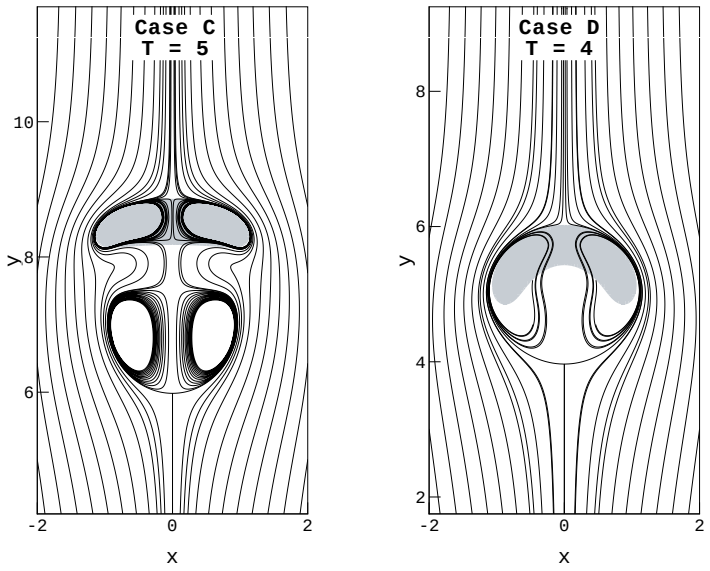

Figure 5.21: Streamlines for cases C and D.

and 5.23.

As can be seen from Fig. 5.21, case C experiences an open wake, unlike other cases. It is believed that this case has crossed the transition point from closed to open wake. Different experimental studies have been performed to determine the transition from a closed, steady to an open wake region. Bhaga and Weber [53] indicate that for high Mo cases, the transition is believed to occur at $Re = 110$. However, for low Mo, this transition is a function of other factors such as the Weber number, defined as $We = Re^2\sqrt{Mo}/\sqrt{Bo}$. In their study, the critical value to describe high or low Mo is given by $Mo = 4 \times 10^{-3}$. Case C has a $Mo = 8.2 \times 10^{-4}$, which is considered as a low Mo case, therefore it is possible that at its terminal Re, the bubble has crossed the transition point.

Figs. 5.24 to 5.31 provide three different pressure contours: Total pressure (P_{tot}), sum of static and dynamic part (P), and sum of thermodynamic part (p_0) and curvature part (p_c). These figures have been non-dimensionalized using $\frac{P_i - P_{top}}{0.5\rho_l U_c^2}$, where P_i is the pressure in each contour, P_{top} is the pressure value at highest point in the domain, far away from the bubble and U_c is the characteristic velocity of the system defined

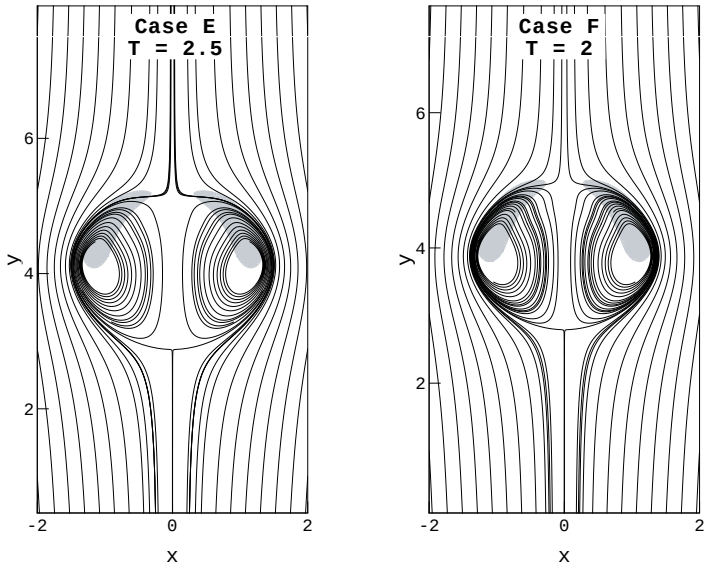

Figure 5.22: Streamlines for cases E and F.

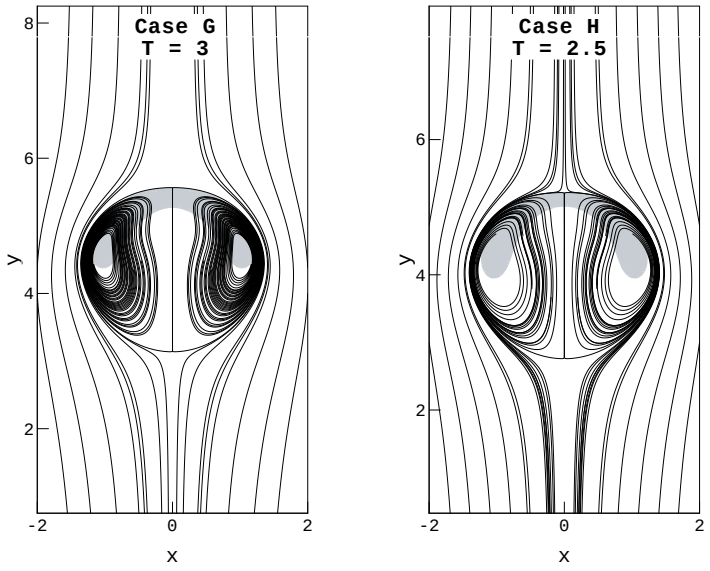

Figure 5.23: Streamlines for cases G and H.

as $U_{c1} = \sqrt{gd_0}$. These results emphasize the idea that thermodynamic properties are independent of the dynamic pressure, since $p_1/p_0 \sim O(Ma^2)$. This can also be seen in the contours P_{tot}, which are very similar to the ones of P, indicating that p_0 and p_c have very little effect on the total pressure of the system. Another important observation can be done by comparing the contour values between the cases. Cases A, B and C, have high range values of p_0 and p_c, indicating the primary forces acting on the system are surface forces. This corresponds to low values of Bo, where surface tension is higher. These three cases have a range of $Bo < 35$, see Figs. 5.24 to 5.26. On the other hand, cases G and H, have low range values p_0 and p_c, indicating that surface tension is not the primary force in the system. These cases have large Bo, which makes inertia the driving force in the system. In general, the range level of P remains very close in all the cases. In addition, it can be noticed that higher values of P are concentrated at the top surface of the bubble. This indicates that at that point, the bubble is trying to push away liquid in order to keep rising.

Drag Coefficient

As the bubble rises, there are two main forces acting on the system: buoyancy and drag. Buoyancy is the driving force and drag is the force that opposes the bubble motion. The rising bubble reaches a point where these two forces are balanced, reaching a steady velocity, known as terminal velocity. Studies have been performed to relate the terminal velocity with drag force. Using experimental studies, Bhaga and Weber [53] established a relationship between the drag coefficient C_d and Re, limited to large values of $Mo > 4 \times 10^{-3}$. The relationship between C_d and Re is given by:

$$C_d = \left[(2.67)^{0.9} + \left(\frac{16}{Re} \right)^{0.9} \right]^{\frac{1}{0.9}}. \tag{5.8}$$

Using the principle that terminal velocity is reached when drag and buoyancy forces are balanced, a theoretical relationship can be established between U_t and C_d. Buoyancy force can be estimated as weight of a spherical bubble $F_{bu} = \pi d_0^3 \Delta\rho g/6$ and drag force can be calculated using $F_{dr} = -\rho U_t^2 A C_d/2$, where A is the cross-sectional

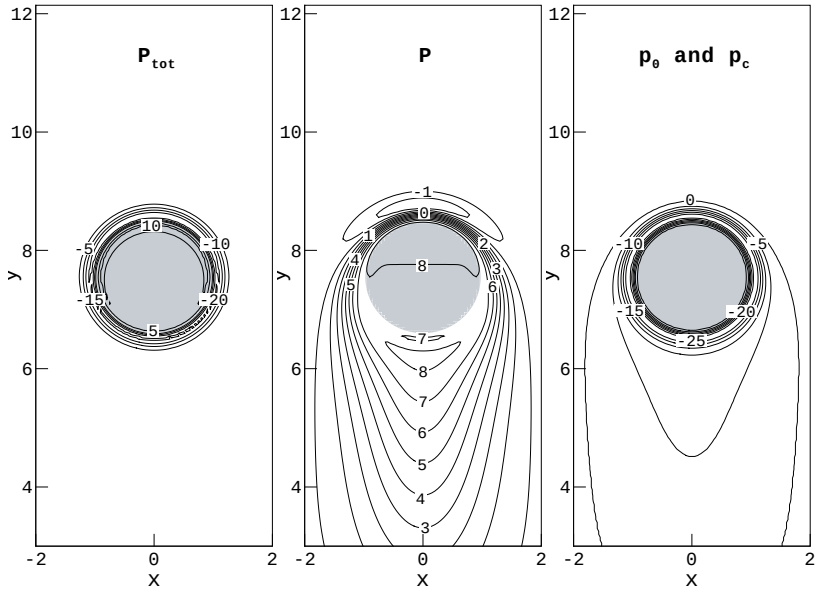

Figure 5.24: Pressure contours for case A. P_{tot} is total pressure, P is the sum of static and dynamic part, p_0 is the thermodynamic part, and p_c is the curvature part.

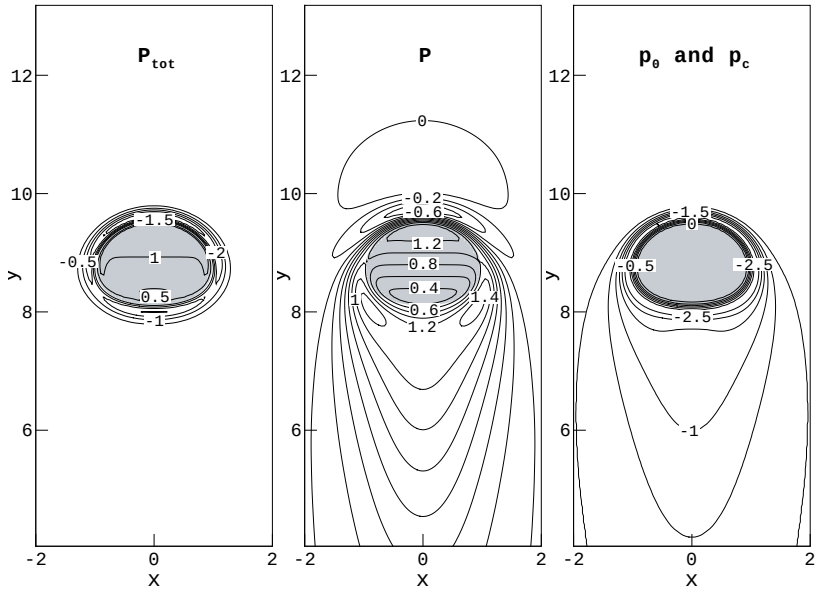

Figure 5.25: Pressure contours for case B. P_{tot} is total pressure, P is the sum of static and dynamic part, p_0 is the thermodynamic part, and p_c is the curvature part.

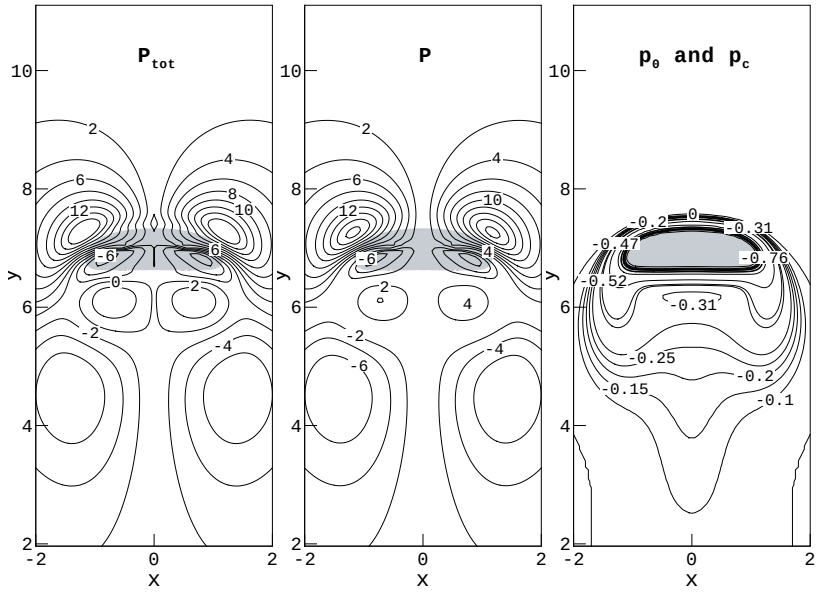

Figure 5.26: Pressure contours for case C. P_{tot} is total pressure, P is the sum of static and dynamic part, p_0 is the thermodynamic part, and p_c is the curvature part.

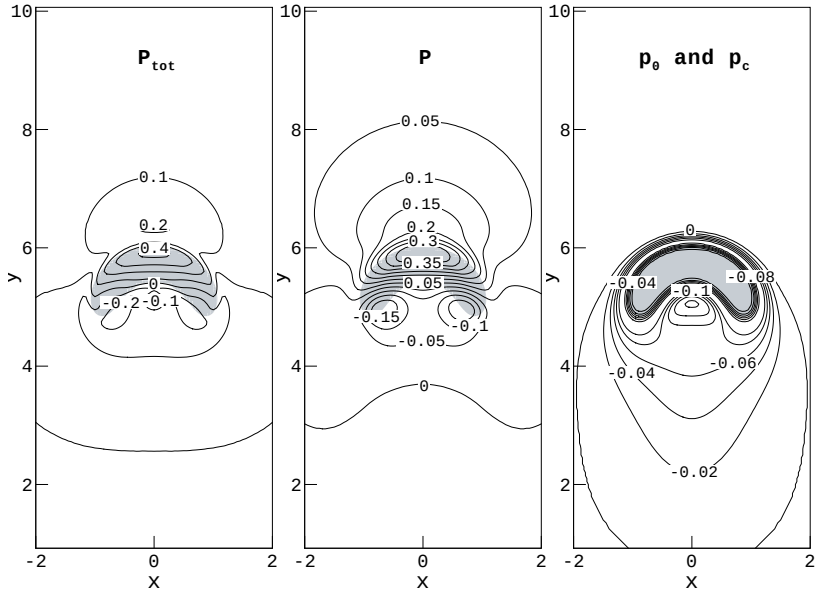

Figure 5.27: Pressure contours for case D. P_{tot} is total pressure, P is the sum of static and dynamic part, p_0 is the thermodynamic part, and p_c is the curvature part.

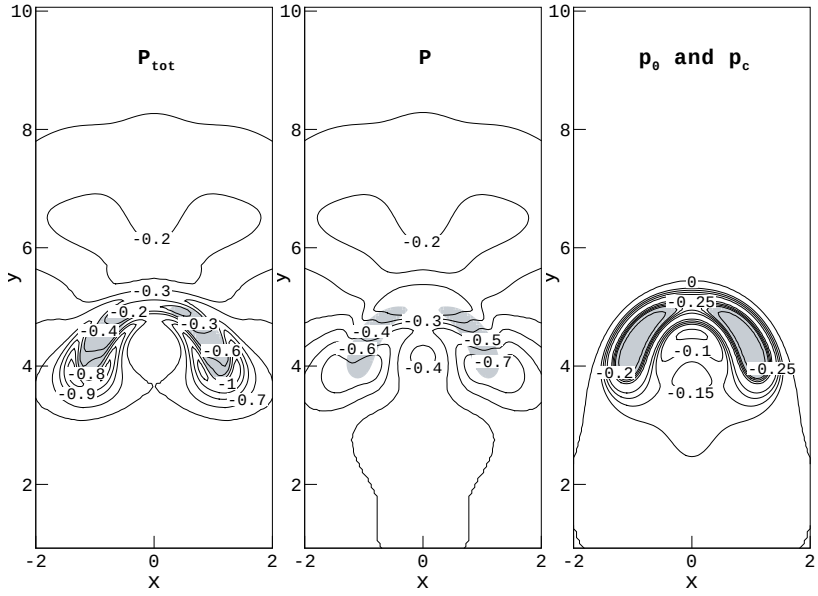

Figure 5.28: Pressure contours for case E. P_{tot} is total pressure, P is the sum of static and dynamic part, p_0 is the thermodynamic part, and p_c is the curvature part.

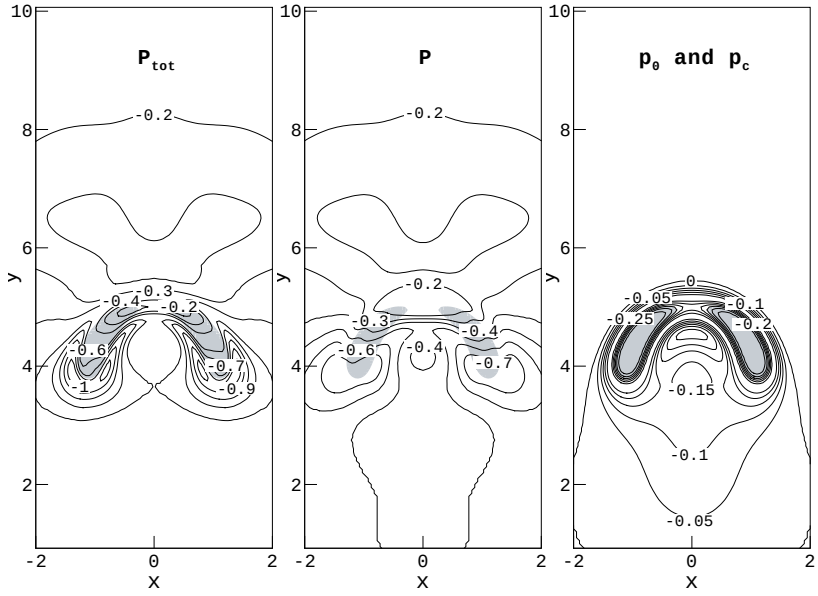

Figure 5.29: Pressure contours for case F. P_{tot} is total pressure, P is the sum of static and dynamic part, p_0 is the thermodynamic part, and p_c is the curvature part.

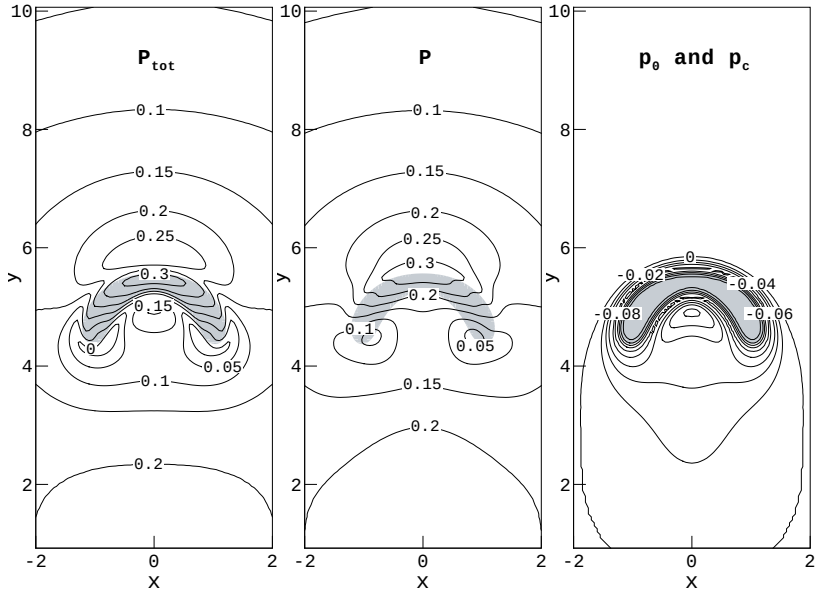

Figure 5.30: Pressure contours for case G. P_{tot} is total pressure, P is the sum of static and dynamic part, p_0 is the thermodynamic part, and p_c is the curvature part.

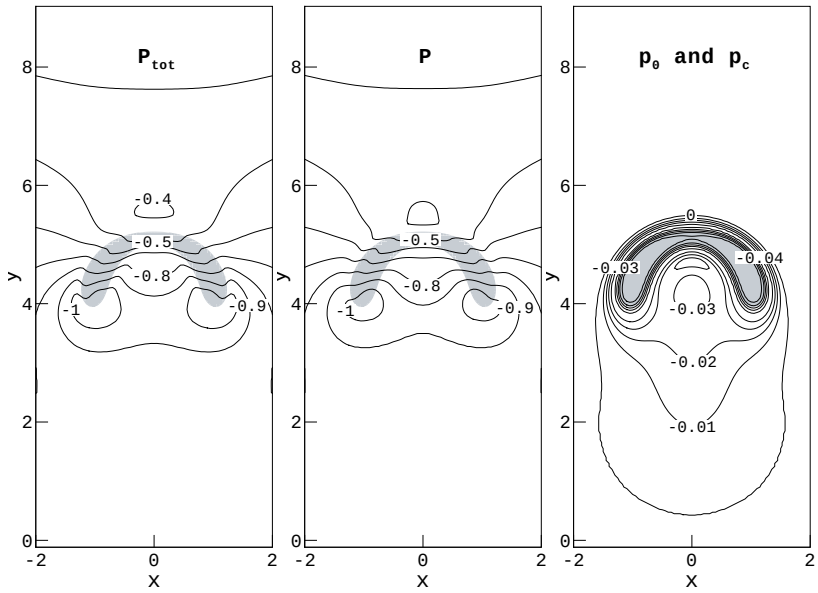

Figure 5.31: Pressure contours for case H. P_{tot} is total pressure, P is the sum of static and dynamic part, p_0 is the thermodynamic part, and p_c is the curvature part.

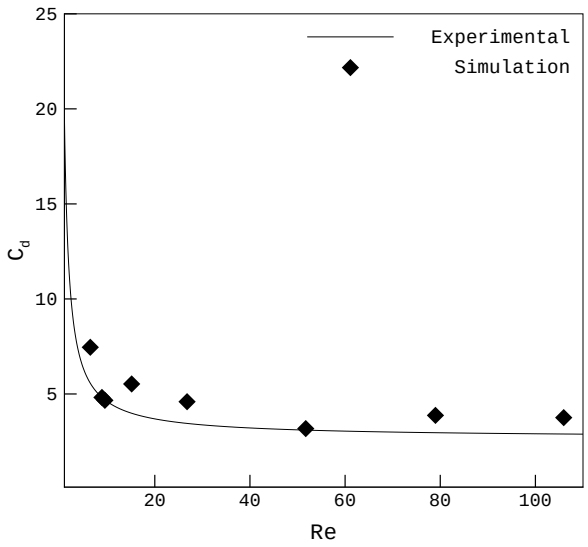

Figure 5.32: Drag coefficient comparison between experimental results from Bhaga and Weber [53] and simulation results.

area normal to the bubble motion. Using these definitions, a theoretical relationship between C_d and U_t is given by

$$C_d = \frac{4\Delta\rho g d_0}{3U_t^2\rho_l}. \tag{5.9}$$

Simulation results are compared to experimental correlation Eq. (5.8), based on the constraint that $Mo > 1 \times 10^{-4}$. Comparison was performed by calculating C_d using theoretical relationship given in Eq. (5.9), using numerical values for U_t. As can be seen in Fig. 5.32, simulation results are in good agreement with experimental correlation.

5.3.2 Comparison with Correlation

Rodrigue [76] proposed a simple correlation for the dynamics of bubble rising in a pure viscous fluid, obtaining terminal velocity as function of physical parameters. This correlation was obtained using a dimensional analysis on experimental results from 19 studies, covering a large range of physical parameters, such as ρ_l, η_l, σ, Re,

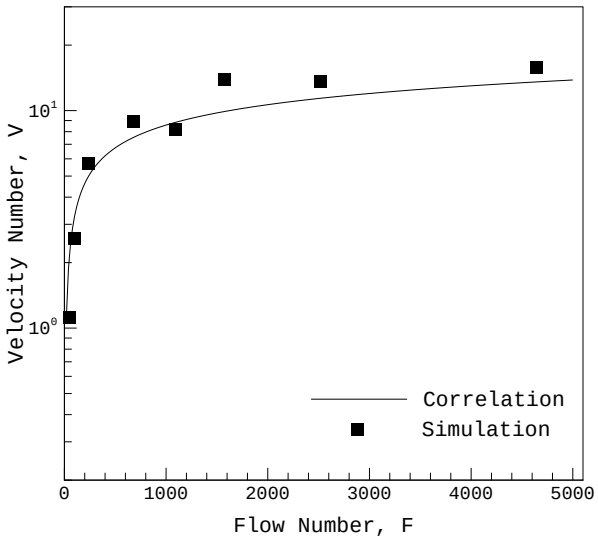

Figure 5.33: Comparison of velocity number for simulation results and correlation [76].

and Mo. Bubble motion is described using two non-dimensional numbers obtained from this study:

Flow number:

$$F = g\left[\frac{d_0^8\rho_l^5}{\sigma\eta_l^4}\right]^{1/3} = Bo\left(\frac{Re}{Ca}\right)^{2/3}, \tag{5.10}$$

and *Velocity number:*

$$V = U_t\left[\frac{d_0^2\rho_l^2}{\sigma\eta_l}\right]^{1/3} = (Re^2Ca)^{1/3}, \tag{5.11}$$

where $Ca = \frac{\eta_l U_t}{\sigma}$ is the capillary number. Rodrigue [76] proposed a new correlation between these two non-dimensional numbers in the form of

$$V = \frac{a_1 F^{b_1}}{1 + c_1 F^{d_1}}, \tag{5.12}$$

where $a_1 = 1/12$, $b_1 = 1$, $c_1 = 49/1000$ and $d_1 = 3/4$.

A comparison between current numerical results and this correlation is performed to test the ability of LBM to predict V for a large range of physical parameters, and

it is shown in Fig. 5.33. In general, there is a reasonable agreement between the numerical results and the correlation. This indicates that numerical simulation can predict an important non-dimensional number, which is related to terminal velocity, a factor that described the dynamic behavior of a rising bubble.

In summary, a $2D$ analysis is performed in order to establish the dependence on physical and numerical parameters such as density ratio, viscosity ratio, surface tension, interface thickness, and domain size. In addition, a $3D$ analysis was performed by simulating a case for each of the eight different shape regimes introduced by Bhaga and Weber [53]. These analyses are a suitable foundation for the understanding of dynamics of multiphase systems. The next stage is to add the complexity of confinement, in order to investigate the effect of wall in the evolution on the flow.

Chapter 6

Single Bubble Rising in a Square Channel

The second stage is to introduce the effect of the walls by evaluating the dynamics of a bubble rising on a vertical and inclined square channel. The driving force is this stage is the buoyancy force in the system.

6.1 Background

The flow of a bubble rising in a liquid-filled channel has many practical and industrial applications in enhanced oil recovery [84, 85], trickle-bed reactors [86], monolithic structures [8], biomedical applications [87, 88], and microelectronic cooling systems [89]. For this reason, the motion of bubbles in vertical capillaries with circular and square cross-sections has been studied experimentally, theoretically, and numerically. Experimentally, Taylor [90] performed a study to measure the fluid film thickness in circular capillaries. This study established that the value of film thickness converged to a constant value as a critical value of the capillary number Ca was reached. A complementary study for low viscosity fluids and high velocity cases was presented by Aussillous and Quéré [91]. This study proposed a first order analysis in order to describe the film thickness for cases at high velocity which tended to deviate

from Taylor's law [90]. This deviation was attributed to the effect of inertia. Thulasidas *et al.* [96] performed an experimental and computational analysis to calculate the main mass transfer in the bubble train flow process for circular and square capillaries. Liquid film thickness and gas-liquid areas were determined experimentally for different flow rates. An iterative scheme was used to find the velocity of the bubble and liquid slugs, as well as the volume fraction of liquid inside of channel. Later, Thulasidas *et al.* [97] performed a theoretical and experimental study of the dynamics of a bubble-train flow inside circular and square capillaries. This study provided a description of the velocity profiles for a wide range values of Ca. Clanet *et al.* [98] carried out an analytical and experimental study for rising bubbles in arbitrary cross section tubes. This study presented a relationship between the rising velocity (U_t) of a bubble and the geometrical properties of the tube. The results of this study were divided into two domains based on the value of the Reynolds number, defined as $Re_s = \frac{U_t S \rho}{Pr\eta}$, where S is the cross sectional area, Pr is the perimeter of the channel, ρ and η are the density and dynamic viscosity of the liquid, respectively. In the low Re_s domain, U_t is related to the geometrical properties by $U_t = 0.012gS/\nu$ where g is the gravity. In the high Re_s domain, the relation is given by $U_t = \sqrt{8\pi gPr}$. Recently, Li *et al.* [99] introduced a study for bubble rising under the influence of gravity for different bubble sizes. This study proposed a relationship between the Weber number We and important flow parameters such as bubble velocity, bubble deformation, and film thickness.

Theoretically, Bretherton [100] used lubrication theory to analyze a long bubble in circular tubes with low Ca ($Ca < 10^{-4}$), treating it as a tight fitting piston problem. In this study a power-law relationship between wetting film thickness and Ca was presented. An extension of this study was presented by Reinelt and Saffman [101] introducing a theoretical and computational analysis for cases up to $Ca < 10^{-1}$. In addition, Ratulowski and Chang [102] performed a study which used an arclength-angle formulation of a modified lubrication equation to compute the pressure drop and wetting film thickness for single bubble in circular and square capillaries at higher Ca. For cases with $Ca < 10^{-1}$, the pressure drop results agreed with study presented by Reinelt and Saffman [101]. Kolb and Cerro [103] developed a film evolution equation

for long bubbles in square channels. This equation can be coupled with the Young-Laplace equation to provide a complete set of equations to describe the interface profile for large values of Ca and Bo.

Numerically, Bugg *et al.* [104] introduced an analysis based on finite difference method to evaluate the dynamic behavior of the gas-liquid interface for large range of Bo and Mo in circular capillaries. The predictions for bubble velocity and film thickness were in good agreement with experimental results. Yang *et al.* [105] presented an investigation of bubbly flow in a narrow channel based on the lattice Boltzmann equation (LBE) method. The focus of this paper was small channels, where the capillary forces are dominant. For a single Taylor bubble, simulation results for film thickness were in good agreement with analytical correlation given by Bretherton [100]. This correlation describes film thickness y as function of Ca, using $y/H = 1.337Ca^{\frac{2}{3}}$, where H is half of hydraulic diameter. Hazel and Heil [106] presented a study based on the finite element method to evaluate the shape and pressure drop across the tip of a long bubble in tubes of elliptical and rectangular cross-sections. This study is in good agreement with the theoretical work presented by Wong *et al.* [107] for pressure drop in low Ca cases in rectangular channels. It also showed that gravity tended to affect the fluid film deposited behind the rising bubble. As the gravity increases, more fluid accumulates at the film region, therefore increasing pressure drop across the tip of the bubble. Taha and Cui [29] performed a computational analysis using FLUENT focusing on slug flows. This study provided a relationship between Ca and the shape and velocity field of the bubble.

Dynamics of rising bubbles in inclined capillaries with circular and square cross-sections has been studied experimentally and numerically as well. Experimentally, Zukoski [108] showed that the influence of surface tension was higher than that of viscosity in the evolution of velocity for a long bubble. This study also observed the influence of the inclination on the dynamic behavior of the bubble. It showed that the velocity of the bubble reached a maximum value when the inclination of the tube was around 45°, and that at a constant inclination the velocity of the bubble decreased with surface tension. Later, Maneri and Zuber [109] performed a study on two-dimensional bubbles and determined that bubble rising motion could be classified

into three regimes depending the angle of inclination. In addition, this study showed that the wall effect decreased as the inclination increased. More recently, Shosho and Ryan [110] introduced a study for bubble rising in inclined tubes in Newtonian and Non-Newtonian fluids as a function of the Froude number Fr, Bo and Mo. This study corroborated the findings from Zukoski [108] where a maximum value of Fr was reached, as the value of inclination reached a critical value around 45°. Furthermore, it was found that the critical inclination angle reduced with the value of Mo and Fr increased with Bo. In general, values for Fr tend to be lower for Non-Newtonian fluids. Norman and Miksis [111] performed a two-dimensional computational study using a level set finite difference method. This study discussed the effect of Bo, Re and inclination on the final shape of the bubble and the distance from the wall. At low inclination, bubble reaches a steady shape and remains at a constant distance away from the wall. Once the inclination has reached a critical value at intermediate Bo, the bubble starts bouncing within the channel. At Bo higher than the critical value, the bubble becomes unstable and breaks up. DeBisschop *et al.* [112] performed a two-dimensional study using boundary integral method with and without insoluble surfactant. In the cases without surfactant, it was noticed that increasing Bo increased the deformation and the final velocity of the bubble. In the case with surfactant, the bubble tended to be more elongated and slender, therefore increasing the distance between the bubble and the wall.

6.2 Test Cases and Computational Setup

The simulation cases were selected from the experimental study performed by Li *et al.* [99]. The experimental study was performed using solutions based on glycerine and sodium iodide at different viscosities. The notation used in the experiment cases is also used in the present study to maintain consistency. *GW* denotes glycerine solutions and *SO* denotes sodium iodide. Each case is followed by a number, which was used to distinguish different viscosity levels in the experiment. In the cases of *GW*, channels with different cross-sectional dimensions are used and they are labeled as *-1* and *-2*. *SO* cases have only one cross-sectional dimensions. Table 6.1 shows

CASE	BO	MO	ρ_{ratio}	CASE	BO	MO	ρ_{ratio}
GW1-1	5.4	$8.1x10^{-4}$	907.5	**GW5-2**	10.4	$8.3x10^{-1}$	1051
GW2-1	5.3	$4.9x10^{-3}$	947.5	**SO2**	9.3	$6.1x10^{-2}$	790.0
GW3-1	4.8	$1.7x10^{-1}$	997.7	**SO3**	10.8	$3.7x10^{0}$	907.5
GW2-2	11.8	$4.9x10^{-3}$	947.5	**SO4**	11.2	$7.0x10^{1}$	790.0
GW3-2	10.8	$1.7x10^{-1}$	997.7	**SO5**	11.2	$7.2x10^{2}$	798.3
GW4-2	10.3	$3.4x10^{-1}$	1016	**SO6**	11.4	$7.8x10^{3}$	849.2

Table 6.1: Values of Bo, Mo and density ratio in each case from experimental study by Li *et al.* [99].

the different cases used in the current study with non-dimensional numbers Mo and Bo. Bo is defined using R_c which is the characteristic length chosen to be half of the hydraulic diameter D_h. For a square channel D_h is the channel width. η_l is the dynamic viscosity of liquid. The dimensionless bubble size is described as $k = \frac{a}{R_c}$, where a is the radius of the spherical bubble. Each of the cases performed in this study uses four non-dimensionless bubble sizes, $k = 0.6$, $k = 0.8$, $k = 1.05$, and $k = 1.25$. In the current study the density ratio is the same as the experimental values, as it was shown in Table 6.1. However, the viscosity ratio is fixed at 100 to maintain numerical stability. Amaya-Bower and Lee [77] showed that when the viscosity ratio is larger than 100, the solution does not depend on the viscosity ratio.

The experiments were performed using channels of length at least 30 times their hydraulic diameter. Simulation of this aspect ratio will create a prohibitively high computational cost. Therefore, a domain size analysis is performed to establish the minimum acceptable channel length that can be used while maintaining accuracy in the results. The domain size analysis is done by comparing two non-dimensional physical parameters at four different channel lengths, $10R_c$, $15R_c$, $20R_c$, and $30R_c$ for the case *GW1-1*. These parameters are the film thickness δ and the deformation parameter Δ. δ is defined as the minimum thickness between the bubble and the wall

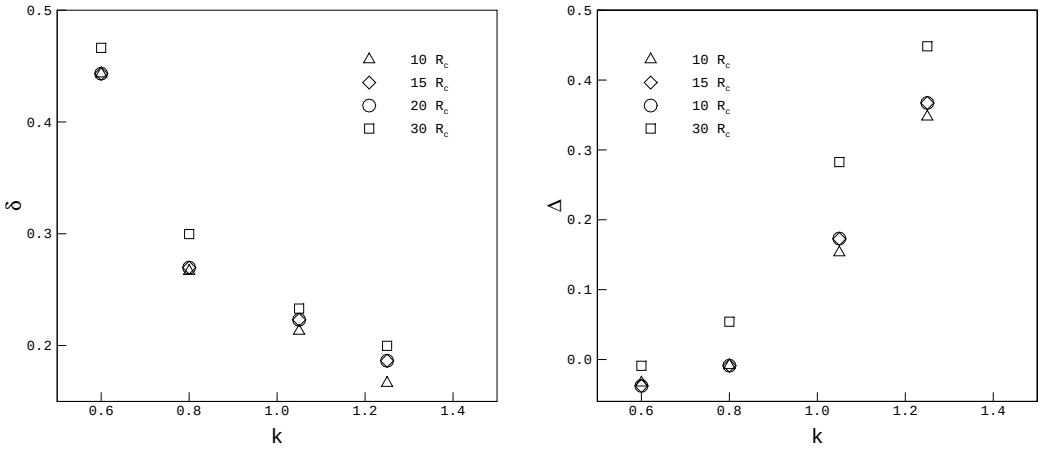

(a) Film Thickness δ (b) Deformation Parameter Δ

Figure 6.1: Effect of channel length on non-dimensional parameters in (a) film thickness δ and (b) deformation parameter Δ at $T = 10$ for case *GW1-1*. The channel lengths are $10R_c$, $15R_c$, $20R_c$ and $30R_c$.

divided by R_c. Δ is the ratio based on the length L_{bu} and width W_{bu} of the bubble, defined as $\Delta = \frac{L_{bu}-W_{bu}}{L_{bu}+W_{bu}}$. The results of the analysis are shown in Fig. 6.1a for δ and in Fig. 6.1b for Δ. Note that plots presented in this task use non-dimensional time $T = t/t_{n2}$, where $t_{n2} = \sqrt{R_c/g}$. As it can be observed from these plots, the results for $k < 1$ are very close to each other when the channel lengths are $\leq 20R_c$, and they are different from the channel length for $30R_c$ by less than 7%. Therefore, for cases where $k < 1$, a channel length of $10R_c$ will be used. However, this channel length has a higher effect on the cases where $k > 1$, for which $15R_c$ will be used. The results obtained with a channel length of $15R_c$ are very similar to those with $20R_c$.

A grid resolution analysis was performed keeping the channel aspect ratio constant at $2R_c \times 15R_c \times 2R_c$ for case *SO4* at inclination of 75°. The grids used in this analysis were $60 \times 450 \times 60$, $90 \times 635 \times 90$, and $120 \times 900 \times 120$. As shown in Fig. 6.2, the final shape in the coarse grid has only a slight difference at the top and bottom of the bubble from the finer grids and overall the shape is properly maintained. Considering the results given by this analysis, it is determined that using the $60 \times 450 \times 60$ grid in this study, corresponding to $R_c = 30$ would provide reasonable accuracy and avoid high computational cost.

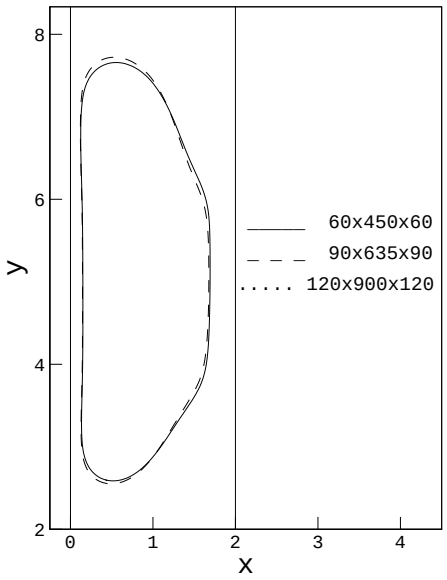

Figure 6.2: Effect of grid resolution on final shape at T = 10 for case *SO4* at inclination of 75°.

Simulations with different equilibrium contact angles ranging from 30° to 150° were performed but there was no noticeable difference in the bubble deformation and the values of δ and Δ. Therefore, we will fix the equilibrium contact angle at 150° for all the cases of vertical and inclined channels.

6.3 Validation: Comparison with Experimental Results

The steady shapes of the bubble for four different cases *GW2-2*, *GW3-2*, *GW4-2*, and *SO4* are compared with the experimental results [99]. This comparison is shown in Figs. 6.3a to 6.3d. In general, the computed steady shapes present the basic features of the experimental bubble shapes. For $k = 0.6$, the bubble tends to remain spherical, as it is for cases *GW3-2*, *GW4-2*, and *SO4*. However, in case *GW2-2* the final shape is a spherical cap. For $k = 0.8$, the bubble tends to take an elongated mushroom shape, as it is for cases *GW2-2*, *GW3-2*, and *SO4*. In the case of *GW4-2* final shape

becomes an elongated egg. For $k = 1.05$ the bubble tends to take a bullet shape for all of the cases. Lastly, for $k = 1.25$ the bubble transforms into a slug shape.

The values of δ and Δ for two experimental cases *GW2-2* and *GW4-2* are also compared with the LBE simulations. Comparison between simulation and experimental results is shown in Fig. 6.4a for δ and in Fig. 6.4b for Δ. As can be seen from these plots, the results from the LBE simulations are in good agreement with the experimental results by Li *et al.* [99]. In general, the simulation results capture the trend between k and the non-dimensional parameters. As the value of k increases δ decreases and Δ increases. This provides a good level of confidence on the accuracy of the simulation results.

All the numerical results are organized into three groups in order to keep the cases within similar ranges of Ca. The three groups in the increasing order of Ca are: three cases for *GW-1*, four cases for *GW-2*, and five cases of *SO*. The following sections will examine the effect of k on the main physical characteristic of the rising bubble, namely the final shape, δ, and Δ. In addition, the streamlines, vorticity and pressure contours of all the cases at $k = 1.25$ will be presented.

6.4 Final Shape

Figs. 6.5a to 6.8c show the results for all the cases organized by the increasing order of Ca in each group for each non-dimensional size k. Each of the figures includes the final shape of each case as well as the values of non-dimensional numbers in the simulation, such as Weber number We, δ, Δ, and Reynolds number Re based on R_c. We is the ratio between inertia and surface tension and it is defined as $We = \frac{\rho_l U_t^2 R_c}{\sigma}$

Looking closely at the final shapes of the bubble, interesting conclusions can be drawn. In all the figures, Ca increases and We and Re decrease from left to right. This indicates that effect of inertia and surface tension is being reduced as the viscous effect is increased in the same direction. For $k = 0.6$, bubble tends to remain spherical except for case *GW2-2*. This case corresponds to the highest We and Re, indicating that the surface tension and viscous effect are lower than other cases. The reduction of viscosity and surface tension promotes higher deformation in the bubble. In cases

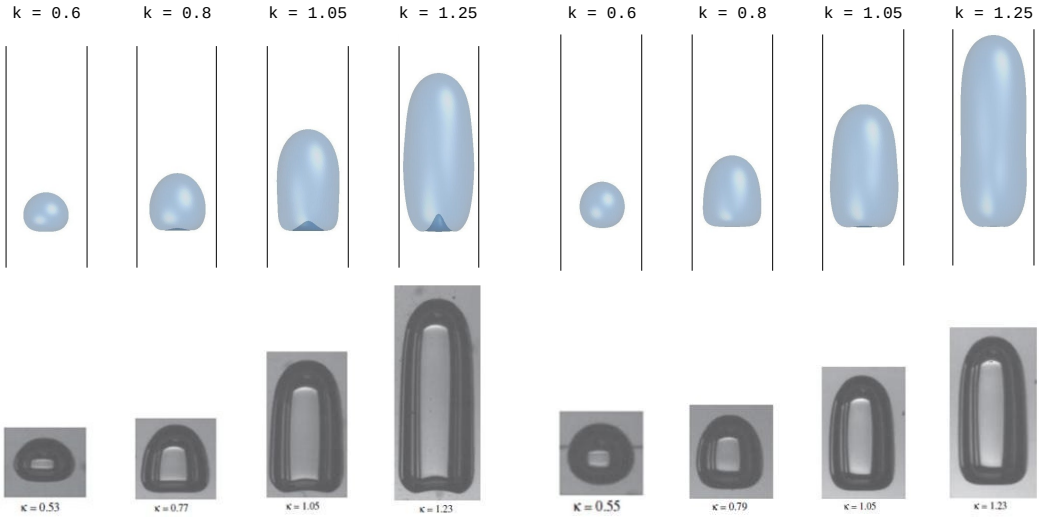

(a) Case *GW2-2* (b) Case *GW3-2*

(c) Case *GW4-2* (d) Case *SO4*

Figure 6.3: Comparison of the final shapes between the LBE simulations and the experimental results by Li *et al.* [99] for four cases (a) *GW2-2*, (b) *GW3-2*, (c) *GW4-2*, and (d) *SO4*. The upper rows present the LBE simulations and the lower rows the experimental results.

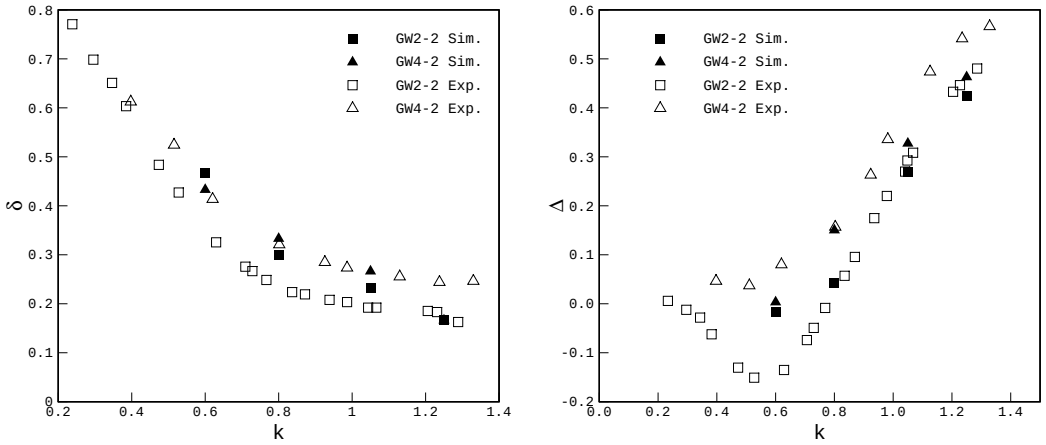

(a) Film thickness δ (b) Deformation parameter Δ

Figure 6.4: Comparison of non-dimensional parameters (a) film thickness δ and (b) deformation parameter Δ between the LBE simulations and the experimental results by Li *et al.* [99] for cases *GW2-2* and *GW4-2*.

where $k \geq 0.8$, deformation is not as consistent. Cases with low Ca such as *GW-1* experience the lowest amount of deformation, since surface tension is higher in those cases. As Ca increases so does the deformation. However, We starts playing an important role. Cases with higher values of We tend to have a flatter bottom surface. In addition, cases where We is the highest have a concave surface at the bottom. This observation is consistent with the results presented by Taha and Cui [29] and Li *et al.* [99]. Taha and Cui attributed the re-entrant cavity to the high value of Ca, whereas Li *et al.* claimed that it was a combination of high values of Ca and We. Furthermore, it is important to emphasize the interesting patterns that can be obtained from the non-dimensional numbers given in the plots. δ is directly proportional to We, which is consistent with the findings by Li *et al.* [99]. However, a consistent pattern for Δ and Ca or We is not perceived from these results. For low k, Δ tends to increase or fluctuate with Ca. In cases shown in Figs. 6.5a, 6.6a, and 6.6b, Δ increases with Ca which implies that the bubble is becoming more elongated along the flow direction. These cases have the largest values of We and Re. On the other hand, for high k the value of Δ tends to decrease or fluctuate with Ca. Cases presented in Figs. 6.7a, 6.7c, and 6.8c, Δ decreases with Ca showing that the bubble is becoming less prolate.

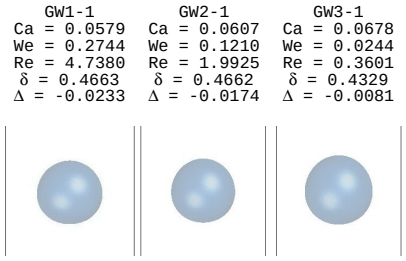

(a) Group *GW-1*

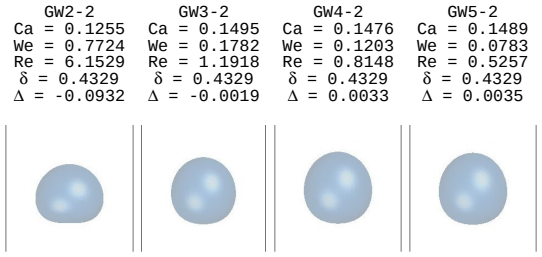

(b) Group *GW-2*

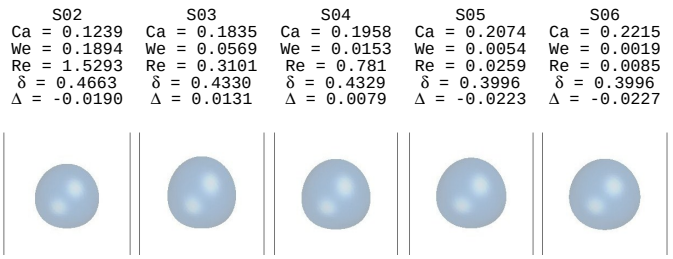

(c) Group *SO*

Figure 6.5: Simulation results for final shape at $T = 10$ and for $k = 0.6$ for all cases organized in three groups. (a) *GW-1*, (b) *GW-2*, and (c) *SO*.

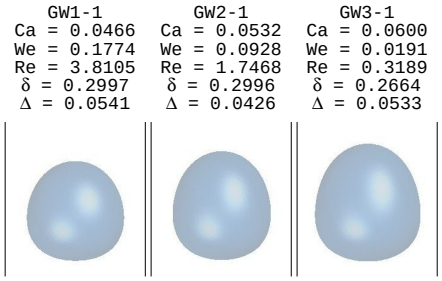

(a) Group *GW-1*

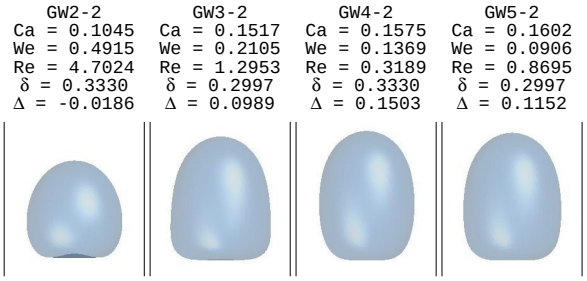

(b) Group *GW-2*

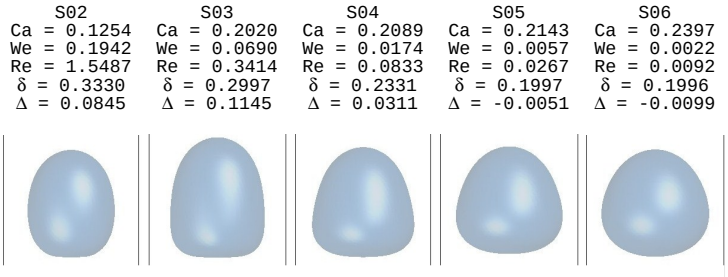

(c) Group *SO*

Figure 6.6: Simulation results for final shape at $T = 10$ and $k = 0.8$ for all cases organized in three groups. (a) *GW-1*, (b) *GW-2*, and (c) *SO*.

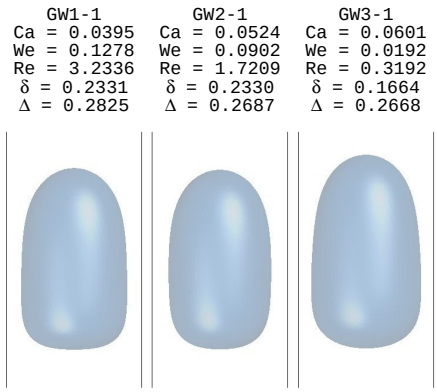

(a) Group *GW-1*

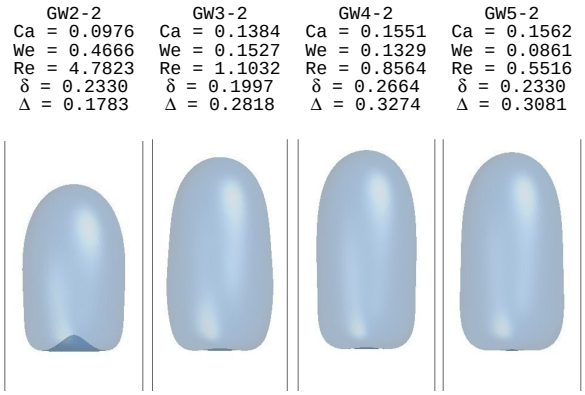

(b) Group *GW-2*

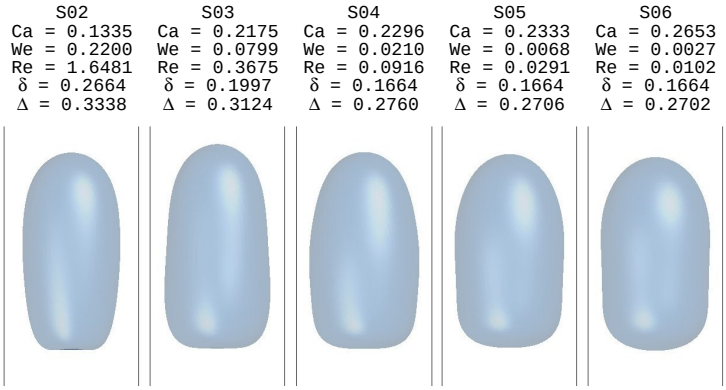

(c) Group *SO*

Figure 6.7: Simulation results for final shape at $T = 10$ and $k = 1.05$ for all cases organized in three groups. (a) *GW-1*, (b) *GW-2*, and (c) *SO*.

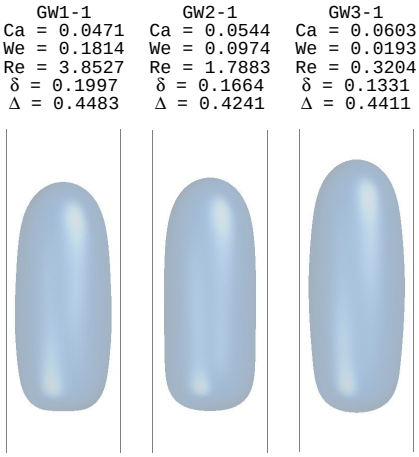

(a) Group *GW-1*

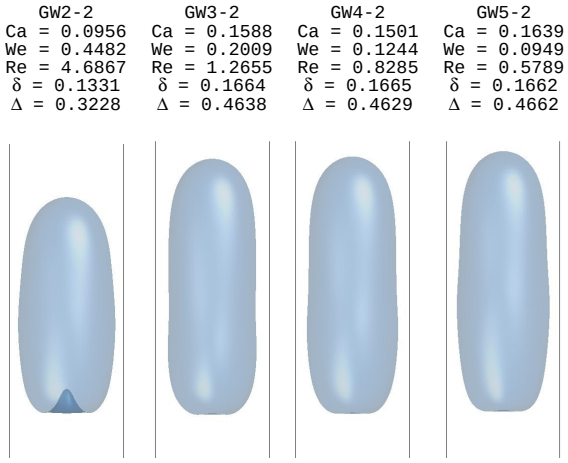

(b) Group *GW-2*

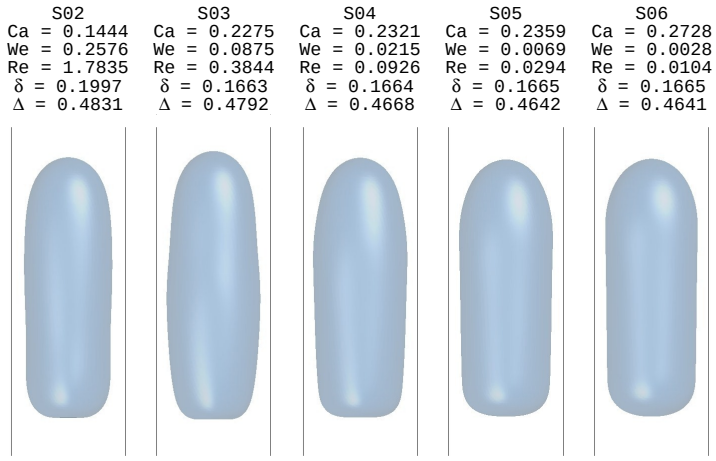

(c) Group *SO*

Figure 6.8: Simulation results for final shape at $T = 10$ and $k = 1.25$ for all cases organized in three groups. (a) *GW-1*, (b) *GW-2*, and (c) *SO*.

These cases correspond to the lowest values of We and Re. Therefore, the behavior of Δ is a combination of k, We, and Re. This is not consistent with the experimental findings by Li *et al.*, which indicates that Δ is inversely proportional solely to We. Their conclusion was reached by comparing only two cases *GW2-2* and *GW4-2*, as presented in the previous section. If only these two cases are considered, the current study predicts increasing Δ with decreasing We as well, as it is presented in Fig. 6.4b.

6.4.1 Final Shape vs. Bo

Bo is an important factor that determines the level of deformation of the bubble. To assess the effect of Bo, a comparison of the final shapes between two cases *GW2* and *GW3* for two different Bo each, labeled as -1 and -2 is performed. The values of Bo for each case are presented in Table 6.1. The comparison is presented in Figs. 6.9a to 6.9b. As can be seen from these plots, deformation for the cases labeled -2 is greater. These cases have higher values of Bo, which indicates that the surface tension is lower and deformation is enhanced. For $k \leq 0.8$ and low Bo bubble tends to remain spherical. However, as Bo increases the bubble tends to become a spherical cap with a flatter bottom surface. In the case of $k \geq 1.05$ and low Bo, the bubble remains elongated with rounded top and bottom surfaces. However, as Bo increases, the radius of curvature at top and the bottom is increased. This effect is more pronounced at the bottom surface, which becomes flatter.

6.4.2 Film Thickness vs. k

A preliminary result for the relationship between δ and k was presented in the previous section as it was compared with the experimental results for two cases. As the value of k increases, so does the volume and the cross-sectional area of the bubble. Therefore, as the bubble rises, it tends to push away liquid from the sides towards the top of the bubble and the corners of the channel, and the value of δ is reduced. Simulation results, which capture this physical relationship between k and δ are presented in Figs. 6.10a to 6.10c. In addition, these plots list the cases in decreasing Ca and increasing We. It could be noticed that the value of δ decreases with Ca and as We

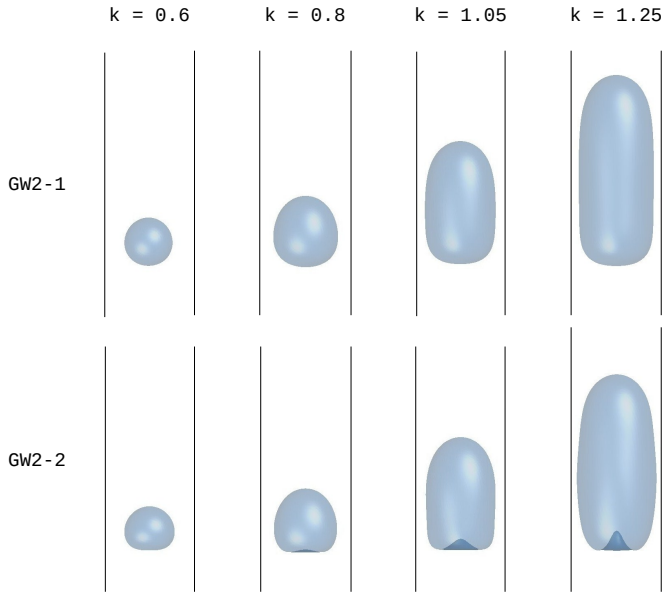

(a) Cases *GW2-1* and *GW2-2*

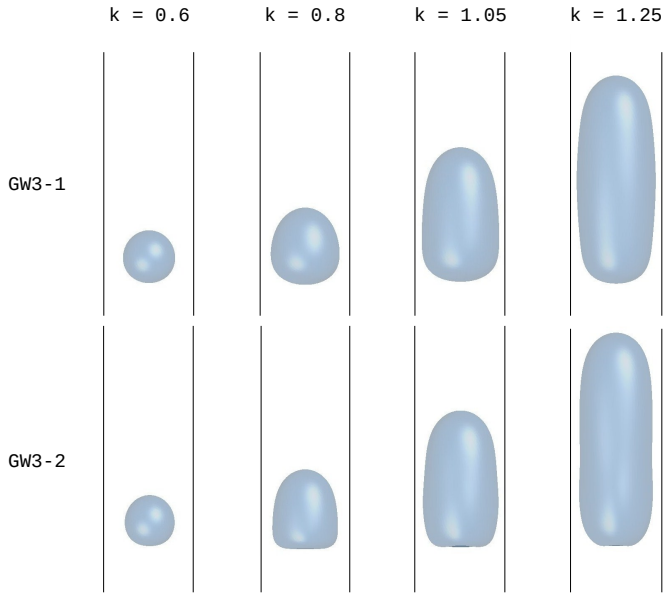

(b) Cases *GW3-1* and *GW3-2*

Figure 6.9: Effect of Bo on final shape at $T = 10$ for cases two cases (a) *GW2* and (b) *GW3*.

goes up. This pattern is consistent with the findings by Li *et al.* [99].

6.4.3 Deformation Parameter vs. k

An initial result for the relationship between Δ and k was presented in the previous section comparing the simulation results with the experimental results for two cases. For these two particular cases, Δ increases with k. Simulation results show that this pattern is consistent for all the cases, as it is shown in Figs. 6.11a to 6.11c. These plots also list the cases in a decreasing Ca and increasing We. It could be noticed that a consistent pattern that relates Δ and Ca or We is not obtained from these plots. Therefore, Δ is a combination of k, Ca and We.

6.5 Streamlines and Vorticity Contours

To facilitate a clear representation of the three-dimensional vectors, two different planes XY and XZ are used to present these streamlines for the all the cases at $k = 1.25$. This value of k was selected since it represents the bubbles that have the highest volume and greatest interaction between the bubble and the walls. Figs. 6.12a to 6.12c show the streamlines in the XY plane at the center of the channel $Z = 0$. Looking closely at these plots, the general silhouette of the streamlines is similar for all the cases. There is a symmetrical recirculation pattern inside of the bubble, which goes over the cross-sectional area of the bubble. Case *SO6* has additional eddies inside of the bubble. This case has the highest level of Ca, therefore the viscous effect will be higher. Furthermore, for all the cases there are no additional eddies at the back of the bubble, since in general the value of the Re is intermediate. The only case, that has a different profile is case *GW2-2*, since this case has a negative curvature at the bottom of the bubble and it also has the highest value of Re.

Figs. 6.13a to 6.18c present the streamlines and the Y-component of vorticity contours in the XZ plane at four different elevations of Y-axis. These elevations were selected by dividing each bubble in 5 equally spaced segments. The placement of these elevations is presented in each of the XY plane plots by four markers label

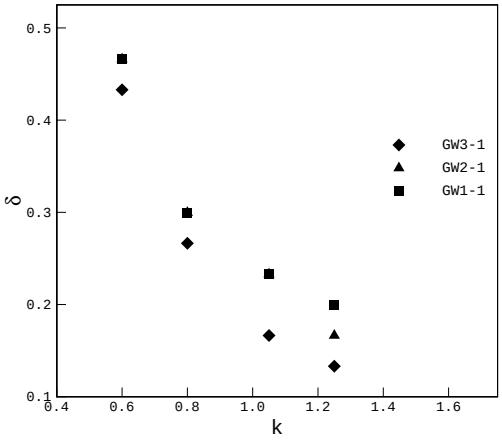

(a) Group *GW-1*

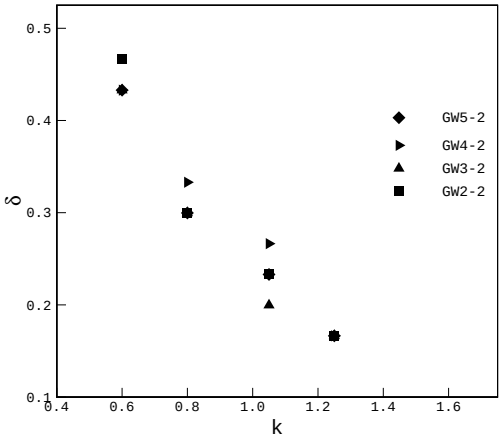

(b) Group *GW-2*

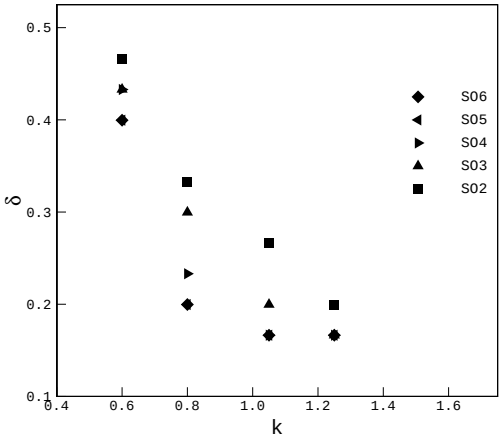

(c) Group *SO*

Figure 6.10: Evolution of film thickness δ as function of k for all cases organized in three groups. (a) *GW-1*, (b) *GW-2*, and (c) *SO*.

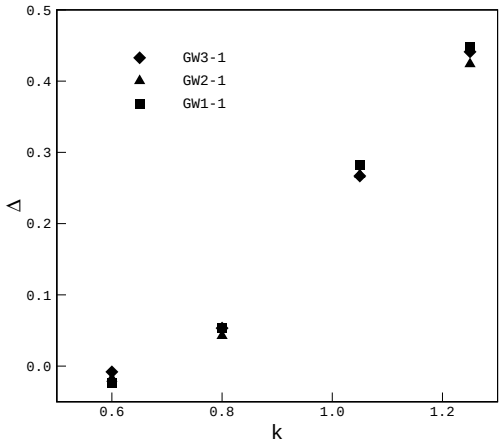

(a) Group *GW-1*

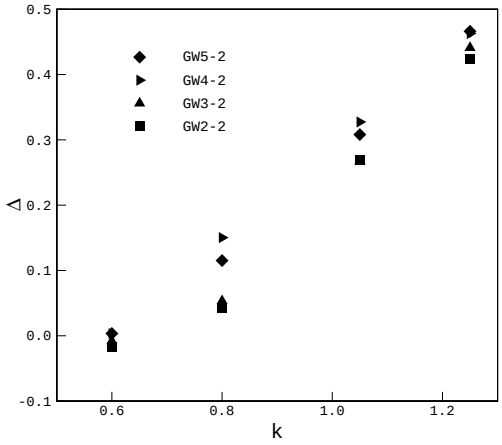

(b) Group *GW-2*

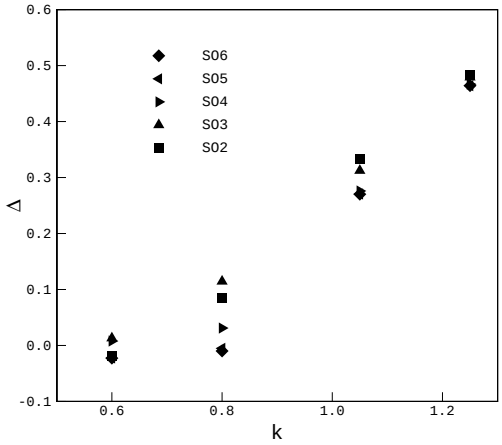

(c) Group *SO*

Figure 6.11: Evolution of deformation parameter Δ as function of k for all cases organized in three groups. (a) *GW-1*, (b) *GW-2*, and (c) *SO*.

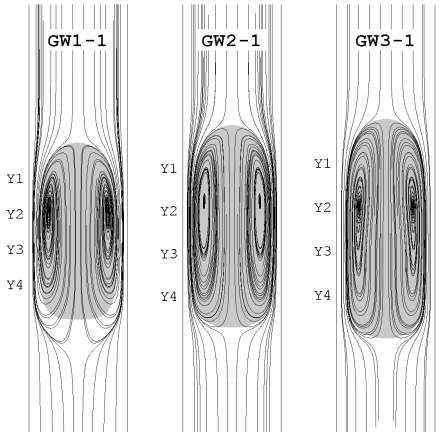

(a) Group *GW-1*

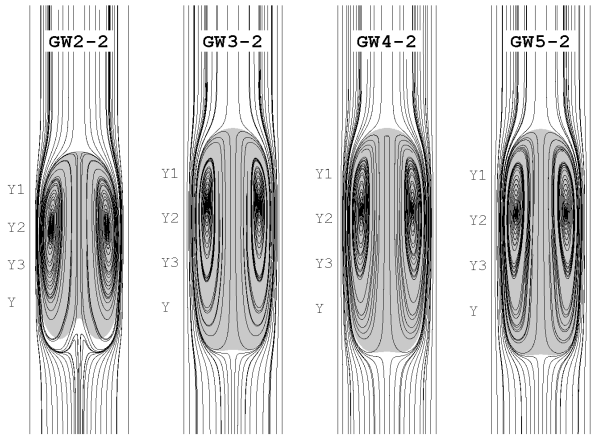

(b) Group *GW-2*

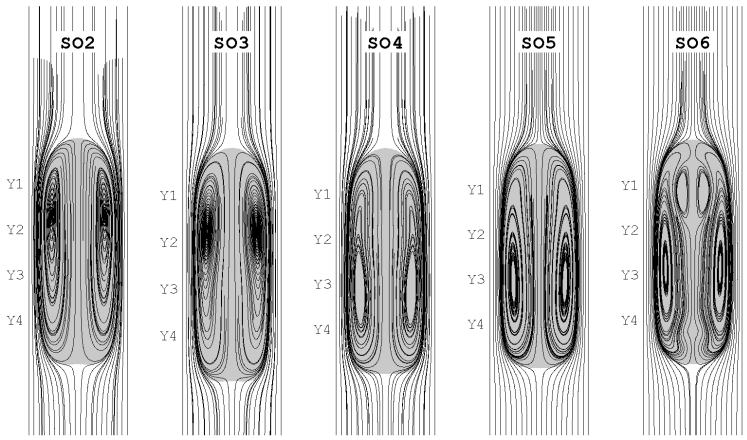

(c) Group *SO*

Figure 6.12: Streamlines in the XY plane at $T = 10$ for all cases organized in three groups. (a) *GW-1*, (b) *GW-2*, and (c) *SO*.

Y1-Y4. Observing in detail these cross-sectional plots, significant patterns can be obtained for the streamlines and the vorticity contours. These patterns will be discussed for each location. For location *Y1*, the streamlines have an asymptotic-like pattern starting at the corners going to center of the channel. In terms of vorticity three different patterns can be observed (along the wall, around the boundary of the bubble, and a combination between them). These patterns can be more easily observed by describing each group individually. For group *GW-1*, the cases with the low Ca, *GW1-1* and *GW2-1* have noticeable vorticity along the wall. However, case *GW3-1* with the highest value of Ca has large vorticity along the wall and the boundary of the bubble. Note that vorticity is non-dimensionalized using $\frac{U_{c2}}{R_c}$, where U_{c2} is the characteristic velocity of the system defined as $U_{c2} = \sqrt{gR_c}$. In general, the value of vorticity is reduced as the Ca increases. As the value of Ca increases, so does the effect of viscosity. This creates a higher resistance to circulation, therefore reducing the value of vorticity. For group *GW-2*, all the cases have vorticity contours along wall and boundary. In addition, the relationship between the vorticity values and the level of Ca is the same as group *GW-1*. In group *SO*, cases with low Ca, *SO2* to *SO4* have noticeable vorticity contours along the wall and the boundary. However, for cases with high Ca the vorticity contour is concentrated only along the wall.

Locations *Y4* have also an asymptotic streamline pattern which is in the opposite direction to that on location *Y1*, from center towards corners of channel. However, case *SO6* has a different pattern in the inner part of the bubble. This corresponds to a non-uniform eddy in the XY plane, see the last plot 6.12c at marker *Y4*. Vorticity contours are concentrated along the wall and the boundary of the bubble. The distribution of these contours depends on the value of Ca in each group. In general, at low Ca contours are along the wall and in the outer perimeter of the bubble edge. However, as Ca increases vorticity contours start to appear in the inside of the bubble and tend to decrease along the wall. The values of vorticity decrease as the value of Ca increases, as it was described in previous location. Another important feature to notice at this location is that the sign of the vorticity is the opposite as location *Y1*. This agrees with the different streamlines direction between two locations, as it was described previously.

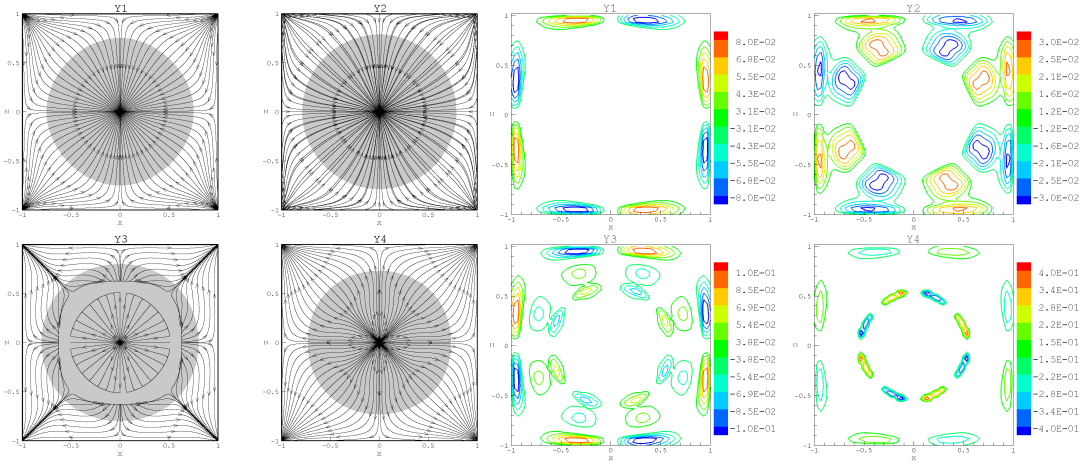

(a) Streamlines for case *GW1-1*

(b) Vorticity contours for case *GW1-1*

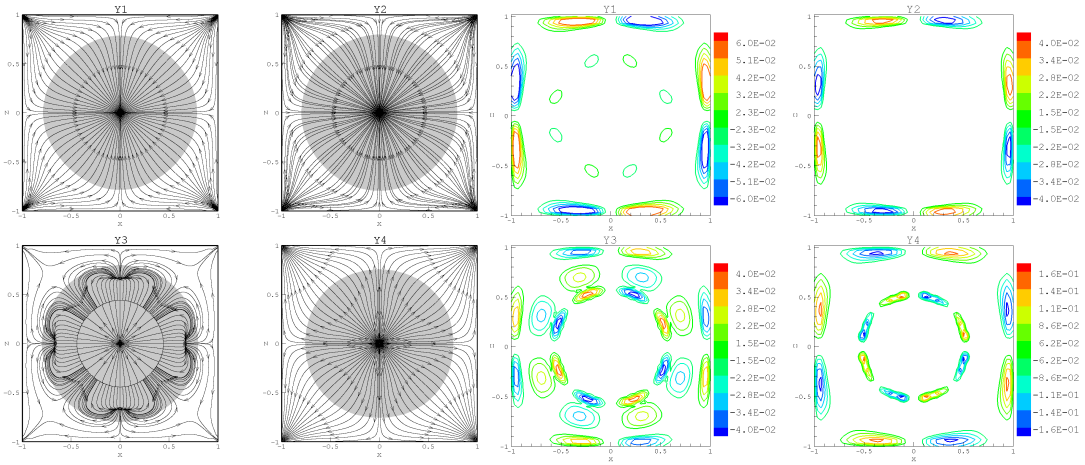

(c) Streamlines for case *GW2-1*

(d) Vorticity contours for case *GW2-1*

Figure 6.13: Streamlines and vorticity contours in the XZ plane at four elevations for cases two cases, the upper row presents case *GW1-1* and the lower row case *GW2-1*.

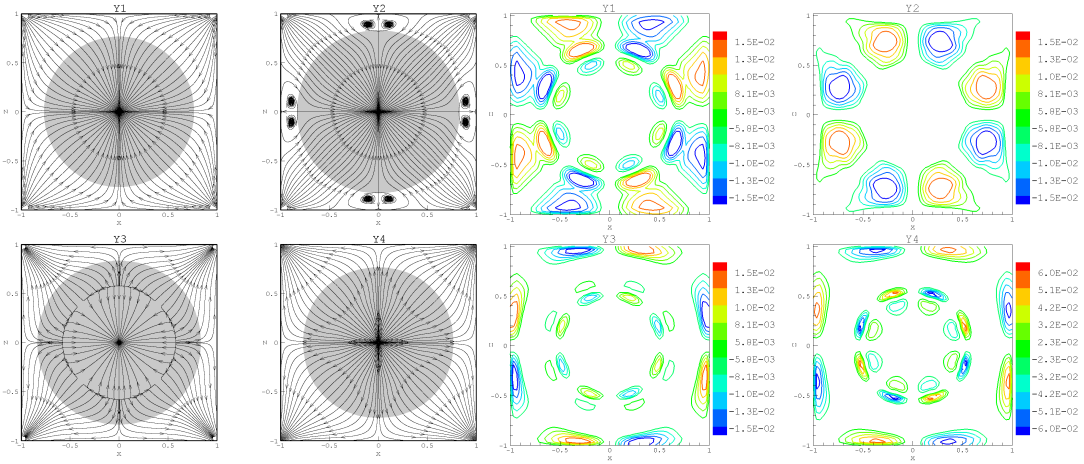

(a) Streamlines for case *GW3-1*

(b) Vorticity contours for case *GW3-1*

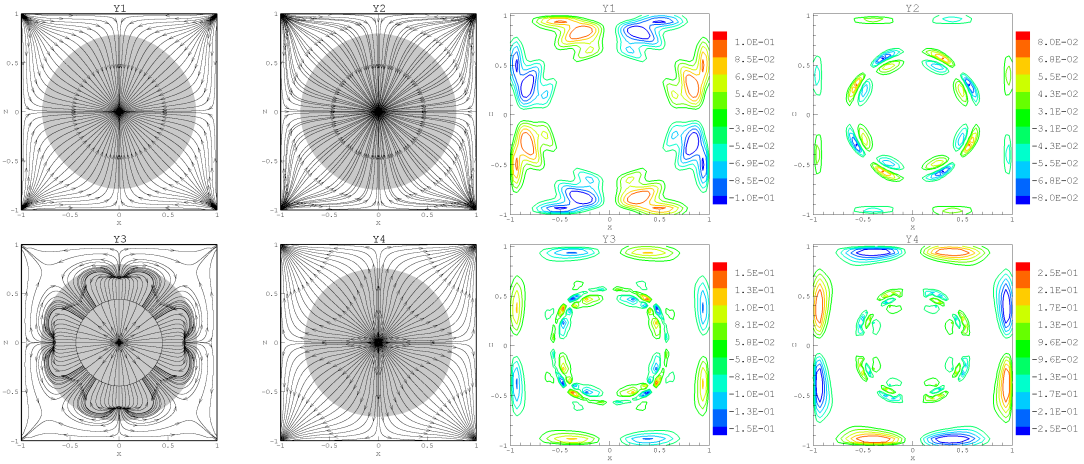

(c) Streamlines for case *GW2-2*

(d) Vorticity contours for case *GW2-2*

Figure 6.14: Streamlines and vorticity contours in the XZ plane at four elevations for cases two cases, the upper row presents case *GW3-1* and the lower row case *GW2-2*.

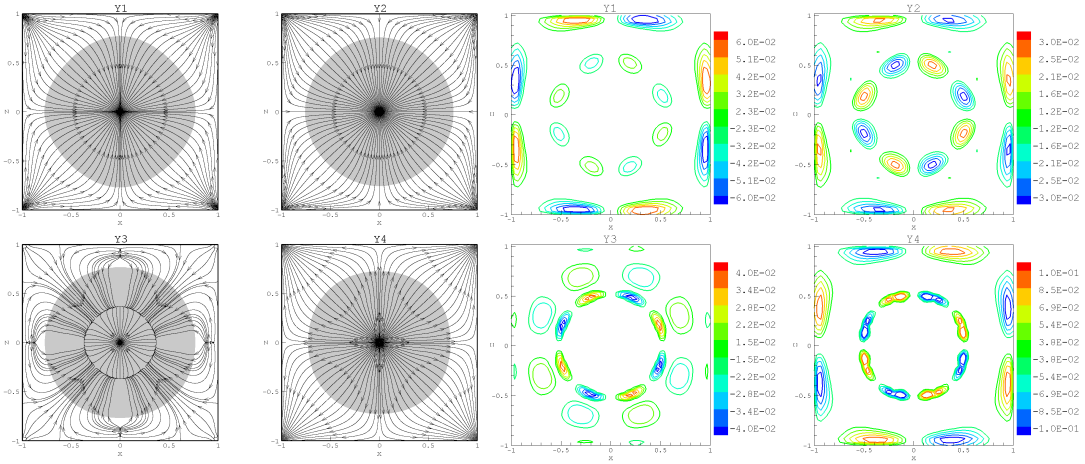

(a) Streamlines for case *GW3-2*

(b) Vorticity contours for case *GW3-2*

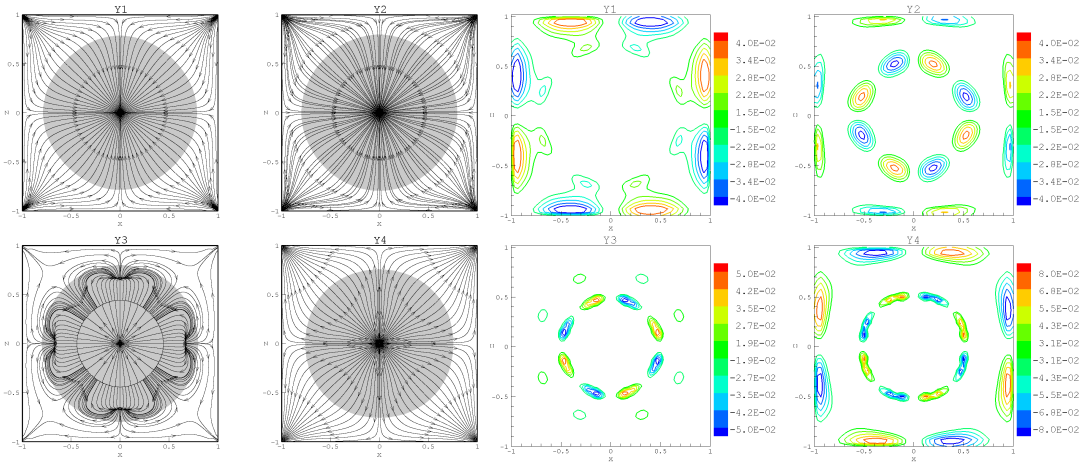

(c) Streamlines for case *GW4-2*

(d) Vorticity contours for case *GW4-2*

Figure 6.15: Streamlines and vorticity contours in the XZ plane at four elevations for cases two cases, the upper row presents case *GW3-2* and the lower row case *GW4-2*.

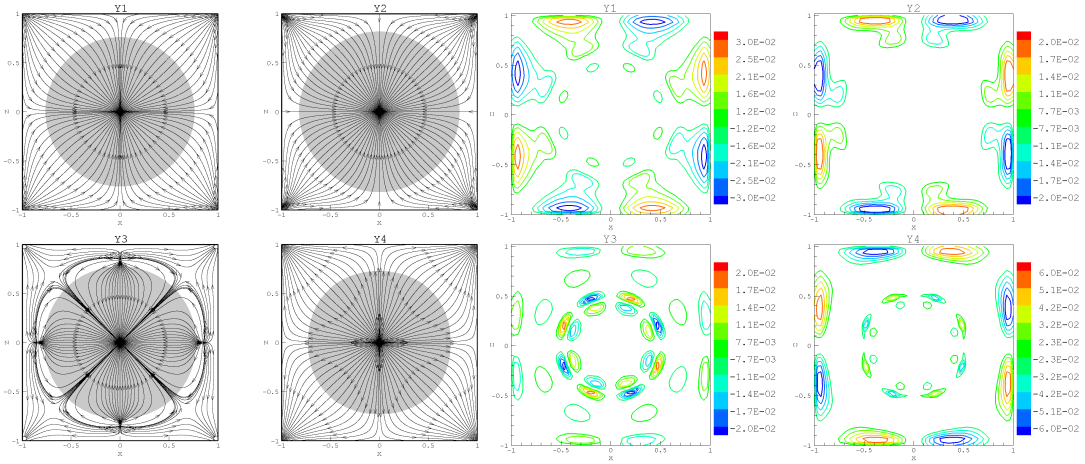

(a) Streamlines for case *GW5-2*

(b) Vorticity contours for case *GW5-2*

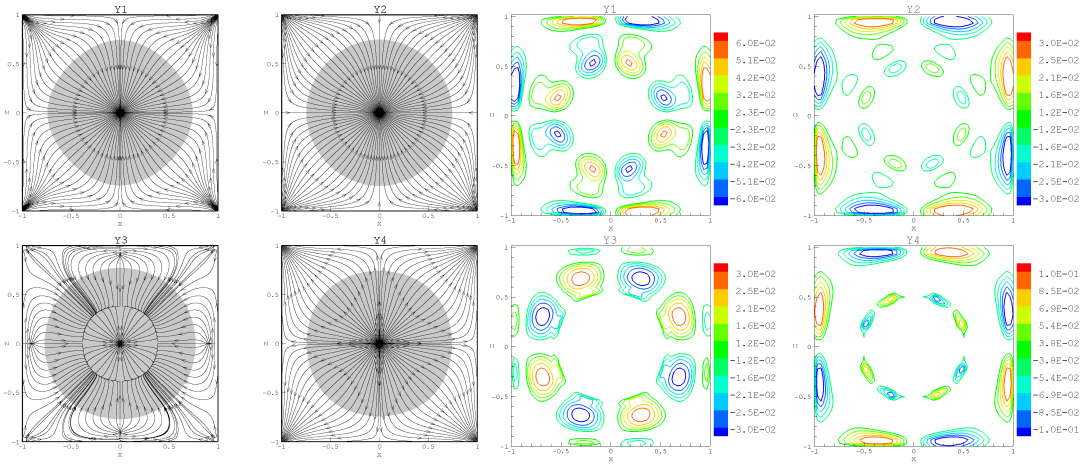

(c) Streamlines for case *SO2*

(d) Vorticity contours for case *SO2*

Figure 6.16: Streamlines and vorticity contours in the XZ plane at four elevations for cases two cases, the upper row presents case *GW5-2* and the lower row case *SO2*.

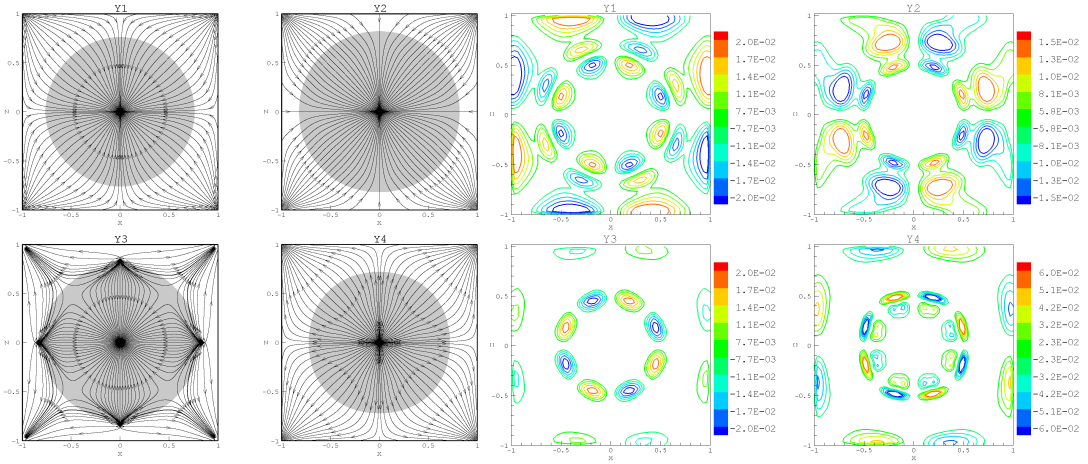

(a) Streamlines for case *SO3*

(b) Vorticity contours for case *SO3*

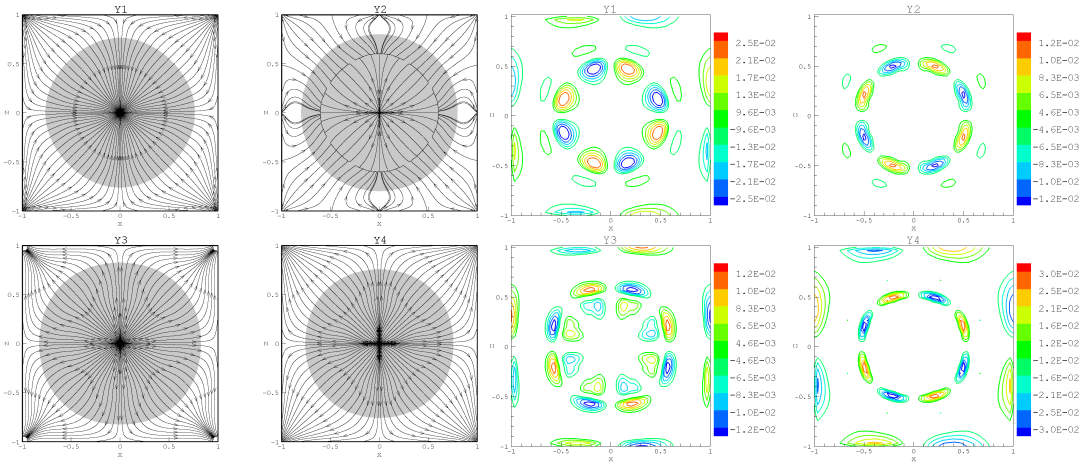

(c) Streamlines for case *SO4*

(d) Vorticity contours for case *SO4*

Figure 6.17: Streamlines and vorticity contours in the XZ plane at four elevations for cases two cases, the upper row presents case *SO3* and the lower row case *SO4*.

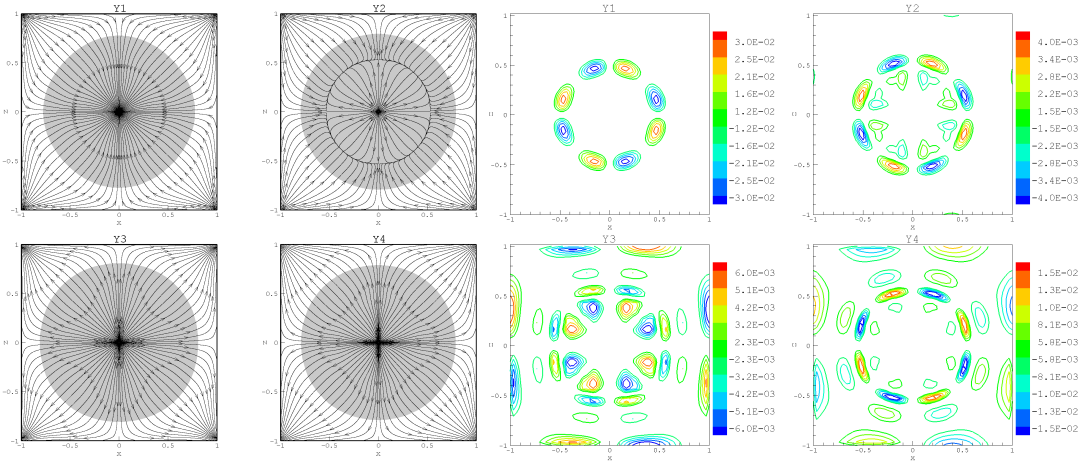

(a) Streamlines for case *SO5*

(b) Vorticity contours for case *SO5*

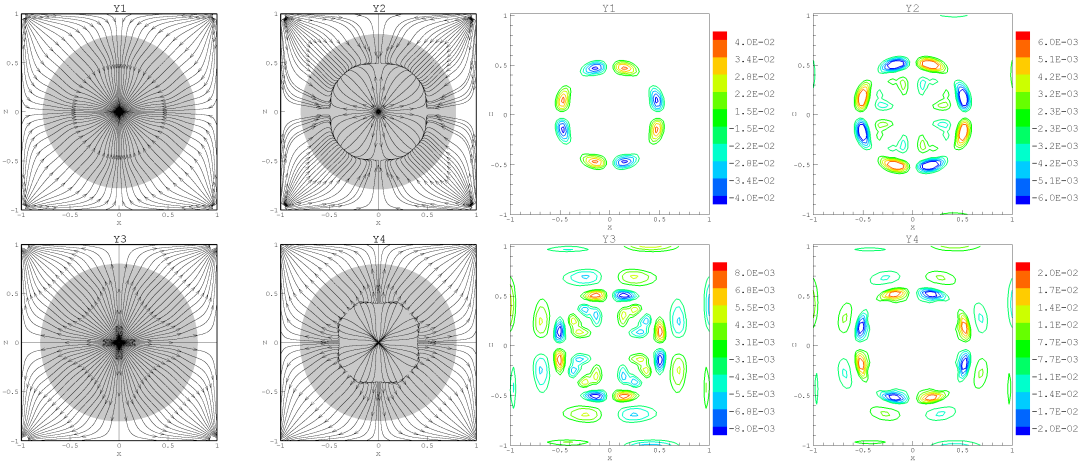

(c) Streamlines for case *SO6*

(d) Vorticity contours for case *SO6*

Figure 6.18: Streamlines and vorticity contours in the XZ plane at four elevations for cases two cases, the upper row presents case *SO5* and the lower row case *SO6*.

The most interesting streamlines and vorticity contours are presented in levels *Y2* and *Y3*. At these locations, bubble tends to push liquid out from the sides and move it towards the corners. In location *Y2*, streamlines are asymptotic like from the corners to the center of the bubble. Different patterns are observed in cases where the value of Ca is higher. For example, *GW3-1* has additional eddies at the center of each side of the bubble. A similar behavior starts to appear in case *SO3*. However, it is not accentuated as much as it is in case *SO4* where the eddies are larger and a different recirculation pattern is found in the center of bubble. In the same manner, cases *SO5* and *SO6* have an additional recirculation pattern concentrated at the middle of the bubble. In general, these cases with different streamline patterns correspond to the vorticity contours which are concentrated at the boundary. Also, for these cases the sign of vorticity changes at this location, which accounts for the additional recirculation patterns. In the location *Y3*, the streamlines have an asymptotic behavior from the center to the corners in cases *SO4* to *SO6*. The remaining cases have different patterns at this location. These patterns include additional recirculation eddies at the center of the bubble. Furthermore, these patterns correspond to vorticity contours that are concentrated along the wall and boundary of bubble. As it was described in previous location, these cases with interesting recirculation patterns also have a change on the sign of vorticity. It can be noticed that the magnitude of vorticity is higher at location *Y4* compared to the other level for all cases, except for *SO5* and *SO6*. This indicates that at the bottom area of the bubble, there is higher circulation, helping the bubble to move upwards. Additionally, there is a relationship between vorticity level and Re, in which the highest value of vorticity level in each case is proportional to the value of Re.

6.6 Pressure Contours

Figs. 6.19a to 6.19l provide three different pressure contours: P_{tot}, P and sum of p_0 and p_c. These figures have been non-dimensionalized using $\frac{P_{btop}-P_i}{1/2\rho_l U_c^2}$, where P_{btop} is the pressure value at highest point in the bubble. Using these contours, note that the main contribution on P_{tot} is given by P. However, the sum of p_0 and p_c

has a subtle effect by creating additional contours in the periphery of the bubble. P is distributed along the channel and the values are inversely proportional to the elevation. The static pressure is reduced as the elevation and gravity is decreased, therefore the difference between $P_{btop} - P$ becomes larger. In general, the highest values of the non-dimensionalized P are located at the bottom surface of the bubble, since it denotes the highest distance within the bubble away from the top. In addition, the range of P becomes smaller in the lower rows, which correspond to the cases with higher values of Mo, indicating that the gravity force is higher, therefore increasing the static pressure. Conversely, contours of p_0 and p_c are concentrated across the interface of the bubble. Evaluating the effect of Bo can be done by comparing these contours between cases *GW2* and *GW3*. Cases *GW2-1* and *GW3-1* have lower Bo, therefore the surface tension is higher enhancing the curvature effect. Also, values of p_0 and p_c tend to increase as the value of Ca decreases, since the surface tension becomes stronger.

6.7 Inclined Channel

Effect of inclination is evaluated at four different angles 30°, 45°, 60°, and 75° for three different cases *SO2*, *SO3*, and *SO4* with $k = 1.25$. The following sections will introduce the effect of inclination in the main physical aspects such as the final shape of a bubble, the film thickness, the deformation parameter, and the velocity. In addition, the streamlines, vorticity, and pressure contours for case *SO3* at each inclination angle will be presented.

6.7.1 Final Shape

Figs. 6.20a to 6.20c show the results in all inclinations for the three cases organized by the increasing value of Ca. Each of the figures includes the final shape of each case as well as the values of non-dimensional numbers in the simulation, such as Ca, We, δ, Δ, and Froude number (Fr) that is defined as $Fr = U_t\sqrt{\frac{\rho}{2R_c g(\rho_l - \rho_g)}}$. As can be seen from these plots, as the inclination angle increases, the surface area at top

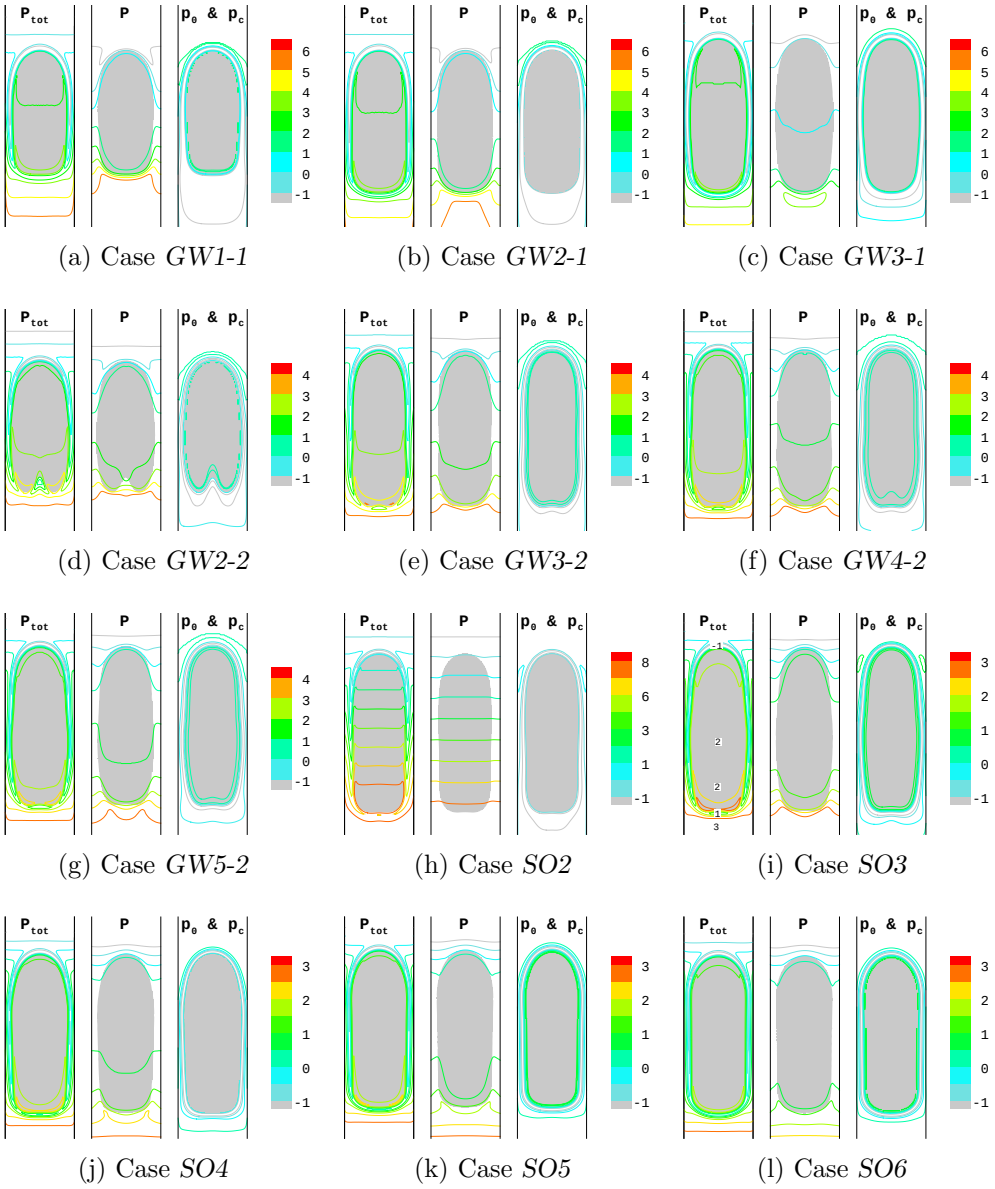

(a) Case *GW1-1* (b) Case *GW2-1* (c) Case *GW3-1*

(d) Case *GW2-2* (e) Case *GW3-2* (f) Case *GW4-2*

(g) Case *GW5-2* (h) Case *SO2* (i) Case *SO3*

(j) Case *SO4* (k) Case *SO5* (l) Case *SO6*

Figure 6.19: Pressure contours: P_{tot} is the total pressure, P is the sum of static and dynamic part, p_0 is the thermodynamic part, and p_c is the curvature part.

of the bubble tends to become flatter and more parallel to the wall. The interesting behavior occurs at the right side of the bubble. For case *SO2*, the bubble tends to be wider at the front of the bubble. On the other hand, in case *SO3*, the rear area is where the wider part of the bubble is located. In case *SO4*, the widest part is located somewhere along the middle of the bubble. Looking closely at the values in these plots, it could be noticed that the values of Ca, Fr, and We have a maximum value which corresponds to an inclination close to 45°. In addition, at constant inclination the value of Fr decreases with Ca. This indicates that as the value of surface tension is reduced, so does the value of the U_t. This is consistent with findings by Zukoski [108].

Film Thickness vs. Inclination

The relationship between δ and inclination for all the cases is presented in Fig. 6.21a. In general, value of δ decreases as the inclination angle is increased. This result is consistent with the observations by DeBisschop *et al.* [112]. The cases in this plot are presented in increasing Ca. Therefore, the value of δ increases with Ca for all the inclinations. Similar conclusion was obtained for the vertical channel, confirming that inclination has no effect on the trend between δ and Ca.

Deformation Parameter vs. Inclination

The effect of inclination on Δ is presented in Fig. 6.21b. In general, the value of Δ increases with inclination. This indicates that the bubble becomes slender and more elongated as the inclination increases. The cases in this plot are listed in increasing value of Ca. Therefore, for these cases, the value of Δ decreases as the value of Ca increases. In the vertical case, it was concluded that Δ is a function of k and Ca. However, by looking closely at the vertical results for these three cases at $k = 1.25$, it can be seen that Δ decreases as Ca increases. Therefore, the inclination has no effect on the relationship between Δ and Ca at a specific value of k.

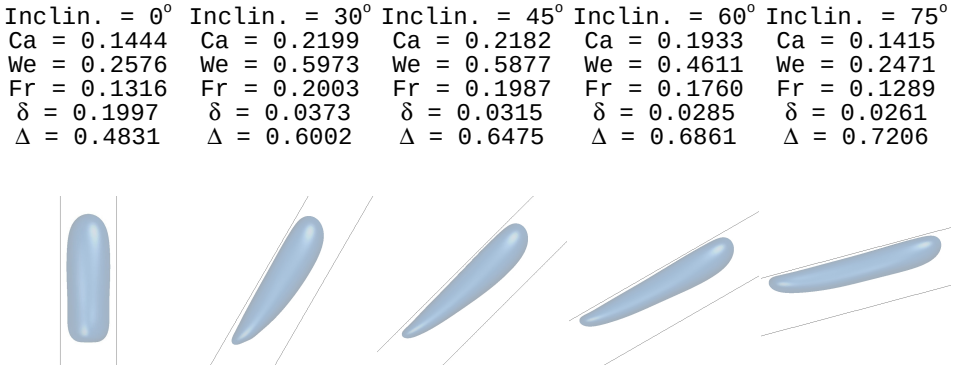

(a) Case *SO2*

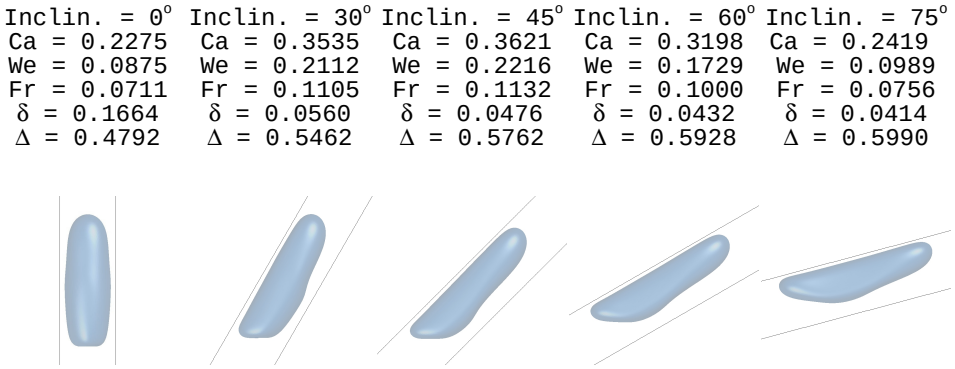

(b) Case *SO3*

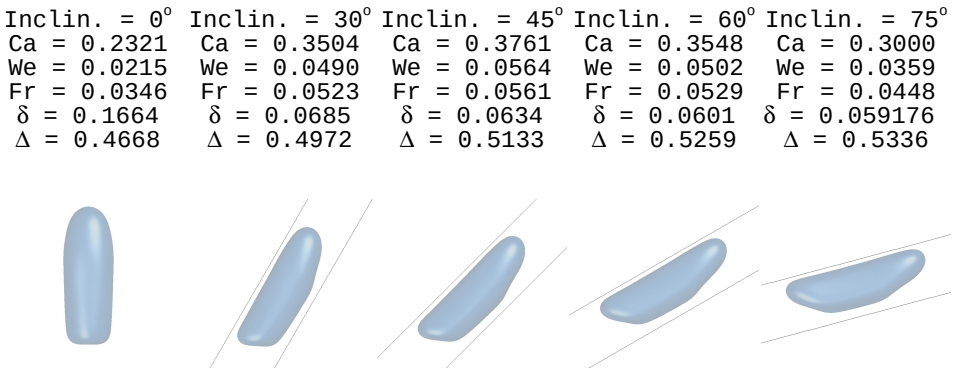

(c) Case *SO4*

Figure 6.20: Final shape at $T = 10$ for different inclination angles for cases *SO2*, *SO3* and *SO4*.

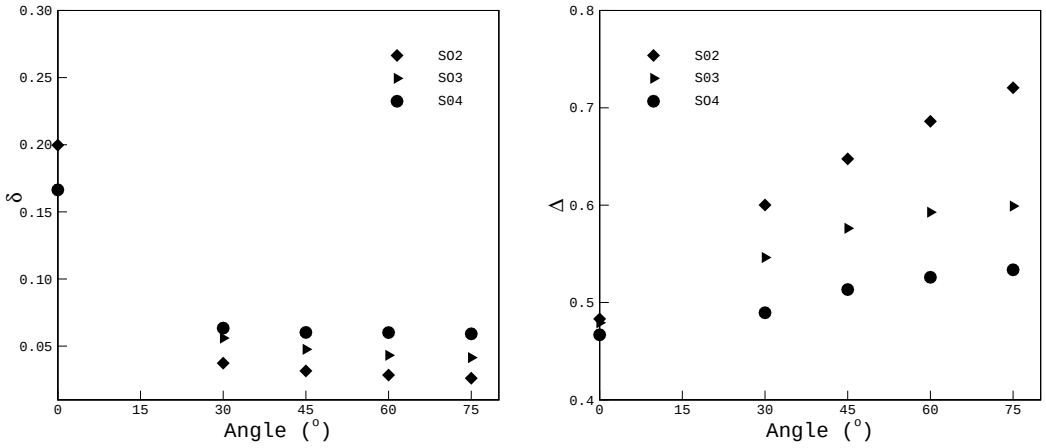

(a) Film thickness δ (b) Deformation parameter Δ

Figure 6.21: Effect of inclination angle on non-dimensional parameters for cases *SO2*, *SO3* and *SO4*.

6.7.2 Velocity vs. Inclination

Evaluation of the velocity at different inclinations is usually performed by comparing the value of Fr. The effect of inclination on Fr is presented in Fig. 6.22. For each case there is a critical angle close to 45° where the value of Fr is the highest. This pattern is consistent with the results presented by [108], [109], and [110]. The cases in this plot are listed in increasing Ca. Using this, note that as the value of Ca decreases, the critical angle value becomes smaller. Therefore, for low Ca cases a maximum velocity is reached at lower inclinations. In addition, the value of Fr is reduced as Ca increases, a result which confirms the experimental findings [108]. Moreover, the critical angle is higher for case *SO4*, which corresponds to the highest value of Mo between the three cases. This confirms the previous experimental findings [110], which indicates that the critical inclination angle is proportional to the value of Mo.

6.7.3 Streamlines and Vorticity Contours

Analysis of streamlines and vorticity contours is performed on case *SO3* for all inclination angles using the same definition of elevations *Y1* to *Y4* as the vertical cases. The streamlines for the XY plane at different inclination angles are given in Fig. 6.23.

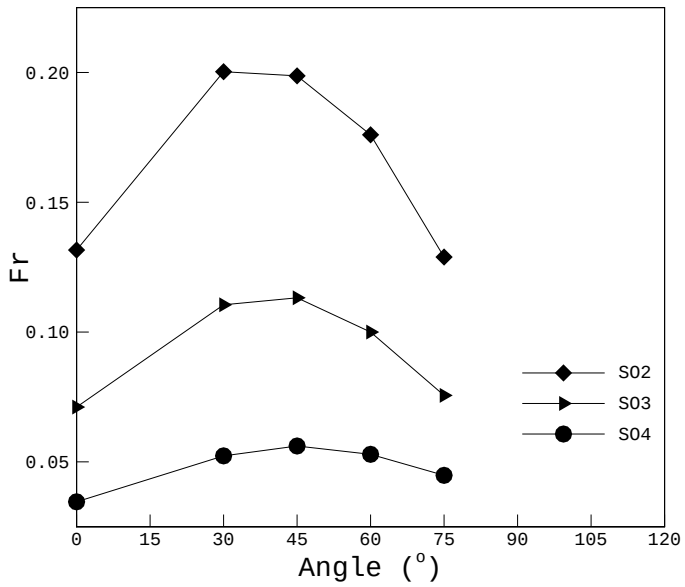

Figure 6.22: Effect of inclination angle on Fr for cases *SO2*, *SO3* and *SO4*.

As can be seen from this plot, the symmetry of the streamlines is lost as the channel is inclined. The streamlines at left side of the bubble tend to go along the wall, and then recirculate towards the right side of the bubble. At 30°, there is an eddy formed at the bottom left side of the bubble. As the inclination is increased, this eddy is reduced in size, until it is completely removed. In addition, there is a recirculation eddy concentrated at the top left side of the bubble. This eddy moves to a higher position in the bubble and becomes smaller as the value of the inclination increases.

The streamlines and vorticity contours in the XZ plane for the different inclinations are presented in Figs. 6.24a to 6.25d. For all the inclinations, the streamlines have a similar asymptotic recirculation pattern at elevations *Y1* and *Y2*. This is a symmetric pattern over Z axis which starts at the right corner towards the center of the bubble. Then, an eddy is generated about the Z axis and parallel wall. Note that the size of these eddies increases with inclination. In terms of vorticity contours for elevations *Y1* and *Y2*, the contours are concentrated at the front and rear of the bubble. In addition, as the inclination is increased there is a development of vorticity along the three walls that are closest to the bubble position. For elevation

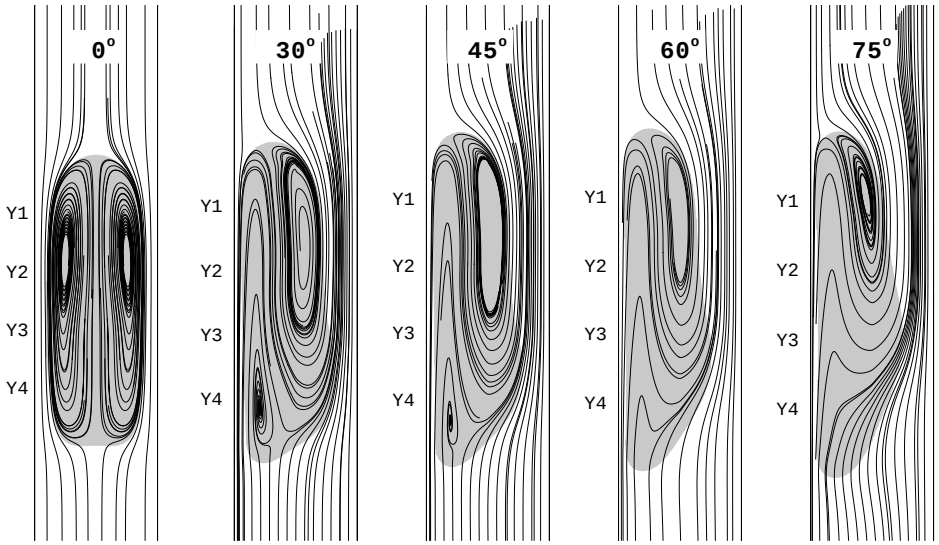

Figure 6.23: Streamlines in the XY plane at $T = 10$ for case *SO3* at inclination angles 30°, 45°, 60°,a 75°.

Y3 the streamlines for inclinations of 30° and 45° have a new recirculation pattern created at the center of the bubble, which corresponds to the change of direction of the vorticity. This type of behavior is similar to the one encountered in the vertical channel. At the same elevation for inclinations 60° and 75° there is no change on the behavior of the streamlines or the vorticity. The streamlines for elevation *Y4* for all the inclinations are very similar. The streamlines start moving from the left side of the bubble towards the right wall, and then returning to the left wall of the channel. In terms of vorticity, it can be seen that for inclinations 30° and 45° the contours are mainly localized at the point where the streamline patterns start at the left side of the bubble. However, for inclinations 60° and 75° there are vorticity contours inside of the bubble and along the three wall closest to the bubble. In general, it could be observed that the values of vorticity are within the same order of magnitude for every inclination at each level.

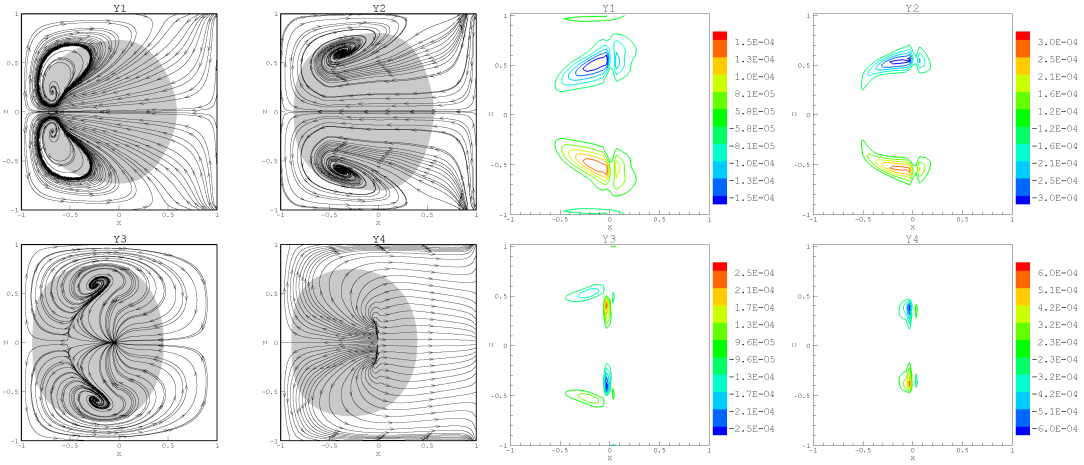

(a) Streamlines at 30°

(b) Vorticity at 30°

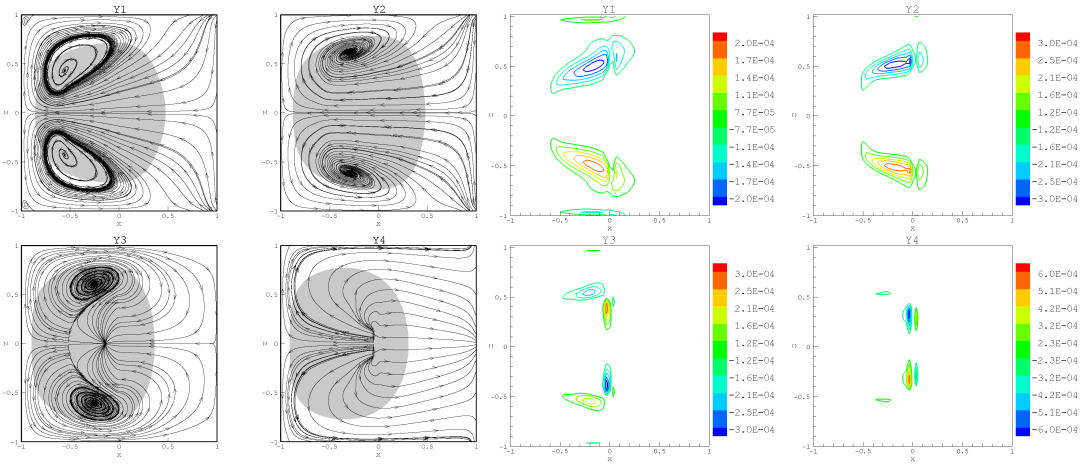

(c) Streamlines at 45°

(d) Vorticity at 45°

Figure 6.24: Streamlines and vorticity contours in the XZ plane at four elevations for case *SO3*, the upper row presents inclination angle 30° and the lower row 45°.

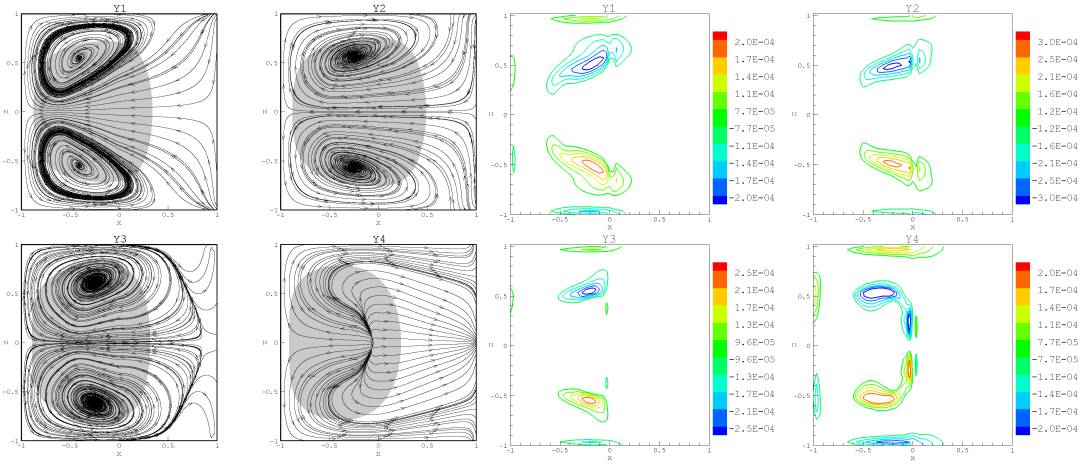

(a) Streamlines at 60° (b) Vorticity at 60°

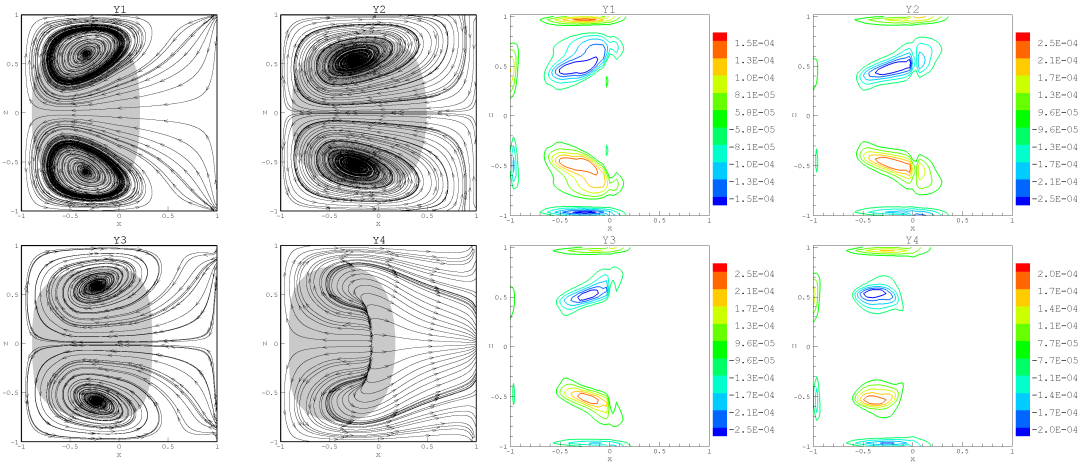

(c) Streamlines at 75° (d) Vorticity at 75°

Figure 6.25: Streamlines and vorticity contours in the XZ plane at four elevations for case *SO3*, the upper row presents inclination angle 60° and the lower row 75°.

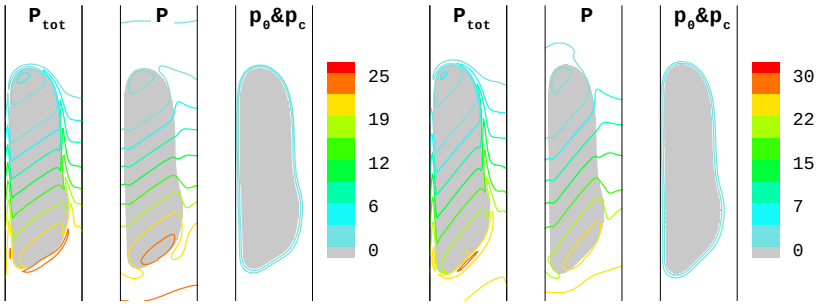

(a) Case *SO3* at 30° (b) Case *SO3* at 45°

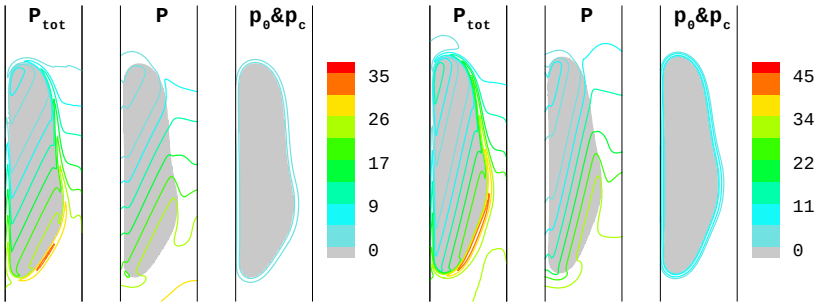

(c) Case *SO3* at 60° (d) Case *SO3* at 75°

Figure 6.26: Pressure contours: P_{tot} is the total pressure, P is the sum of static and dynamic part, p_0 is the thermodynamic part, and p_c is the curvature part.

6.7.4 Pressure Contours

Figs. 6.26a to 6.26d provide the same pressure contours as presented for the vertical cases. Looking closely at these contours the primary mode of pressure is P, and that the effect of p_0 and p_c is mainly concentrated around the bubble. These findings are consistent with the results obtained in the vertical channel cases, therefore inclination does not affect the interaction between the different pressures in the system. However, an interesting feature to notice in regards to the contour lines in P and P_{tot} is that their value range becomes higher as inclination increases. This indicates that the effect of the gravity is lower, therefore reducing the static pressure effect on the system. In addition, the contour lines have a tendency to be perpendicular to the gravity.

In summary, the effect of the wall was evaluated by simulating vertical and inclined square channels. For both cases the simulations were in good agreement with previous

experimental results. This analysis corresponds to the simulation of the segregated area in a microfluidic device, which evaluates the transport of the flow in the main channel. At this point, the task at hand is the simulation of the flow formation, which takes place in the mixing area. This task is introduced in the following section.

Chapter 7

Formation Process in a Microchannel

The last stage in this study is to investigate the bubble and droplet formation process using a T-junction mixing area. This stage is divided into two different parts, one investigates liquid-liquid systems and the other gas-liquid systems. In addition this stage has two geometrical components: the mixing and the segregated area. The segregated area is the same geometry used in the last section, however the main difference is that gravity is not the driving force of the system. Therefore, non-dimensional numbers such as Bo and Mo do not play an important role in the formation or transport processes.

7.1 Background

The use of two immiscible fluids in microchannel geometries has become a growing topic of interest in many industrials applications. Mixing geometry and fluid properties at inlet conditions are the most important criteria to determine the type of flow that will be generated in a microchannel. T-junction is one of the most used mixing geometries to form two-fluid flows in microchannels. Many experimental and numerical studies have been performed to establish a relationship between geometry, mass flow rate and the dynamics of the flow for liquid-liquid and gas-liquid systems.

Experimentally, Xu *et al.* [113] performed a study that adds a capillary tube inside the dispersed fluid flow to increase the shear force and enhance the formation of droplets. This study shows how the flow patterns are strongly dependent on the ratio between fluid velocities and surface contact angle. Later, Nisisako *et al.* [114] performed a study in order to develop a reliable method to control the size and the frequency in the generation of droplets. It was established that controlling the velocity ratio is the key to obtain a consistent method of droplet generation for the given experimental setting. Garstecki *et al.* [22] demonstrated that at a low capillary number, the break-up process, usually referred to as *squeezing* is a balance of the hydrostatic pressure between both fluids. In addition, a scaling law was presented and verified which relates the dimensions of the channels, and flow rate ratio with the final length and diameter of the bubble. Fu *et al.* [115] investigated squeezing, dripping and the transition regimes for gas-liquid systems. These regimes correspond to three different mechanisms: confined break-up, unconfined, and partially confined, respectively. It was noted that in the squeezing regime the bubbles are long slugs, they are dispersed bubbles in the dripping regime, and short slugs in the transition period between the regimes. Size in the transition regime was compared to the model proposed by Christopher *et al.* [116]. Santos and Kawaji [117] performed an experimental and numerical study. Experimentally two different flows were identified, slug and stratified. The slug flow is further classified into three categories, namely snapping, breaking, and jetting, which are presented in a map as function of fluid velocities. $2D$ modeling using Fluent was able to capture the effect of surface tension. In addition, void fraction was calculated and correlated linearly with homogeneous void fraction. Lastly, it was shown that the velocity slip depends on how the dispersed fluid covers the cross-sectional area of the channel and the presence of liquid at the edges. van Steijn *et al.* [118] described the bubble formation using high-resolution, time resolved values using camera, and μ-PIV. Three stages were identified in the formation process of bubble in squeezing regime: filling, squeezing and constriction of the neck followed by break-up. Prediction of bubble length can be estimated without fitted parameter by taking into account the leakage past the bubble. This provides a justification of the confined mechanism. Later, same authors [119] confirmed that the

collapse and pinch-off processes are triggered by a sudden reversed flow of liquid from tip of the gas thread to the neck. Velocity in the corners of the channel is relative to the growing threat itself, which is related to the ratio between the area occupied by the dispersed fluid and the gutters. Velocity increases with the length of the bubble.

Numerically, Qian and Lawal [23] presented a gas-liquid study of Taylor flow using FLUENT. This study evaluated the influence of inlet conditions, the fluid properties, and the wall wetting conditions. It showed that the flow pattern becomes bubblier and the void fraction increases as velocity ratio is decreased. It was also determined that the length of the slugs increases with surface tension, however it was not effected by changing the viscosity or density ratios. In addition, variation of the contact angle changed considerably the shape of the slug making it either concave or convex. Van der Graaf *et al.* [120] performed a liquid-liquid $3D$ study using a Lattice Boltzmann method based on the model introduced by Swift *et al.* [33]. This study investigated the effects of capillary number and contact angle on the volume of the droplets. It was determined that size of bubble decreases as the values of capillary number and contact angle increase. De Menech *et al.* [121] performed a liquid-liquid $3D$ study using phase field model which shows three distinct regimes of droplet formation: squeezing, dripping, and jetting. Each of the regimes has a governing force and a set of parameters which enhances the droplet formation. The transition between one regime to the other is mainly given by the value of a capillary number. Gupta *et al.* [122] performed a liquid-liquid $3D$ study using Lattice Boltzmann for high capillary numbers. This study established a dependence between shear, surface tension, and viscosity ratio on the transition between dripping to jetting regimes.

7.2 Simulation Set Up

Fig. 7.1 provides the schematic diagram of the T-junction mixing geometry used in this study. In the T-junction dispersed fluid (label $_d$) penetrates the main channel which is already filled with continuous fluid (label $_c$) from a vertical direction and a plug starts to grow. A distortion of the dispersed fluid in the downstream direction is created by the pressure gradient and the flow in the main channel. As the dispersed

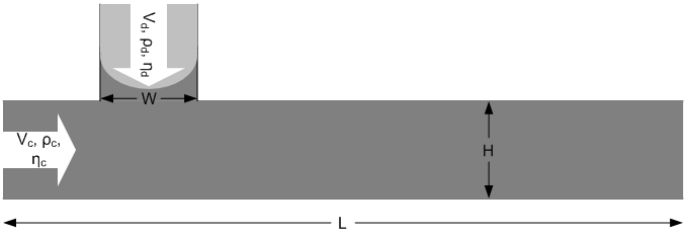

Figure 7.1: $2D$ Schematic diagram of T-junction. v_d and v_c are the mean velocities of the dispersed and continuous liquid respectively. η_d and η_c are the dynamic viscosities and ρ_d and ρ_c are the densities.

fluid stream starts to get reduced and a neck is created and finally broken, and a plug is created. This plug continues downstream in the main channel and the process starts all over again.

7.3 Validation Test

For a $2D$ geometry, the main dimensions in both geometries are H, W, and L. In order to determine the relationship between these quantities a series of $2D$ runs are performed using T-junction. In addition, simulations were carried out to determine the effect of other important numerical parameters such as density $\rho_{ratio} = \rho_d/\rho_c$ and contact angle θ_{eq} in the formation process to be consistent with experimental results. Simulations were performed in a gas-liquid system with constant viscosity ratio $\lambda = \eta_d/\eta_c = 1.0$ and variable Q which is the volumetric flow ratio defined as $Q = Q_d/Q_c$. Evaluation of each parameter is performed by comparing the final shape of the bubble and the evolution of two important values W_m and L_{bu}. W_m is the maximum width that the gas stream will reach at the tee section and L_{bu} is the length of gas stream measure from the tee, before the bubble detaches. Graphical representation of these values is presented in Fig. 7.2. All the results in this section are presented using non-dimensional time defined as $T = t/t_{n3}$, where $t_{n3} = H/v_d$.

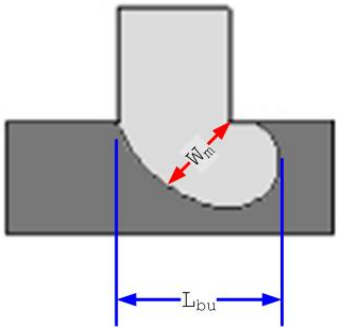

Figure 7.2: Graphical representation of W_m and L_{bu}.

7.3.1 Grid Resolution

A resolution analysis was performed by varying the numbers of grid points in dimension H while maintaining the following relations $W = H$ and $L = 15H$. The numbers of grid points used in this analysis were 20, 30, 40, and 60. Although all grid resolutions are able to capture the break-up process, there is a significant difference between the final lengths of the bubble, as shown in Fig. 7.3. Comparing the finest and coarsest grid cases, the difference between final values of the length of the slug is around 16%. Fig. 7.4a shows the effect of grid resolution on the evolution of L_{bu}, which indicates the location where break-up takes place. In general, the value of L_{bu} tends to increase with resolution and its evolution tends to collapse to a single line if resolution is significantly higher. Another important feature to analyze is the value of W_m, which shows the growth of the gas stream around the tee. Fig. 7.4b shows that for all the cases, the evolution for W_m has the same behavior representing the three stages of formation: expansion, collapse, and break-up. In the expansion stage, the value of W_m increases until it reaches a maximum value where the collapse stage starts. Once the value of W_m reaches its minimum the break-up takes place. In general, the gas stream enters the main channel sooner for high resolution cases, therefore expansion of W_m takes place faster. The maximum value of W_m reached for all the cases is about the same, and the evolution for 40 and 60 are very close to each other. Considering the results provided by this analysis, it is determined that using

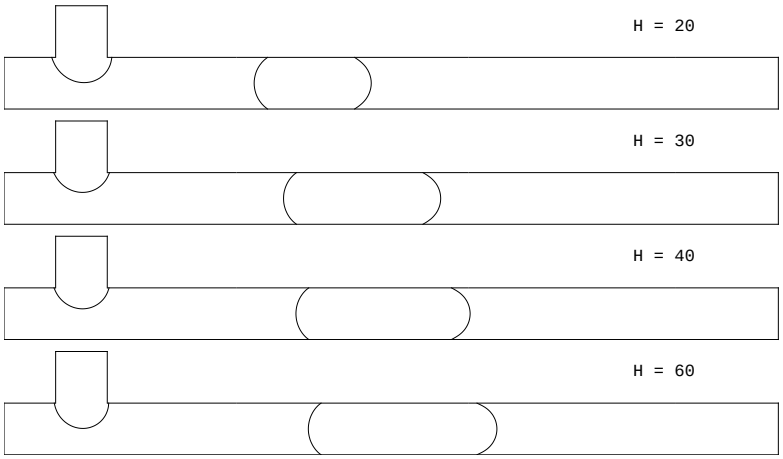

Figure 7.3: Effect of grid resolution on terminal shape for $Ca = 0.005$, $Q = 0.8$, and $\lambda = 1$, $\theta_{eq} = 30°$ at $T = 12$.

the intermediate grid in this study, corresponding to $H = 40$ grid points will provide reasonable accuracy and avoid high computational cost.

7.3.2 Domain Size

Simulations are performed in a semi-confined domain, ergo wall boundary conditions are no-slip in all directions and bounce-back conditions are applied for both g_α and h_α. All open conditions are treated with equilibrium boundary condition for g_α and h_α. Density and velocity are fixed at the entrance and gradient free at the exit. It is important to understand what effect the location of the exit has on the formation of the bubble. Therefore, analysis of the domain size is performed by changing the value of the L as function of H. The different cases tested were $10H$, $15H$, $20H$, and $30H$. Fig. 7.5 shows that final shape of the slug for all the domain sizes is quite similar, and the length of slug is different by less than 7%. The main difference is the location of the slug, which is slightly closer to the tee for largest domain size. Fig. 7.6a shows that final value of L_{bu} is about the same for all the cases. In addition, Fig. 7.6b shows evolution of W_m is not significantly effected by the domain sizes. The maximum value of W_m is almost the same for all the cases and it is reached at

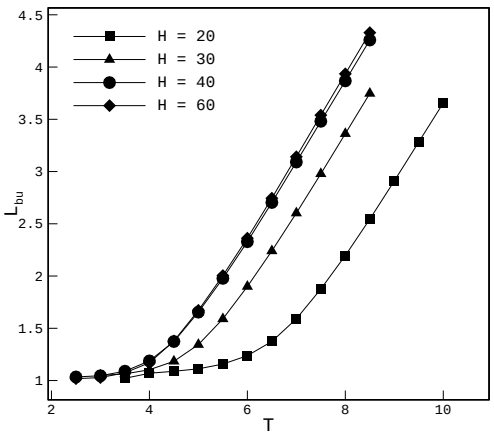

(a) Effect of grid resolution on the evolution L_{bu}.

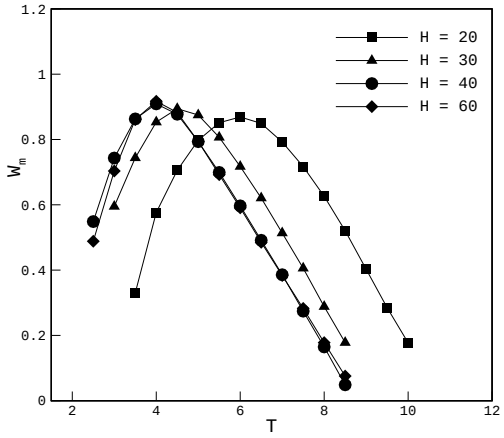

(b) Effect of grid resolution on the evolution W_m.

Figure 7.4: Effect of grid resolution on the evolution of L_{bu} and W_m for $Ca = 0.005$, $Q = 0.8$, $\lambda = 1$, and $\theta_{eq} = 30°$ at $T = 12$.

comparable times. Using these results, it is determined that using an intermediate domain size corresponding to $L = 20H$ would provide reasonable accuracy and avoid high computational cost. In addition, using this domain size would allow capturing significant topological changes that may take place further along the main channel.

7.3.3 Density Ratio

Liquid-liquid systems have density ratio magnitude in the order of unity. However, gas-liquid systems can reach low density ratios in the order of 10^{-3}. Previous numerical studies assume that both fluids (gas and liquid) have the same density, arguing that at microscale the buoyancy has little to no effect on the evolution of the flow. However, a numerical comparison has not been yet presented verifying this assumption. In order to evaluate the effect of density ratio, four ratios are considered: 1, 0.1, 0.01, and 0.001 in two cases with $Ca = 0.005$ with $Q = 0.8$ and $Q = 5.0$. This value of Ca corresponds to the squeezing regime, where surface tension is the dominant force and the size of the bubble is proportional to the value of Q. Decreasing the value of Q makes flow bubblier and increases the frequency of formation. Figs. 7.7a and 7.7b show the final shape of a bubble forming at $Q = 0.8$ and $Q = 5.0$ respectively. For

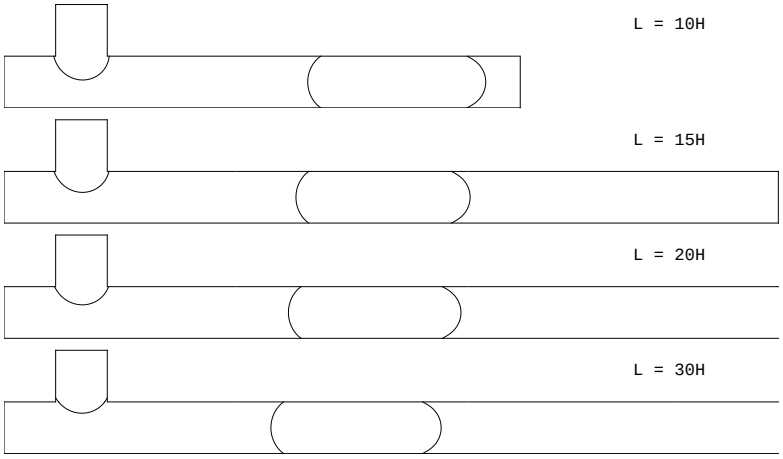

Figure 7.5: Effect of domain size on terminal shape for $Ca = 0.005$, $Q = 0.8$, $\lambda = 1$, and $\theta_{eq} = 30^\circ$ at $T = 12$.

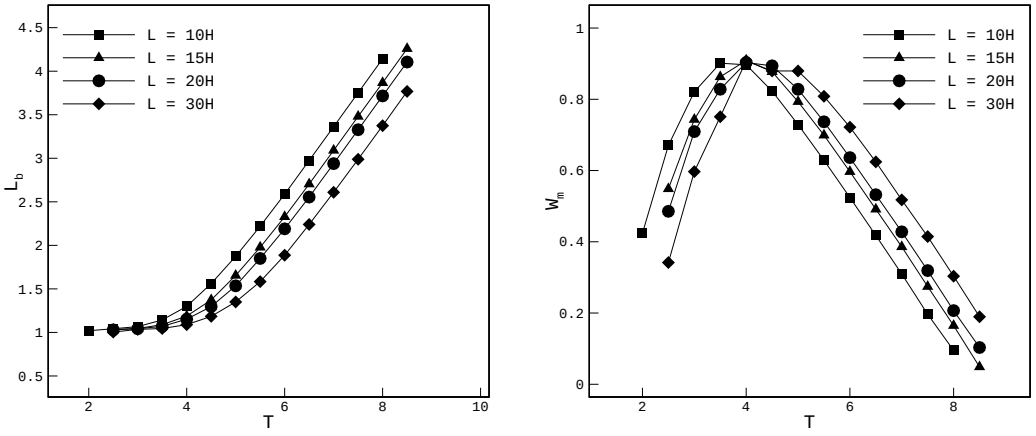

(a) Effect of domain size on the evolution L_{bu}. (b) Effect domain size on the evolution W_m.

Figure 7.6: Effect of domain size on the evolution of L_{bu} and W_m for $Ca = 0.005$, $Q = 0.8$, $\lambda = 1$, and $\theta_{eq} = 30^\circ$ at $T = 12$.

the case with $Q = 0.8$, it is noted that the break-up process is enabled when the density ratio is the smallest. However, for the case with $Q = 5.0$ the final shapes at the front and middle of the bubble are almost overlapping each other. From these plots it can be seen that the main difference in both cases is concentrated in the area close to the tee. It is believed that the source of the dissimilarity is due to the inertia effect on the system. Using a non-dimensional number for inertia $I = Re/Ca$, the inertia of the continuous fluid for the case with $Q = 0.8$ is more than 6 times higher than for the case $Q = 5$. Wagner *et al.* [123] showed that the increase in inertia produces larger deformation, which in this case leads to bubble break-up. Therefore, comparing the given cases, inertia plays a more important role as the value of Q is reduced. In addition, Wagner *et al.* presented evidence that suggests that inertia is a necessary component for the loss of stability in a $2D$ break-up. The concept of critical inertia I_c is introduced, where a singularity is observed in the deformation curve creating a steeper slope. This indicates that there is a sudden transition when $I = I_c$, and the deformation mode would be different when $I < I_c$ compared to $I > I_c$. Furthermore, the authors question whether simulations performed in $3D$ would also undergo the sudden transition that was seen in $2D$. In conclusion, setting the density of the fluids to be the same when simulating a gas-liquid system is not viable, an acceptable assumption unless the ratio of inertia is acceptably low. Unfortunately, using a low value of density ratio may create numerical instability in the simulation. Therefore, in order to reach a compromise between an accurate solution to physical cases and a numerical stability, this study will use a density ratio of 0.01 and 0.001 when possible.

7.3.4 Contact Angle

The effect of contact angle is evaluated on a gas-liquid system by comparing five different cases $\theta_{eq} = 30°$, $\theta_{eq} = 60°$, $\theta_{eq} = 90°$, $\theta_{eq} = 120°$, and $\theta_{eq} = 150°$ for $Ca = 0.005$, $Q = 0.8$, $\lambda = 1$, and $\rho_{ratio} = 0.01$. Fig. 7.8 shows the final shapes for the gas-liquid system, where the contact angle is measured in the continuous fluid. As the contact angle increases, the surface becomes more non-wetting; ergo the surface

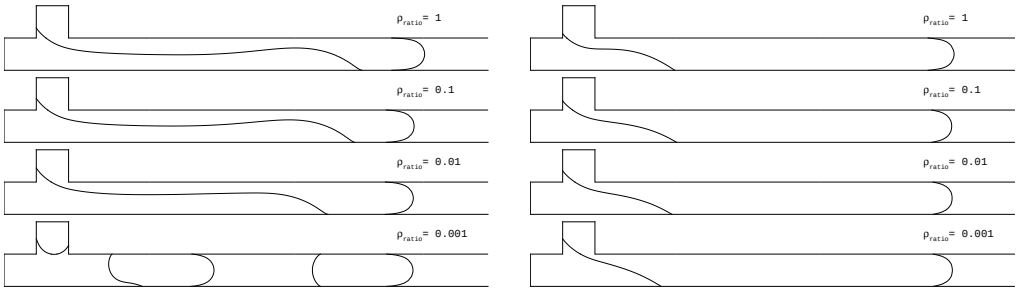

(a) Effect of density ratio on terminal shape for $Ca = 0.005$, $Q = 0.8$, $\lambda = 1$, and $\theta_{eq} = 30°$ at $T = 18$

(b) Effect of density ratio on terminal shape for $Ca = 0.005$, $Q = 5.0$, $\lambda = 1$, and $\theta_{eq} = 30°$ at $T = 18$

Figure 7.7: Effect of density ratio on terminal shape.

attracts the gas and rejects the liquid. When the contact angle is small, the shape of the slug becomes convex; however for high contact angle it tends to become concave.

It is important to note that the effect of θ_{eq} is significant regardless of the fluids in the system or the value of Ca. Figs. 7.9 and 7.10 present the formation process of bubble and droplets respectively at three different Ca and three θ_{eq}. In the gas-liquid system it is noted that for all the values of Ca, as the value of θ_{eq} increases the formation is hindered, since the gas tends to be more attached to the wall surface. On the other hand, liquid-liquid systems exhibit the opposite behavior, since in this system the contact angle is measured in the dispersed fluid. As can be seen in Fig. 7.10 decreasing θ_{eq} hinders droplet formation regardless of the value of Ca. For the cases with a low Ca, note that as θ_{eq} is reduced, the plug formed by the dispersed fluid is reduced in size and is drawn and stretched more towards the upper surface of the channel. This conclusion was also reached by Van der Graaf *et al.* [120]. On the other hand, droplets do not pinch-off when the value of θ_{eq} decreases for cases of larger values of Ca. In general, experimental and numerical studies assume that the surface is almost completely wetting. Therefore, simulations in this study are carried out using a value that would represent physical wetting, $\theta_{eq} = 30°$ and $\theta_{eq} = 150°$ for gas-liquid and liquid-liquid systems respectively.

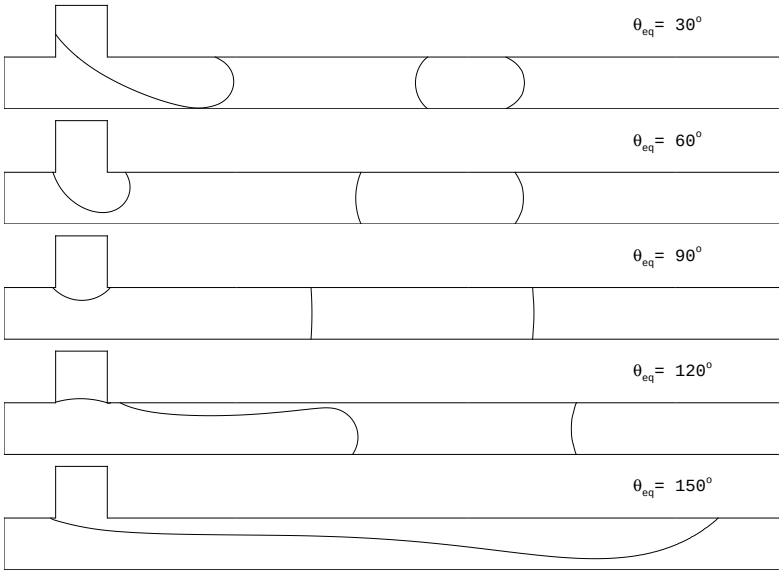

Figure 7.8: Effect of contact angle θ_{eq} on bubble terminal shape for $\theta_{eq} = 30°$, $\theta_{eq} = 60°$, $\theta_{eq} = 90°$, $\theta_{eq} = 120°$, and $\theta_{eq} = 150°$ with $Ca = 0.005$, $Q = 0.8$, $\rho_{ratio} = 0.001$, and $\lambda = 1$ at $T = 15$.

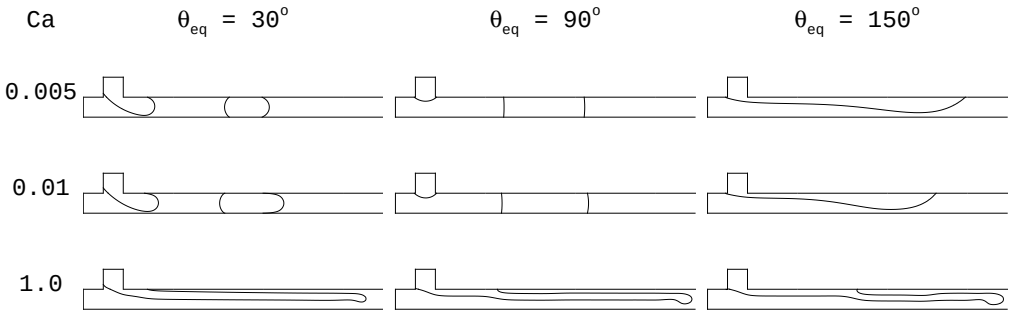

Figure 7.9: Effect of contact angle θ_{eq} on bubble terminal shape for $\theta_{eq} = 30°$, $\theta_{eq} = 90°$ and $\theta_{eq} = 150°$ with $Ca = 0.005$, $Ca = 0.01$, and $Ca = 1$. $Q = 0.8$, $\rho_{ratio} = 0.001$, and $\lambda = 1$ at $T = 15$.

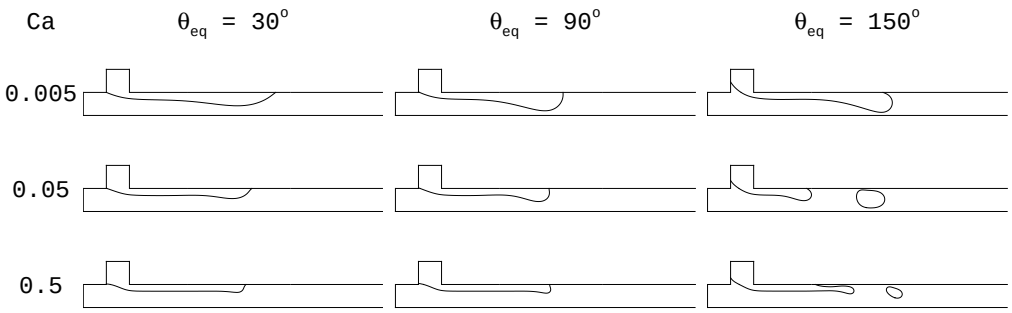

Figure 7.10: Effect of contact angle θ_{eq} on droplet terminal shape for $\theta_{eq} = 30°$, $\theta_{eq} = 90°$ and $\theta_{eq} = 150°$ with $Ca = 0.005$, $Ca = 0.05$, and $Ca = 0.5$. $Q = 0.25$ and $\lambda = 1$ at $T = 12$.

7.4 Comparison to Experimental Results

Capabilities of the numerical method used in this study are assessed by simulating a benchmark case selected from the experimental study by van Steijn *et al.* [118]. The working fluids are ethanol and air, and the surface of the channel is considered fully wetting. The square channel size is $H = 800\mu m$ and $L \approx 200H$. Comparison between the experimental and simulation results is performed using the silhouette of the bubble at different stages of the formation process, the evolution of W_m, and the final shape and dimensions of the bubble.

7.4.1 Formation Process

Experimental results are presented using the time for a formation cycle, which corresponds to $T_c = 170ms$. In order to provide a reasonable comparison, the numerical results will be presented using same notation, where numerical non-dimensional time formation cycle corresponds to $T_c = 11$. Fig. 7.11 presents the formation process of the bubble at four different times. In general, it can be noted that the numerical results for the evolution of the gas at each time are in good agreement with the experimental results. To provide a more complete comparison, Fig. 7.12 introduces the in-plane velocity field. Time $T/T_c = 0.03$ and $T/T_c = 0.3$ correspond to the filling

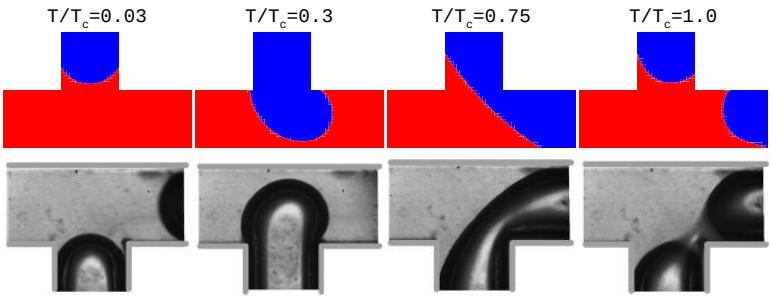

Figure 7.11: Comparison of shape in the formation process for ethanol and air and $Q = 1.5$. Top row presents the simulation results and lower row are experimental results by van Steijn *et al.* [118].

or expansion stage, where the bubble enters and fills the main channel distorting the fully developed pattern. $T/T_c = 0.75$ illustrates the squeezing stage, where the gas has completely blocked the main channel and is being pushed along. At this time, the velocity direction in the experiments tends to be mainly along the main channel and the velocity at the gas-liquid interface is diverging. However, for the simulation results the y-component of the velocity has a different behavior depending on the elevation in the channel. In the lower half of the channel, the y-component tends to vanish, leaving the velocity to be predominantly in the x-direction. In the upper half, the velocity vectors have a propensity of being perpendicular to the interface, therefore their direction is continuously changing. One of the main sources of this discrepancy is that the simulation is performed in $2D$, which does not account for the flow in the corners of the channels. According to van Steijn *et al.* [118, 119] flow in the corners is an essential component which affects the evolution of the bubble and enhances the collapse and pinch-off process. In addition, it was shown that the velocity at the corners and length of the gas thread are related quantities. $T/T_c = 1.0$ presents the final stage of the process, the pinch-off, where the neck of the thread is reduced to a minimum and the bubble detaches. At this time, the velocity vectors are directed to the position, where the pinch-off takes place, which corresponds to the edge of the tee.

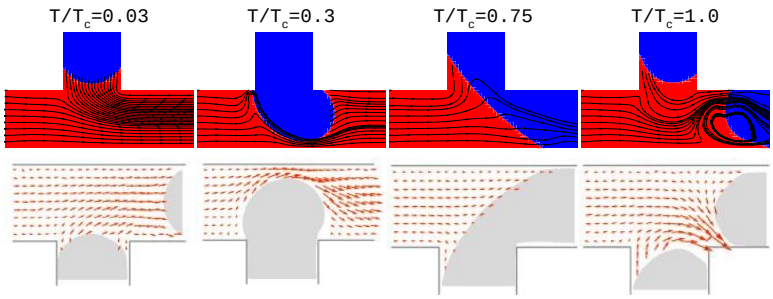

Figure 7.12: Comparison of velocity field in the formation process for ethanol and air and $Q = 1.5$. Top presents the simulation results and lower row are experimental results by van Steijn *et al.* [118].

7.4.2 Evolution of W_m

W_m represents the maximum width that the gas stream will reach at the tee section. The evolution of W_m provides a more quantitative description of the growth of the gas thread in the main channel and its subsequent collapse until pinch-off takes place. Fig 7.13 provides the evolution of W_m comparing the experimental and simulation results. From this graph it can be seen that the maximum value of W_m is around 0.5 for both experimental and numerical solutions. Numerically, this maximum value of W_m is reached faster, around $T/T_c = 0.275$ compared to $T/T_c = 0.4$ for the experimental result. In addition, the numerical evolution has a more rapid expansion and collision process, which is represented by the steepness of the slope. The difference in the evolution of W_m between experimental and simulation results is expected since the simulation is a $2D$ representation of the experimental case.

7.4.3 Final shape and Dimension of Bubble

The case used in the experimental study corresponds to the squeezing regime. Garstecki *et al.* [22] showed that in this regime, the size of the bubble is solely effected by the value of the volumetric flow ratio Q. The length of the bubble is non-dimensionalized by the height of channel H, and is given by the relation $L_{bu}/H = \alpha_1 + \alpha_2 Q$, where the constants $\alpha_{1,2}$ are in the order of unity and depend on the geometry of the channel.

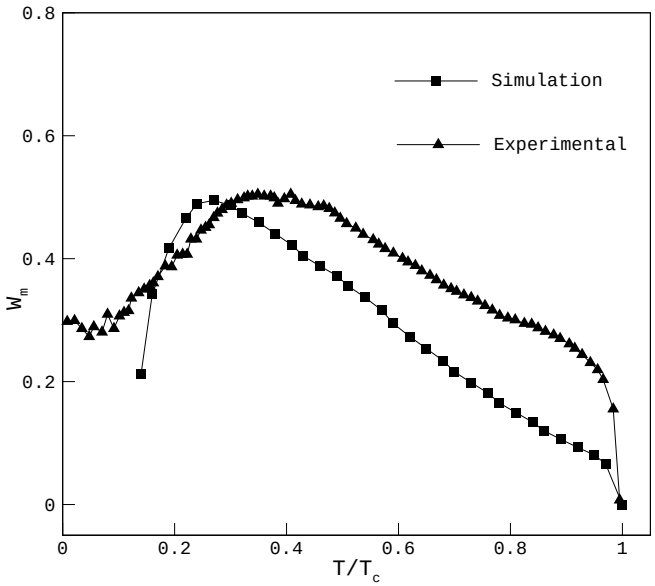

Figure 7.13: Comparison of evolution of W_m for experimental results by van Steijn *et al.* [118] and simulated results for ethanol and air and $Q = 1.5$.

Using $Q = 1.5$ and $\alpha_1 = \alpha_1 = 1.5$ as given by van Steijn *et al.* [118], the theoretical value of the length of the bubble is $L_{bu}/H = 3.75$. Simulation results for the length of the bubble is $L_{bu}/H = 3.94$ which indicates that the percent difference is around 5%. In conclusion, similarity of simulation results with the experimental case provide a good level of confidence of the capabilities of the numerical model to represent the formation process in a T-junction.

7.5 Numerical Results

The parameters which are needed to fully describe the $2D$ T-junction problem are the fluid dynamic viscosities (η_d and η_c), mean speeds of the fluids set at each entrance (v_d and v_c), and the interfacial tension σ. These parameters can be combined into four non-dimensional groups; namely capillary number $Ca = \eta_c v_c/\sigma$, Reynolds number $Re = \rho v_c H/\eta_c$, viscosity ratio $\lambda = \eta_d/\eta_c$, and flow rate ratio $Q = Q_d/Q_c = v_d/v_c$. In general, the formation process of a droplet or bubble in a microchannel with a

T-junction mixing geometry is determined by the balance of the forces. There are two primary forces, the interfacial and viscous forces. By varying the values of Ca, Q, Re, and λ the influence of these forces will be affected. Considering cases with small constant values of Re, leaves only Ca, λ, and Q as governing factors. The following sections will explore the effect that each of these non-dimensional numbers has on the formation process of droplets and bubbles.

7.5.1 Droplet Formation

Effect of Ca

In order to capture the effect of Ca, five different cases were performed using $Ca = 0.005$, $Ca = 0.01$, $Ca = 0.05$, $Ca = 0.1$, and $Ca = 0.5$ at constant $Q = 0.25$, $\lambda = 1.0$ and $\theta_{eq} = 150°$. The final shapes of these simulations are presented in Fig. 7.14. Numerically, varying the value of Ca represents a change of the value of surface tension, while the other values are maintained constant. From these plots, two formation regimes can be identified based on the value of Ca. Cases with low Ca, belong to the squeezing regime. It is noticed that for this regime the dispersed fluid enters the channel and creates a droplet that plugs the continuous flow. The droplet starts moving as it is pushed or squeezed by continuous fluid. For these cases, break-up does not occur since the viscous force is not large enough to overcome the interfacial tension. Previous studies have determined that formation of the droplet in this regime is only proportional to the value of Q. However, as it will be discussed in the following sections, viscosity ratio also plays an important role in the formation process. Garstecki *et al.* [22] determined that viscous forces start playing an important role in the droplet formation, when $Ca > 0.01$. Cases with higher Ca values belong to the dripping regime. As the dispersed fluid enters the channel, the continuous fluid starts pushing it, not allowing a plug to be formed. This fluid is confined to the upper wall of the channel, where shear stress starts acting and inducing the break-up process.

It is important to quantify the effect that Ca has on the pinch-off process. This is done by evaluating how long it takes for the droplet to pinch-off (T_p) and how

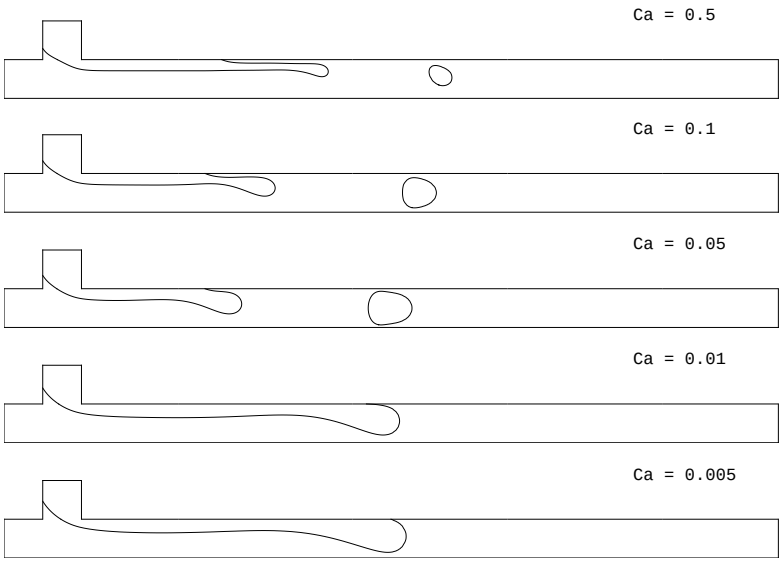

Figure 7.14: Effect of Ca on droplet formation for $Ca = 0.5$, $Ca = 0.1$, $Ca = 0.05$, $Ca = 0.01$, and $Ca = 0.005$ with $Q = 0.25$, $\lambda = 1$, and $\theta_{eq} = 150°$ at $T = 7.5$.

far from the tee this process takes place (D_p). Figs. 7.15a and 7.15b present the relationship between T_p and D_p with Ca. From these plots it can be seen that T_p decreases and D_p increases with higher value of Ca. This indicates that the dispersed fluid is moving farther along the main channel as Ca increases, since there is a higher viscous force exerted on the system. Increase in viscous force also induces pinch-off, therefore T_p is smaller for high values of Ca. Ca also affects the size of the dispersed fluid stream and consequently the size of the droplet. This effect is quantified by examining the evolution of W_m and the final non-dimensional length of the droplet (L_{dr}/H). Fig. 7.16a shows that Ca has a significant affect on the evolution of W_m. The maximum value of W_m is higher as Ca decreases. This indicates that for lower Ca the dispersed fluid tends to occupy more space in the tee area before moving along the main channel. It also illustrates that the expansion and collapse rates are higher for low Ca. Interestingly, the value of Ca does not affect the final value of W_m. On the other hand, Fig. 7.16b shows that length of the droplet decreases as the value of Ca goes up. All these findings are consistent with previous studies [120, 122].

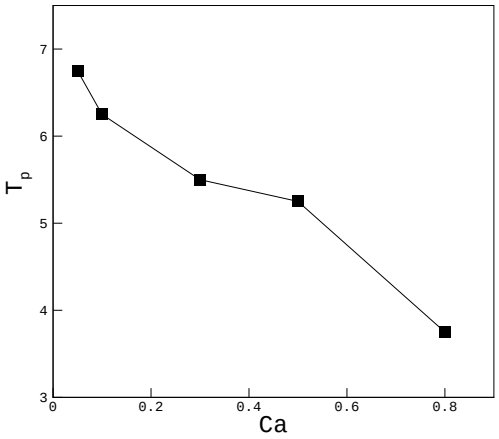

(a) Effect of Ca on T_p.

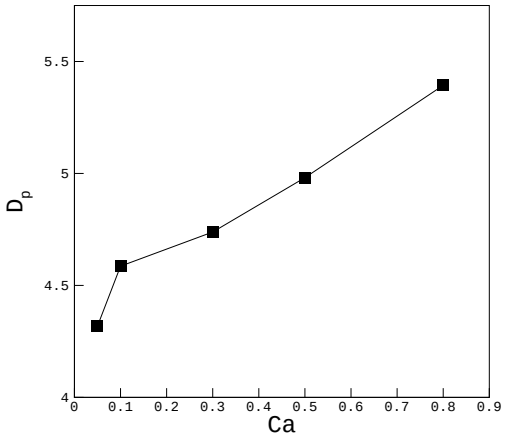

(b) Effect of Ca on D_p.

Figure 7.15: Effect of Ca on (a) T_p and (b) D_p for cases in the dripping regime with $Q = 0.25$, $\lambda = 1$ and $\theta_{eq} = 150°$.

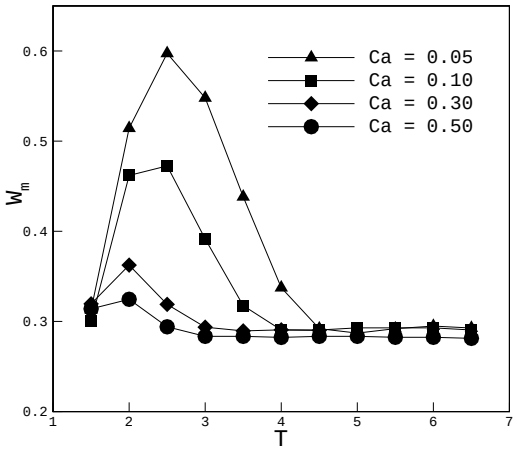

(a) Effect of Ca on W_m.

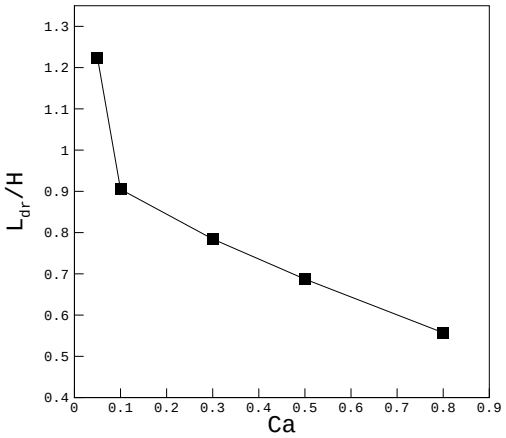

(b) Effect of Ca on L_{dr}/H.

Figure 7.16: Effect of Ca on (a) W_m and (b) L_{dr}/H for cases in the dripping regime with $Q = 0.25$, $\lambda = 1$ and $\theta_{eq} = 150°$.

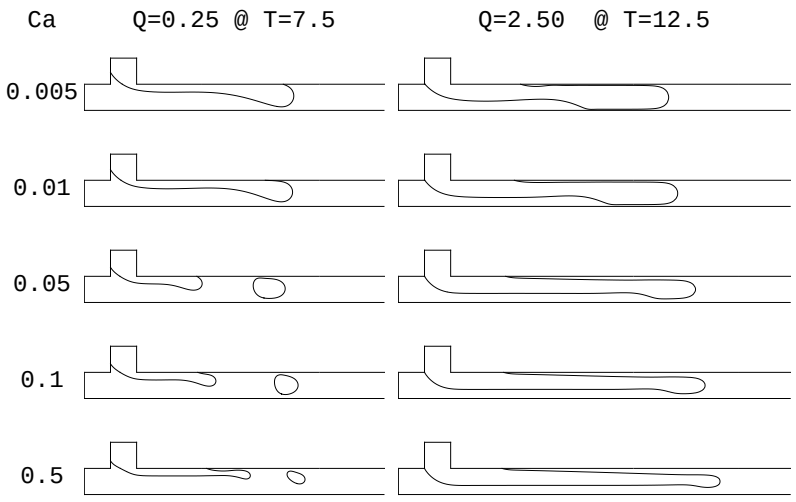

Figure 7.17: Effect of Q on droplet formation for $Q = 0.25$ and $Q = 2.5$ with $Ca = 0.005$, $Ca = 0.01$, $Ca = 0.05$, $Ca = 0.1$, and $Ca = 0.5$ for $\lambda = 1$, and $\theta_{eq} = 150°$ at $T = 7.5$.

Effect of Q

Evaluating the effect of Q is performed by comparing two values $Q = 0.25$ and $Q = 2.5$ with all the values of Ca introduced in previous section, and $\lambda = 1.0$ and $\theta_{eq} = 150°$. Results for final shapes are presented in Fig. 7.17. In general, it can be noticed that modifying the value Q has an effect on both regimes, squeezing and dripping. As the value of Q decreases the void fraction increases and size of the droplet decreases. In the squeezing regime, increasing Q creates a bigger plug which blocks the channel, therefore delaying or even hindering the break-up process. At this point, there is not enough pressure to promote the break-up, therefore the plug keeps on growing and moving as it is squeezed by the continuous fluid. In the dripping regime, increasing Q creates a more elongated thread. Shear stress is not high enough to induce break-up, so the stream continues flowing along the main channel. These findings are consistent with previous experimental and numerical studies [23, 113, 121].

Effect of λ

In order to evaluate the effect of λ, three values are used $\lambda = 0.1$, $\lambda = 0.5$, and $\lambda = 1.0$ with all the values of Ca introduced in previous sections, and $Q = 0.25$ and $\theta_{eq} = 150°$. Final shape for these cases are presented in Fig. 7.18. Note that as the value of λ decreases, the viscous effect exerted by the continuous flow increases. In general, the higher effect can be seen in two different ways: as the dispersed fluid encounters more resistance, it takes longer to enter the channel and to start formation process. And, once the dispersed fluid is in the channel, it experiences a higher shear stress. Therefore, it is stretched further and faster along the continuous flow direction. In addition, increasing the viscous forces enhances the formation process. As can be seen in the cases in the squeezing regime, a droplet is formed when $\lambda = 0.1$. Previous studies indicated that the formation process in the squeezing regime is mainly controlled by the value of Q, [22, 113, 120]. However, these results show that λ is also an important factor in the droplet formation process.

For cases in the dripping regime, the droplets pinch-off faster and closer to the tee as λ is decreased. This is better illustrated in Figs. 7.19a and 7.19b, which shows the effect of λ on T_p and D_p. In general, value of T_p rises and D_p drops as Ca increases for all values of λ, which is consistent with findings in the previous section. This indicates that the value of λ does not affect the relationship between Ca and T_p or D_p. In addition, it can be seen that T_p and D_p become smaller with λ, which shows that there is a higher viscous force in the system that enhances the pinch-off process. Fig. 7.20a shows that λ has little effect on the expansion and collapse time as described in the evolution of W_m. However, the final value of W_m increases with λ. Fig. 7.20b illustrates the effect of λ on the non-dimensional length of the droplet. It is noticed that at low Ca, L_{dr}/H decreases with λ. However, the opposite relation is seen with large Ca.

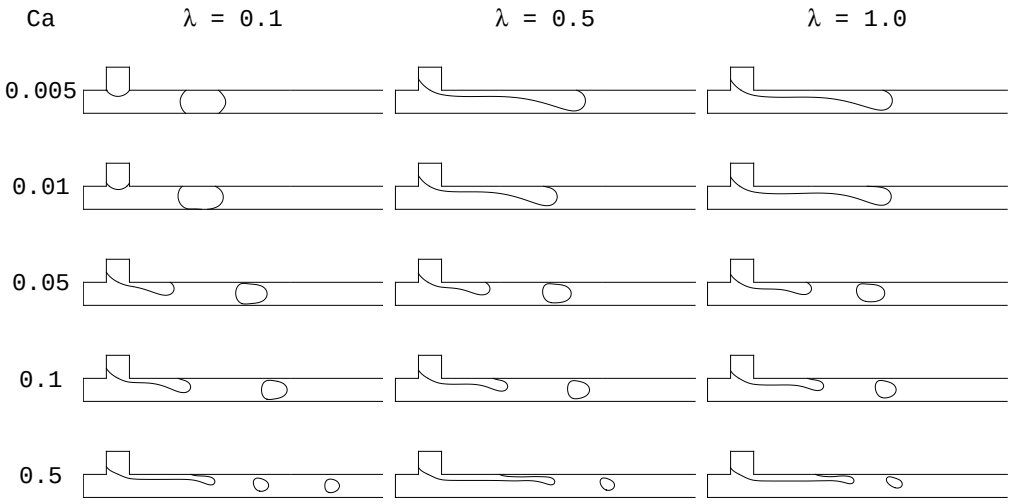

Figure 7.18: Droplet formation for $Ca = 0.005$, $Ca = 0.01$, $Ca = 0.05$, $Ca = 0.1$, and $Ca = 0.5$. $Q = 0.25$, $\lambda = 0.5$, and $\theta_{eq} = 150^{\circ}$ at $T = 7.5$.

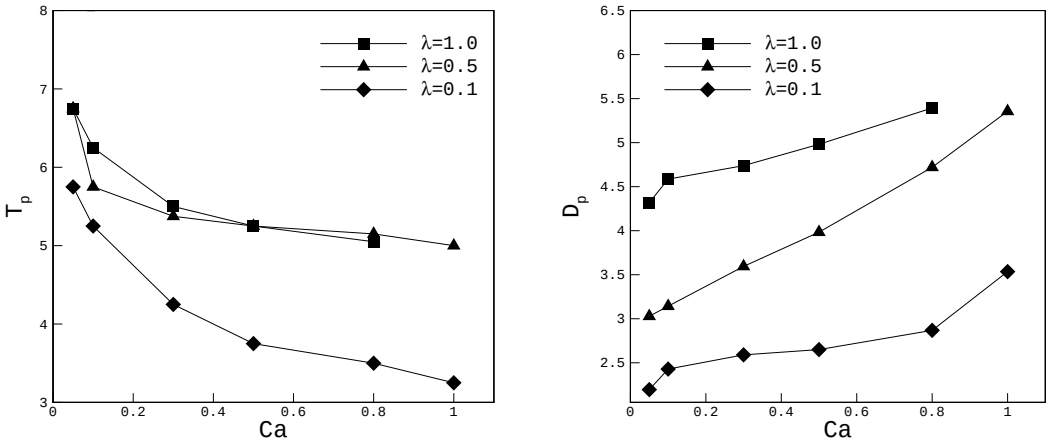

(a) Effect of λ on T_p.

(b) Effect of λ on D_p.

Figure 7.19: Effect of λ on (a) T_p and (b) D_p for cases in the dripping regime with $Q = 0.25$, $\lambda = 1$ and $\theta_{eq} = 150^{\circ}$.

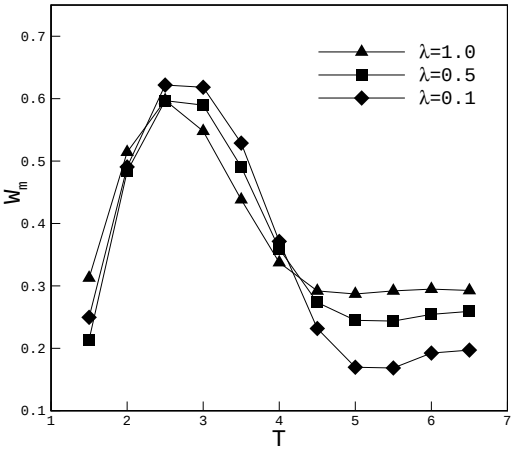

(a) Effect of λ on W_m.

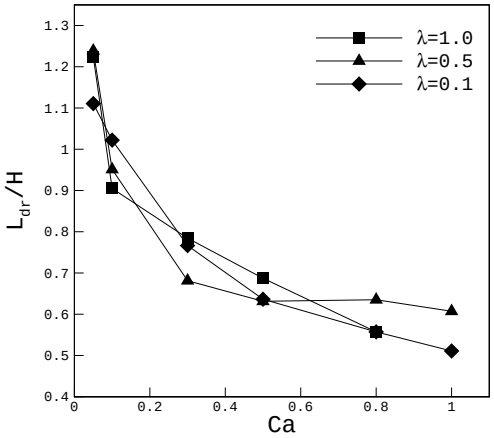

(b) Effect of λ on L_{dr}/H.

Figure 7.20: Effect of λ on (a) W_m and (b) L_{dr}/H for cases in the dripping regime with $Q = 0.25$, $\lambda = 1$ and $\theta_{eq} = 150°$.

7.5.2 Bubble Formation

Effect of Ca

In order to capture the effect of Ca, five different cases were performed for bubble formation using $Ca = 0.005$, $Ca = 0.01$, $Ca = 0.1$, $Ca = 0.5$, and $Ca = 1.0$ at constant $Q = 1.0$, $\lambda = 0.02$, and $\theta_{eq} = 30°$. Fig 7.21 shows that by varying the value of Ca three different regimes can be obtained: squeezing, dripping, and jetting. The squeezing regime corresponds to $Ca < 0.01$ [22]. The cases presented in this regime show that the length of the bubble decreases as the value of Ca increases. This is consistent with the finding presented for the liquid-liquid system. The dripping and jetting regimes are for higher values of Ca, however an established critical value of Ca has not yet been determined. In this study, $Ca \sim 0.1$ is used as a transition value between these two regimes. This value is selected by comparing the features of the final shapes of high Ca cases. For $Ca = 0.1$ the gas stream is thicker than for $Ca > 0.5$. In addition, the tip of the stream for $Ca = 0.1$ has a shape of the bullet, juxtaposed to the tear like shape for other cases. The cases presented in the dripping or jetting regime do not present any break-up. This means that the shear force is not

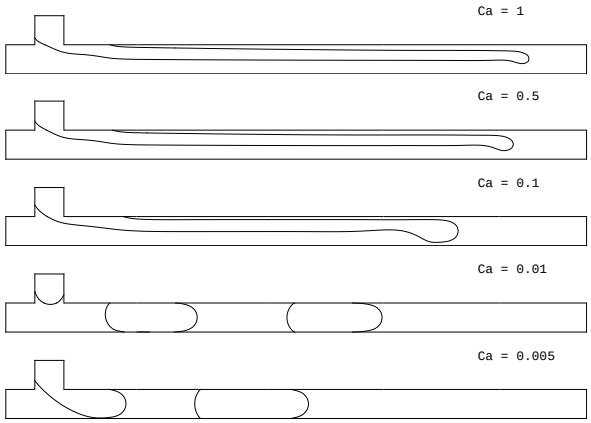

Figure 7.21: Effect of Ca on bubble formation for $Ca = 1.0$, $Ca = 0.5$, $Ca = 0.1$, $Ca = 0.01$, and $Ca = 0.005$ with $Q = 1.0$, $\lambda = 0.02$, $\rho_{ratio} = 0.001$, and $\theta_{eq} = 30°$ at $T = 18.0$.

high enough to overcome surface tension.

Effect of Q

In order to evaluate the effect of Q, four different values were tested for a case in each regime. Fig. 7.22 shows the effect of Q for the squeezing regime at $Ca = 0.005$ by comparing $Q = 0.5$, $Q = 1.5$, $Q = 3.0$, and $Q = 4.5$. As described previously and as shown in the plot, this regime is mainly dominated by the value of Q. As Q decreases, the size of the bubble becomes smaller and the flow becomes bubblier. In addition, the length of the bubble can be estimated by the value of Q [22]. The scaling law introduced in section 7.4 for the non-dimensional length of the bubble, $L_{bu}/H = \alpha_1 + \alpha_2 Q$, where $\alpha_1 = \alpha_1 = 1.5$ [118] is used to compare the simulation results obtained for different Q. The results of this comparison is presented in Fig. 7.23, which shows a good agreement between simulation results and scaling law.

Figs. 7.24 and 7.25 illustrate the effect of Q for dripping and jetting regimes at $Ca = 0.05$ and $Ca = 0.1$ respectively, using $Q = 0.3$, $Q = 0.5$, $Q = 1.0$, and $Q = 3.0$. Results in both regimes indicate that reduction of Q reduces the size of the bubble and increases void fraction. In both regimes, break-up tends to take place when the value of $Q < 0.5$.

Figure 7.22: Effect of Q on bubble formation in the squeezing regime for $Q = 0.5$, $Q = 1.5$, $Q = 3.0$, and $Q = 4.5$ with $Ca = 0.005$, $\lambda = 0.02$, $\rho_{ratio} = 0.01$, and $\theta_{eq} = 30^{\circ}$ at $T = 18.0$.

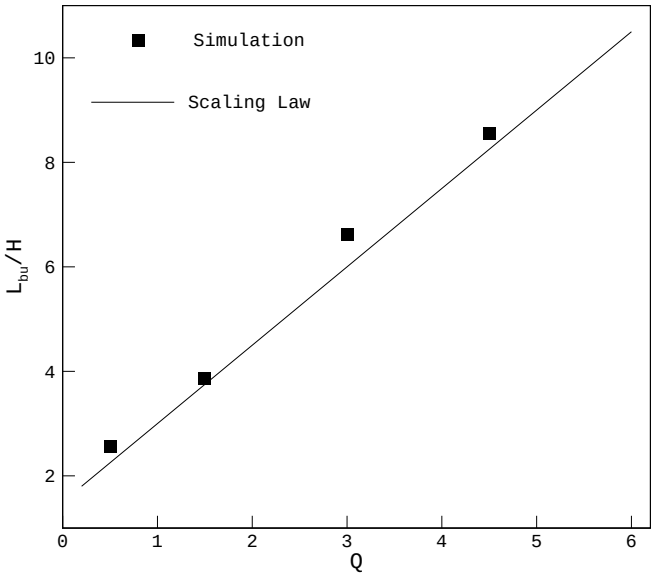

Figure 7.23: Effect of Q on the non-dimensional length of the bubble in the squeezing regime with $Ca = 0.005$, $\lambda = 0.02$, $\rho_{ratio} = 0.01$, and $\theta_{eq} = 30^{\circ}$ at $T = 18.0$.

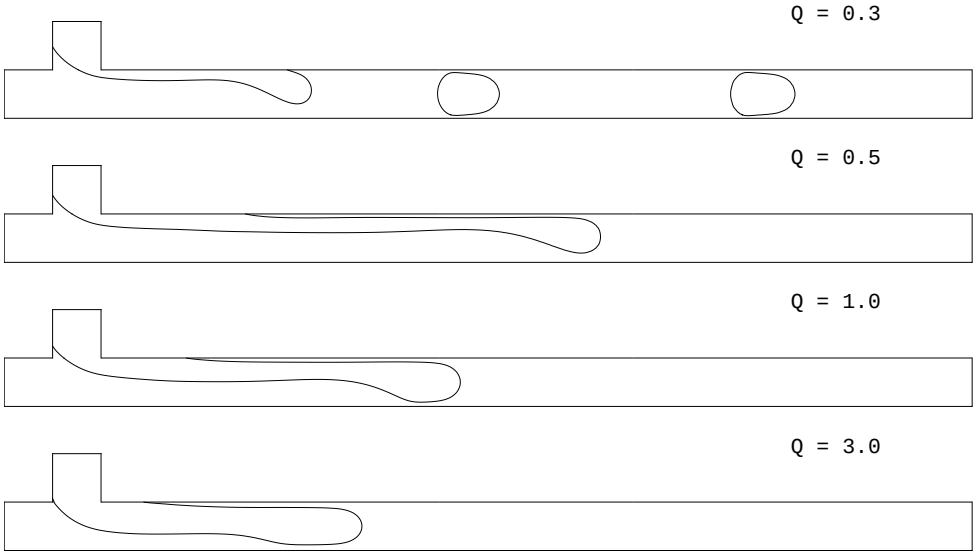

Figure 7.24: Effect of Q on bubble formation in the dripping regime for $Q = 0.3$, $Q = 0.5$, $Q = 1.0$, and $Q = 3.0$ with $Ca = 0.05$, $\lambda = 0.02$, $\rho_{ratio} = 0.01$, and $\theta_{eq} = 30°$ at $T = 18.0$.

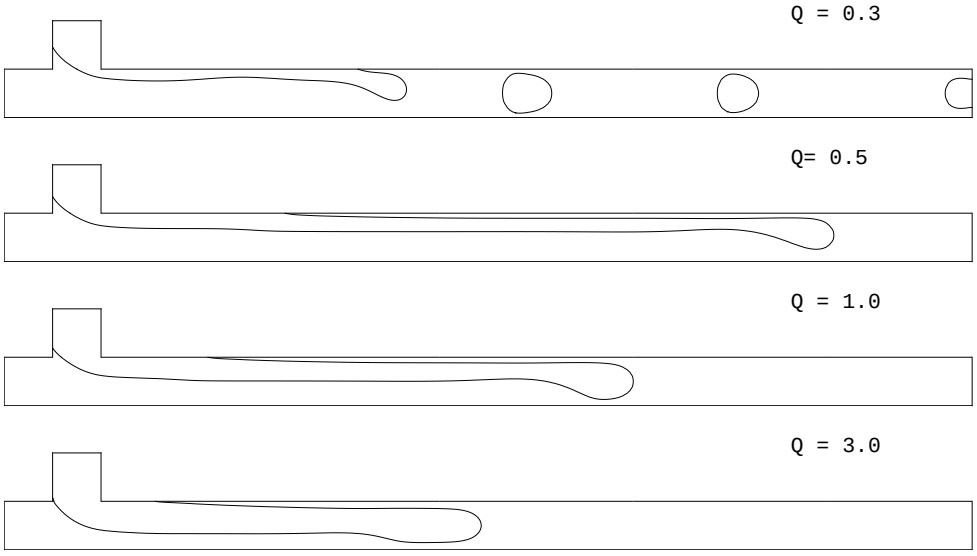

Figure 7.25: Effect of Q on bubble formation in the jetting regime for $Q = 0.3$, $Q = 0.5$, $Q = 1.0$, and $Q = 3.0$ with $Ca = 0.5$, $\lambda = 0.02$, $\rho_{ratio} = 0.01$, and $\theta_{eq} = 30°$ at $T = 18.0$.

Figure 7.26: Effect of λ on bubble formation in the squeezing regime for $\lambda = 1.0$, $\lambda = 0.1$, $\lambda = 0.05$, and $\lambda = 0.02$ with $Ca = 0.005$, $Q = 0.5$, $\rho_{ratio} = 0.001$, and $\theta_{eq} = 30^{\circ}$ at $T = 18.0$.

Effect of λ

In order to evaluate the effect of λ, four values are used $\lambda = 0.02$, $\lambda = 0.05$, $\lambda = 0.1$, and $\lambda = 1.0$ with the three values of Ca used in the previous section. Garstecki *et al.* [22] showed that in the squeezing regime, the size of the bubble is solely effected by the value of the volumetric flow ratio Q. Therefore, change on λ is expected to have little nor no affect in the formation process. This assumption is validated by the results presented in Fig. 7.26, which shows that neither the size of the bubbles, their position, or their frequency is affected by the value of λ. A different result was obtained for the liquid-liquid system in the previous section. In this system, reduction of λ enhances the break-up process, by increasing the effect of shear forces. This indicates that λ has a greater affect in the formation of a droplet rather than of a bubble for low Ca.

Evaluation of λ in the dripping and jetting regime is performed using the values of Ca from the previous section with $Q = 0.3$ and $Q = 0.5$. These values of Q were selected to see how λ affect flows with and without break-up. Figs. 7.27 and 7.29

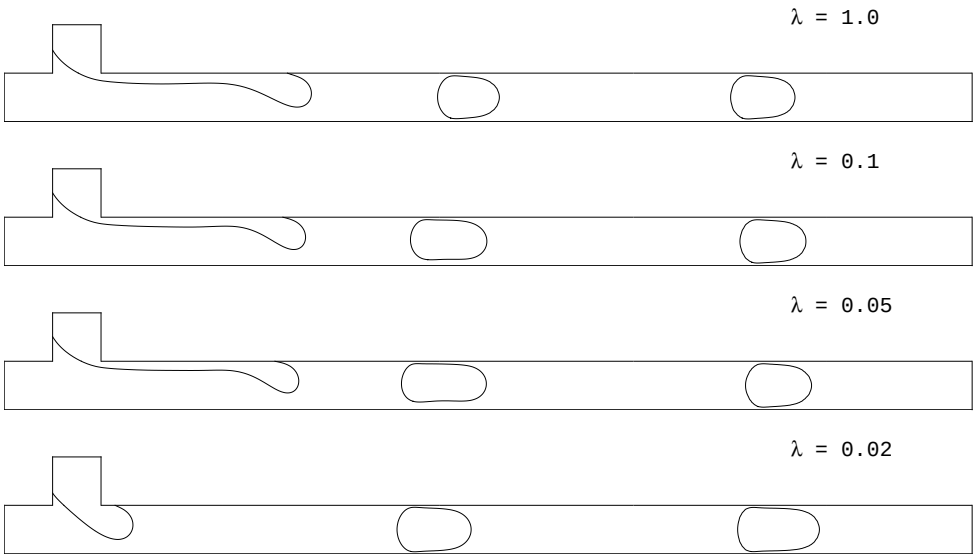

Figure 7.27: Effect of λ on bubble formation in the dripping regime for $\lambda = 1.0$, $\lambda = 0.1$, $\lambda = 0.05$, and $\lambda = 0.02$ with $Ca = 0.05$, $Q = 0.3$, $\theta_{eq} = 30^{\circ}$ at $T = 18.0$.

present the effect λ for the dripping and jetting regimes respectively with $Q = 0.3$. As can be seen from these plots, changing value of λ does not have a great effect on the frequency and the void fraction of the flow. However, the size of the bubble tends to increase as λ decreases. Figs. 7.28 and 7.30 shows that the value of λ has very little effect on the final shape of the flows. In the case of the dripping regime, the slug at the tip of the flow tends to decrease with λ. In general, it can be seen that the change of λ in less significant in the gas-liquid systems compared with liquid-liquid systems.

7.6 $3D$ Results

After a comprehensive $2D$ analysis of the formation of bubbles and droplets in a T-junction, it is necessary to expand this study by simulating the cases in $3D$. It is critical to understand how the physical behavior of the flow changes by transforming the geometry to fully $3D$. Preliminary simulations of droplet formation and bubble formation are performed using $\rho_{ratio} = 1$ and $\lambda = 1$. In addition, coarse grid resolution

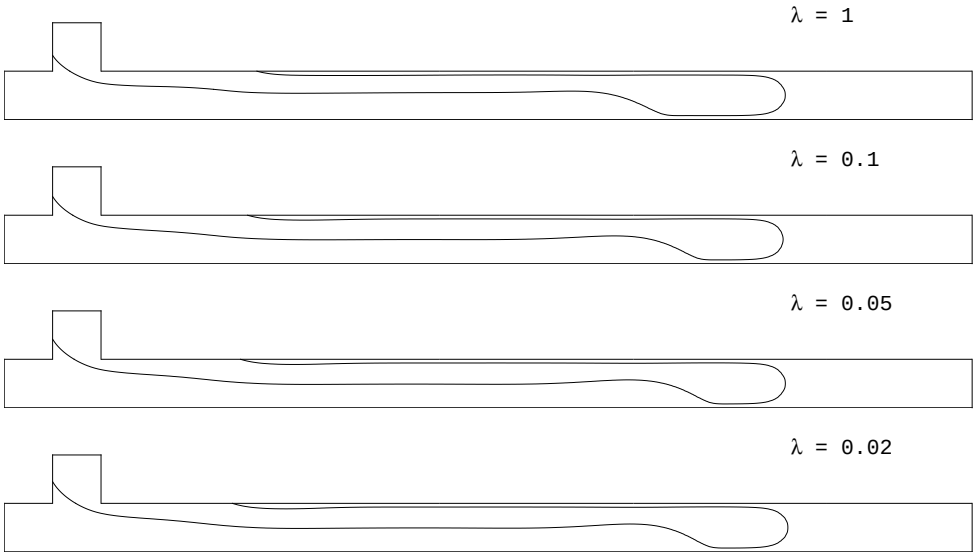

Figure 7.28: Effect of λ on bubble formation in the dripping regime for $\lambda = 1.0$, $\lambda = 0.1$, $\lambda = 0.05$, and $\lambda = 0.02$ with $Ca = 0.05$, $Q = 0.5$, $\theta_{eq} = 30^{\circ}$ at $T = 18.0$.

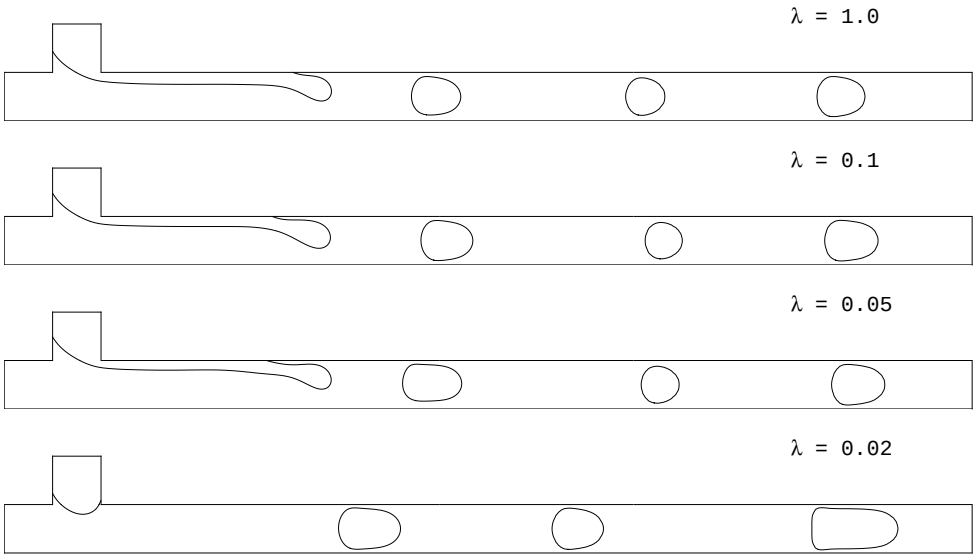

Figure 7.29: Effect of λ on bubble formation in the jetting regime for $\lambda = 1.0$, $\lambda = 0.1$, $\lambda = 0.05$, and $\lambda = 0.02$ with $Ca = 0.5$, $Q = 0.3$, $\theta_{eq} = 30^{\circ}$ at $T = 18.0$.

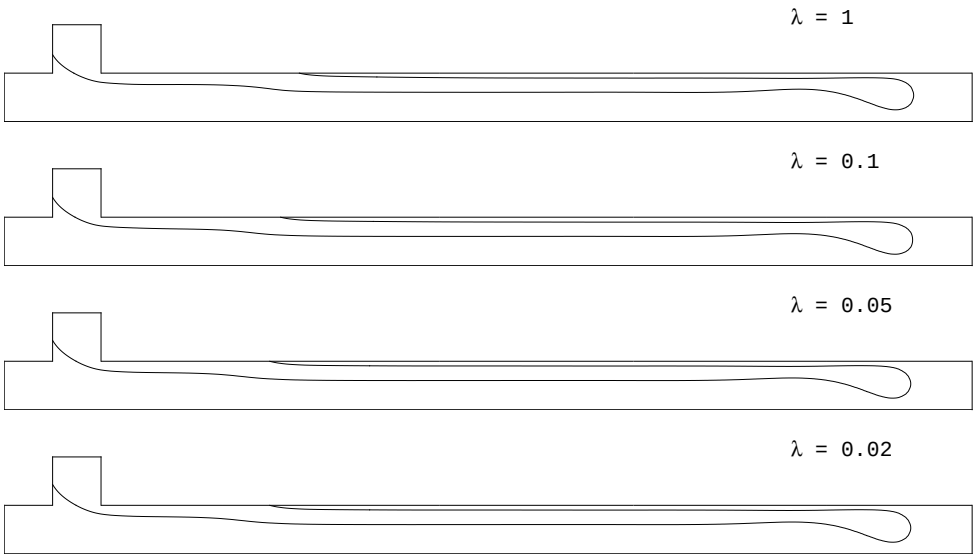

Figure 7.30: Effect of λ on bubble formation in the jetting regime for $\lambda = 1.0$, $\lambda = 0.1$, $\lambda = 0.05$, and $\lambda = 0.02$ for $Ca = 0.5$, $Q = 0.5$, $\theta_{eq} = 30^{\circ}$ at $T = 18.0$.

was used which corresponds to $H = 20$.

7.6.1 Droplet Formation

Simulations of droplet formation are presented in Figs. 7.31 and 7.32 for each of the regimes. These cases correspond to the first and last cases shown in 7.14. For the dripping regime, $Ca = 0.5$, it can be seen that the dispersed fluid enters the channel and the thin thread is pushed along the main channel. The displaced fluid thread has a conical shape, which keeps elongating with time and no droplet formation is shown. In the squeezing regime, $Ca = 0.005$ the disperser fluid thread is thicker than in the dripping case. As the thread enters the main channel starting the expansion stage, W_m increases until it reaches a maximum value. At this point, the collapse stage starts and a neck in the thread starts reducing and ultimately pinch-off takes place. As expected, the behavior of the flow in $3D$ is not exactly the same as $2D$. In general, $3D$ simulations are able to capture the flow around the displaced fluid and on the corners of the channels. The geometrical change will definitively have an impact on the type of flow that will be generated. $3D$ simulations do not capture

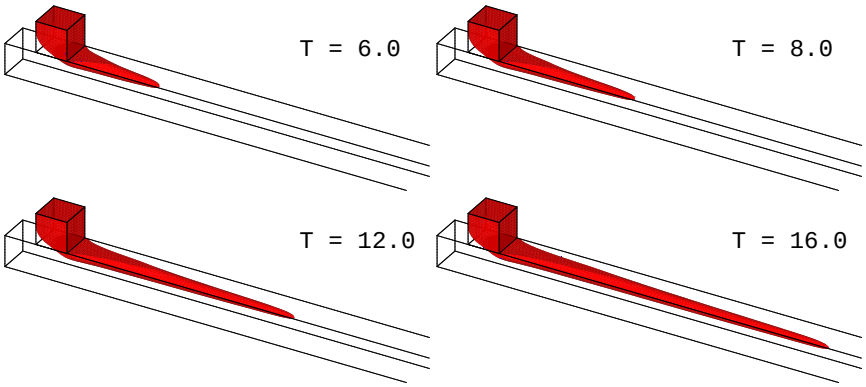

Figure 7.31: $3D$ Simulation for droplet formation for $Ca = 0.5$, $\lambda = 1$, $Q = 0.25$, and $\theta_{eq} = 30°$.

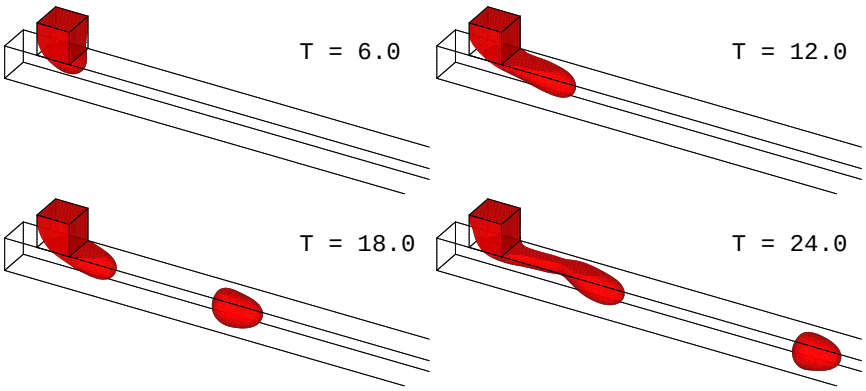

Figure 7.32: $3D$ Simulation for droplet formation for $Ca0.005$, $\lambda = 1$, $Q = 0.25$, and $\theta_{eq} = 30°$.

pinch-off in the dripping regime, however, they do in the squeezing regime. On the other hand, some important features are maintained. The thickness of the dispersed thread is proportional to the value of Ca, which indicates different regime and forces acting on the system.

7.6.2 Bubble Formation

Simulations of bubble formation are presented in Figs. 7.33 to 7.35 for each of the regimes. These cases correspond to the first, third, and last cases shown in 7.21. In the jetting and dripping regimes, $Ca = 1$ and $Ca = 0.01$ respectively, the dispersed fluid

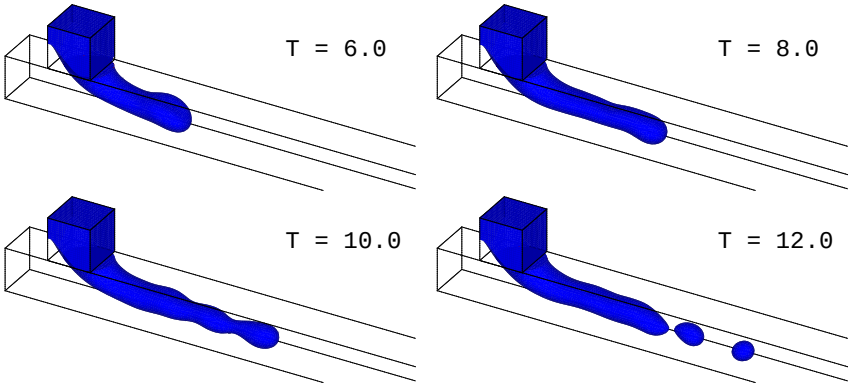

Figure 7.33: $3D$ Simulation for bubble formation at $Ca = 1.0$, $\lambda = 1$, $Q = 1.0$, and $\theta_{eq} = 30°$.

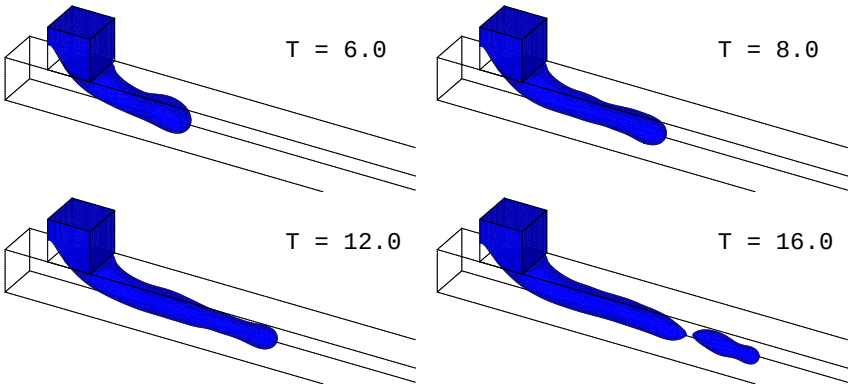

Figure 7.34: $3D$ Simulation for bubble formation at $Ca = 0.01$, $\lambda = 1$, $Q = 1.0$, and $\theta_{eq} = 30°$.

enters the main channel and forms a thread. As this thread is pushed further along the channels, disturbances start affecting the thread and finally pinch-off takes place. It is believed that is disturbances are caused by the Rayleigh-Plateau instability. It is believed, that this instability triggers pinch-off, since the dispersed fluid tends to minimize its surface area. This effect cannot be captured in the $2D$ simulation, which explains why there is not break-up. In the squeezing regime $Ca = 0.005$, the dispersed fluid enters the main channel forming a thicker thread than in the dripping or jetting cases. As the dispersed fluid is pushed along, and necking starts to occur and a bubble forms. This flow differs from the $2D$ simulation on the size of the bubble and thickness of the thread.

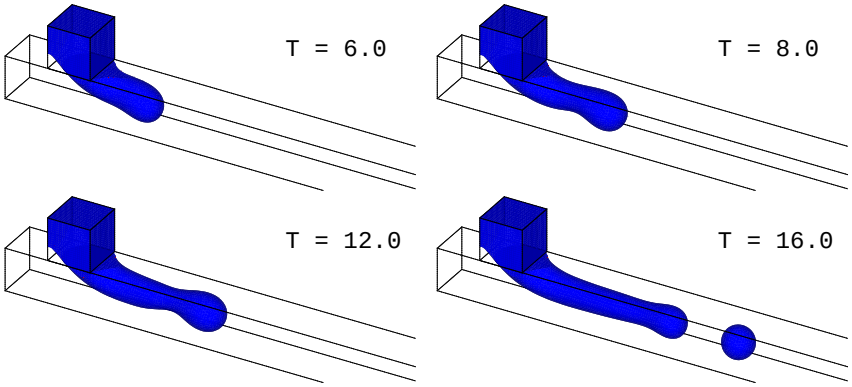

Figure 7.35: $3D$ Simulation for bubble formation at $Ca = 0.005$, $\lambda = 1$, $Q = 1.0$, and $\theta_{eq} = 30°$.

Preliminary $3D$ simulations provide a good starting point to evaluate flow formation in the microchannel. Results showed the ability to capture the droplet and bubble formation process. However, additional analysis has to be performed in order to investigate whether the results are physical or are due to numerical values such as grid resolution, density and viscosity ratios.

Chapter 8

Summary and Future Work

8.1 Summary

Industry is switching to microscales systems, since they can reduce cost, improve safety, and increase efficiency. In general microfluidic devices use single-phase flows, however some specific microfluidic applications, such as chemical synthesis and fluid mixing processes, are now taking advantage of multiphase flows. Introduction of a secondary immiscible flow, creates new recirculation patterns, larger interfaces and additional eddies. These multiphase flows are improving the mixing of reactants and transverse channel transport. In addition, introduction of a secondary flow will allow reduction of common single-phase flow issues, such as long diffusion times and axial dispersion.

Study of multiphase flows in a microreactor could be divided into two main areas: mixing area and segregated area. In the mixing area, mixing geometry and gas-liquid inlet conditions are the most important criteria to determine the type of gas-liquid flow that will be generated. On the other hand, segregated area, is greatly dependent on the interaction between gas, liquid, and solid wall. At this point, the effect of wettability and contact angle would ultimately determine the behavior of the flow.

In order to understand the behavior of multiphase flows in microsystems, this study used LBM as a numerical tool to simulate the dynamics of bubble formation and motion along a microchannel. This study was completed in three different stages:

first, analyze the dynamic behavior of a single bubble as it rises. Second, add the effect of the wall by evaluating a bubble rising in vertical and inclined square channels. Lastly, investigate the formation process in a microchannel for liquid-liquid and gas-liquid systems. The following is a review of the key points obtained in each stage of the study.

Single Bubble Rising in Unconfined Domain

$2D$ analysis is performed in order to establish the dependence on physical and numerical parameters such as density ratio, viscosity ratio, surface tension, interface thickness, and domain size.

- Density ratio has little effect on terminal shape and velocity.
- Viscosity ratio has a large effect on the terminal velocity and shape of the bubble. As viscosity ratio decreases, interface becomes more immobile and shear stress is higher in the system. Therefore, the bubble suffers less deformation and terminal velocity is reduced.
- Increase of Bo reduces the surface tension, therefore higher deformation is exhibited by the bubble.
- Interface thickness has very little to no effect on terminal velocity and shape, as long as the value is high enough to use an isotropic discretization to reduce the parasitic currents in the system.
- Domain size in the radial direction has to be large enough to reduce the wall effect on the dynamics of the bubble.

$3D$ analysis was performed by simulating a case for each of the eight different shape regimes introduced by Bhaga and Weber [53].

- Terminal Re and shape for each case are in good agreement with experimental results.

- Velocity streamlines are given for each case. It was shown that the wake behind the bubble has a dependence on the size, velocity, and deformation of the bubble.
- Pressure contours show that pressure concentrates at the top of the bubble, indicating that the bubble is pushing liquid away in order to continue rising.
- Drag coefficient is calculated using simulation results and it is compared satisfactorily with experimental results.

Single Bubble Rising in a Square Channel

Vertical channel simulations were compared with the experimental results by Li *et al.* [99].

- Simulation results generally agree with the experimental results, except for the evolution of Δ. Experimentally, it was considered that Δ is only a function of k. However, it was found that Δ is also influenced by Ca and We. In addition, a proportional relationship between δ and Ca was established.
- Streamlines and vertical component of vorticity are introduced at different elevation levels of the bubbles to show the different circulation patterns along the flow. It was identified that the change of direction of the vorticity creates complex streamlines. It was shown that the magnitude of the vorticity was reduced as the Ca was increased.

Inclined channel simulations were compared with previous experimental and numerical studies by Zukoski [108], Maneri and Zuber [109] and Shosho and Ryan [110].

- Relationship of δ and Fr at different inclination angles was successfully compared to previous results.
- Streamlines and vorticity contour coupling was not affected by the inclination

Formation Process in a Microchannel

Formation process in a microchannel with a T-junction mixing area was studied for liquid-liquid and gas-liquid systems. It was shown that different non-dimensional parameters such as Ca, Q, ρ_{ratio}, λ, and θ_{eq} have an effect on the formation process in each system.

- Density ratio for the liquid-liquid is considered to be 1. However, in the gas-liquid system this assumption is not valid unless the inertia ratio between the fluids is considerably low.

- Using different values of Ca two different regimes can be identified for the liquid-liquid system, the squeezing and the dripping regimes, where critical value is around $Ca = 0.01$.

- In the gas-liquid system three regimes were identified, the squeezing, the dripping, and jetting regimes. Transition from squeezing to dripping takes place around the same critical Ca for the liquid-liquid system. It was estimated that the transition between dripping and jetting takes place around $Ca = 0.1$.

- In the squeezing regime for the gas-liquid system, the size of the bubble was successfully compared to a scaling law that relates non-dimensional length of the bubble and Q. In addition, it was shown that in this regime, λ has very little effect on the frequency, size or location of the bubble.

- In the squeezing regime for the liquid-liquid system, the formation process is affected by Q and λ. Break-up process is enhanced as both of these values are reduced.

- In the dripping regime for the liquid-liquid system, size of the droplet and pinch-off time are reduced as value Ca increases. In addition, increase of Ca reduces the expansion and collapse rate, as shown in the evolution of W_m.

- Formation process in the dripping and jetting regimes for the gas-liquid system seems to be more influenced by the value of Q rather than λ. This effect is the

opposite to liquid-liquid systems, where reduction of λ enhances the break-up process.

- Surface wettability plays a very important role in the formation process, regardless of the fluids in the system or the value of other non-dimensional factors. As the surface becomes more non-wetting, the dispersed fluid is repelled from the wall thus enhancing the pinch-off process.

8.2 Future Work

The results obtained in the current study are a good starting point, however it could be extended by investigating micro-channel devices with different mixing areas such as cross-section, and co-flowing, with and without symmetrical geometries. In each case, the goal is to identify the different formation regimes and the primary forces that affect the transition from one regime to the next. $3D$ simulation results presented in this study are a foundation to evaluate the effect of the flow in the corners of the pinch-off process, as it was described by previous experimental studies [118, 119]. This effect has to be further examined by performing simulations of each geometry using a $3D$ model. In addition, it is believed that the formation process in the dripping and jetting regimes is triggered by the Rayleigh-Plateau instability. Unfortunately, this instability is completely lost for $2D$ simulations. $2D$ simulations are a good alternative to explore the factors that affect the formation process, however a $3D$ simulation is required to provide a more accurate depiction of the problem. Furthermore, an analysis has to be performed to evaluate the effect of numerical parameters such as grid resolution, density, and viscosity ratio.

Another important factor that has to be explored is the level of contamination or impurities in the system by introducing surface acting agents (Surfactants). Surfactants have the ability of modifying the intermolecular forces, therefore modifying the surface tension of the bubble. However, the addition of surfactants also creates complexities in the simulation of the dynamics of the multiphase flow, since it affects the velocity and the deformation of phases. The advantage of adding surfactants is that

the model will become more realistic and would have a broader range of applications.

Any numerical model always has the possibility for improvement, and it is a never ending task to find alternatives to expand its capabilities and applications. At this point it is necessary to develop numerical schemes that would help overcome some of the limitations of LBM. These limitations include complex enclosure geometries, high velocity and high viscosity ratio cases. Ultimately, the goal is to engage in a cooperative research. This research would focus on the improvement and use of LBM and other numerical tools to explore multiphase models involving different complex phenomena and gas-liquid-solid flows at different scales. Areas that I would like to explore include but are not limited to porous media, bubbly flows, suspensions, boiling, atomization, drop impact, solidification, mixing, energy generation and conservation, biomechanical systems, and heat exchangers.

Appendix A

Modified Particle Distribution Functions

In Eq. (4.9), the modified particle distribution function $\bar{g}_\alpha$ and equilibrium distribution function $\bar{g}_\alpha^{eq}$ are introduced:

$$\begin{aligned}\bar{g}_\alpha \quad &= g_\alpha + \frac{1}{2\tau}(g_\alpha - g_\alpha^{eq}) \\ &-\frac{\delta t}{2}\left(\mathbf{e}_\alpha - \mathbf{u}\right)\cdot\left[\nabla\rho c_s^2\left(\Gamma_\alpha - \Gamma_\alpha(0)\right) - (C\nabla\mu + \rho g\nabla h)\Gamma_\alpha\right] \\ &-\frac{\delta t}{2}\mathbf{e}_\alpha\cdot\left(\rho_l g\nabla h\right)\Gamma_\alpha(0),\end{aligned} \tag{A.1}$$

and

$$\begin{aligned}\bar{g}_\alpha^{eq} \quad &= g_\alpha^{eq} \\ &-\frac{\delta t}{2}\left(\mathbf{e}_\alpha - \mathbf{u}\right)\cdot\left[\nabla\rho c_s^2\left(\Gamma_\alpha - \Gamma_\alpha(0)\right) - (C\nabla\mu + \rho g\nabla h)\Gamma_\alpha\right] \\ &-\frac{\delta t}{2}\mathbf{e}_\alpha\cdot\left(\rho_l g\nabla h\right)\Gamma_\alpha(0).\end{aligned} \tag{A.2}$$

Appendix B

Discretization of First and Second Derivatives

B.1 $D2Q9$ Model

The first derivative can be expressed in terms of grid indices.

$$\begin{aligned} \frac{\partial \phi}{\partial x}|_{(i,j)} = & \quad \left[\phi_{(i+1,j)} - \phi_{(i-1,j)}\right]/\,3 + \left[\phi_{(i+1,j+1)} - \phi_{(i-1,j-1)}\right]/\,12 \\ + & \quad \left[\phi_{(i+1,j-1)} - \phi_{(i-1,j+1)}\right]/\,12 \end{aligned} \tag{B.1}$$

and

$$\begin{aligned} \frac{\partial \phi}{\partial y}|_{(i,j)} = & \quad \left[\phi_{(i,j+1)} - \phi_{(i,j-1)}\right]/\,3 + \left[\phi_{(i+1,j+1)} - \phi_{(i-1,j-1)}\right]/\,12 \\ + & \quad \left[\phi_{(i-1,j+1)} - \phi_{(i+1,j-1)}\right]/\,12 \end{aligned} \tag{B.2}$$

in which i and j are the grid indices in the $x-$ and $y-$direction respectively.

The second derivative is calculated using the following finite difference.

$$\begin{aligned} \frac{\partial^2 \phi}{\partial x_k}|_{(i,j)} = & \quad [\phi_{(i+1,j+1)} + \phi_{(i-1,j+1)} + \phi_{(i+1,j-1)} + \phi_{(i-1,j-1)} \\ + & \quad 4\phi_{(i+1,j)} + 4\phi_{(i-1,j)} + 4\phi_{(i,j+1)} + \phi_{(i,j-1)} - 20\phi_{(i,j)}]/6 \end{aligned} \tag{B.3}$$

B.2 $D3Q19$ Model

The first derivative can be expressed in terms of grid indices.

$$\begin{aligned}\frac{\partial\phi}{\partial x}|_{(i,j,k)} = &\quad \left[\phi_{(i+1,j,k)} - \phi_{(i-1,j,k)}\right]/\,6 + \left[\phi_{(i+1,j+1,k)} - \phi_{(i-1,j-1,k)}\right]/\,12 \\ + &\quad \left[\phi_{(i+1,j-1,k)} - \phi_{(i-1,j+1,k)}\right]/\,12 + \left[\phi_{(i+1,j,k+1)} - \phi_{(i-1,j,k-1)}\right]/\,12 \\ + &\quad \left[\phi_{(i+1,j,k-1)} - \phi_{(i-1,j,k+1)}\right]/\,12\end{aligned} \tag{B.4}$$

$$\begin{aligned}\frac{\partial\phi}{\partial y}|_{(i,j,k)} = &\quad \left[\phi_{(i,j+1,k)} - \phi_{(i,j-1,k)}\right]/\,6 + \left[\phi_{(i+1,j+1,k)} - \phi_{(i-1,j-1,k)}\right]/\,12 \\ + &\quad \left[\phi_{(i-1,j+1,k)} - \phi_{(i+1,j-1,k)}\right]/\,12 + \left[\phi_{(i,j+1,k+1)} - \phi_{(i,j-1,k-1)}\right]/\,12 \\ + &\quad \left[\phi_{(i,j+1,k-1)} - \phi_{(i,j-1,k+1)}\right]/\,12\end{aligned} \tag{B.5}$$

and

$$\begin{aligned}\frac{\partial\phi}{\partial z}|_{(i,j,k)} = &\quad \left[\phi_{(i,j,k+1)} - \phi_{(i,j,k-1)}\right]/\,6 + \left[\phi_{(i+1,j,k+1)} - \phi_{(i-1,j,k-1)}\right]/\,12 \\ + &\quad \left[\phi_{(i-1,j,k+1)} - \phi_{(i+1,j,k-1)}\right]/\,12 + \left[\phi_{(i,j+1,k+1)} - \phi_{(i,j-1,k-1)}\right]/\,12 \\ + &\quad \left[\phi_{(i,j-1,k+1)} - \phi_{(i,j+1,k-1)}\right]/\,12\end{aligned} \tag{B.6}$$

in which i, j, and k are the grid indices in the $x-$,$y-$, and $z-$direction respectively.

The second derivative is calculated using the following finite difference.

$$\begin{aligned}\frac{\partial^2\phi}{\partial x_k}|_{(i,j)} = &\quad [\phi_{(i+1,j+1,k)} + \phi_{(i-1,j-1,k)} + \phi_{(i+1,j-1,k)} + \phi_{(i-1,j+1,k)} \\ + &\quad \phi_{(i+1,j,k+1)} + \phi_{(i-1,j,k-1)} + \phi_{(i+1,j,k-1)} + \phi_{(i-1,j,k+1)} \\ + &\quad \phi_{(i,j+1,k+1)} + \phi_{(i,j-1,k-1)} + \phi_{(i,j+1,k-1)} + \phi_{(i,j-1,k+1)} \\ + &\quad 2\phi_{(i+1,j,k)} + 2\phi_{(i-1,j,k)} + 2\phi_{(i,j+1,k)} + 2\phi_{(i,j-1,k)} \\ + &\quad 2\phi_{(i,j,k+1)} + 2\phi_{(i,j,k-1)} - 24\phi_{(i,j,k)}]/6\end{aligned} \tag{B.7}$$

Bibliography

[1] Gunther A., Kahn S.A., Thalmann M., Trashsel F., Jensen K.F., Transport and reaction in microscale segmented gas liquid. Lab Chip 2004;4:278-286.

[2] Sia S.K., Linder V., Parviz B.A., Siegel A., Whitesides G.M., An integrated approach to a portable low-cost immunoassay for resource-poor settings. Angew. Chem. Int. Ed. 2004;43:498-502.

[3] Nisisako T., Torii T., Higuchi T., Novel microreactors for functional polymer beads. Chem. Eng. J. 2004;101:23-29.

[4] Hessel V., Lowe H., Muller A., Kolb G., Chemical Micro Process Engineering. Germany: Wiley-VCH; 2005.

[5] Burns M.A., Johnson B.N., Brahmasandra S.N., James K.H., Webster R., Krishnan M., Sammarco T.S., Man P.M., Jones D., Heldsinger D., Mastrangelo C.H., Burke D.T., An integrated nanoliter DNA analysis device. Science 1998;282:484-487.

[6] Stride E., Saffari N., Microbubble ultrasound contrast agents: a review. Proc. Instn. Mech. Eng. 2003;217:429-447.

[7] Khan S.A., Gunther A., Schmidt M.A., Jensen K.F., Microfluidic Synthesis of Colloidal Silica. Langmuir 2004;20:8604-8611.

[8] Kapteijn F., Nijhuis T.A., Heiszwolf J.J., Moulijn J.A., New non-traditional multiphase catalytic reactors bases on monolithic structures. Catalysis Today 2001;66:133-144.

[9] Kreutzer M.T., Kapteijn F., Moulijn J.A., Heiszwolf J.J., Multiphase monolith reactors: Chemical reaction engineering of segmented flowin microchannels. Langmuir 2004;20:8604-8611.

[10] Köster S., Angilè F.E., Duan H., Agresti J.J., Wintner A., Schmitz C., Rowat A.C., Merten C.A., Pisignano D., Griffiths A., Weitz D.A., Drop-based microfluidic devices for encapsulation of single cells. Lab Chip 2008;8:1110-1115.

[11] Joshi C.K., Parikh P.A., Application of monolithic stirres reactor in hydrogenation reaction. Indian J. Chem. Technol. 2008;15:572-575.

[12] Buzanowski M.A., Yang R.T., Simple design of monolith reactor for selective catalytic reduction of nitric oxide for power plant emission control. Ind. Eng. Chem. Res. 1990;29:2074-2078.

[13] Avila P., Montes M., Miro E.E., Monolithic reactors for environmental applications. A review on preparation technologies. Chem. Eng. Sci. 2005;109:11-36.

[14] Yeh C.-H., Zhao Q., Lee S.-J., Lin Y.-C., Using a T-junction microfluidic chip for monodispersed calcium alginate microparticles and encapsulation of nanoparticles. Sensors Actuators A: Physical 2009;151:231-236.

[15] Griffiths A., Tawfik D.S., Miniaturising the laboratory in emulsion droplets. TRENDS in Biotechnology 2006;24:395-402.

[16] Nelson G., Application of microencapsulation in textiles. Int. J. Pharm. 2002;242:55-62.

[17] Cubaud T., Ho C.-H., Transport of bubbles in square microchannels. Phys. Fluids 2004;16:4575-4585.

[18] Yu Z., Hemminger O., Fan L.-S., Experiment and lattice Boltzmann simulation of two-phase gas-liquid flows in microchannels. Chem. Sci. Eng. 2007;62:7172-7183.

[19] Shan X., Chen H., Lattice Boltzmann model for simulating flows with multiple phases and components. Phys. Rev. E 1993;47:1815-4327.

[20] Sankaranarayanan K., Shan X., Kevrekidis K., Sundaresan I.G., Analysis of drag and virtual mass forces in bubbly suspensions using an implicit formulation of the lattice Boltzmann method. J. Fluid Mech. 2002;452:61-96.

[21] Gunther A., Jensen K., Multiphase microfluidics: from flow characteristics to chemical and materials synthesis. Lab Chip 2006;6:1487-1503.

[22] Garstecki P., Fuerstman M.J., Stone H.A., Whitesides G.M., Formation of droplets and bubbles in a microfluidic T-junction - scaling and mechanism of break-up. Lab Chip 2006;6:437-446.

[23] Qian D., Lawal A., Numerical study on gas and liquid slugs for Taylor flow in a T-juntion microchannel. Chem. Sci. Eng. 2006;61:7609-7625.

[24] Brackbill J.U., Kothe D.B., Zemach C., A continuum method for modeling of surface tension. J. Comput. Phys. 1992;100:335-354.

[25] Sevilla A., Gordillo J.M., Martinez-Bazan C., Bubble formation in a coflowing air-water stream. J. Fluid Mech. 2005;530:181-195.

[26] Shao N., Salmana W., Gavriilidis A., Angeli P., CFD simulations of the effect of inlet conditions on Taylor flow formation. Int. J. Heat Fluid Flow 2008;29:1603-1611.

[27] Cubaud T., Ulmanella U., Ho C.-H., Two-phase flow in microchannels with surface modifications. Fluid Dyn. Res. 2006;38:772-786.

[28] Lee C.Y., Lee S.Y., Influence of surface wettability on transition of two-phase flow pattern in round mini-channels. Int. J. Multiphase Flow 2008;34:706-711.

[29] Taha T., Cui Z.F., CFD modelling of slug flow inside square capillaries. Chem. Sci. Eng. 2006;61:665-675.

[30] Tseng F.G., Yang I.D., Lin K.H., Ma K.T., Lu M.C, Tseng Y.T., Chieng C.C., Fluid filling into micro-fabricated reservoirs. Sensors Actuators A: Physical 2002;97-98:131-138.

[31] Fang C., Hidrovo C., Wang F.-M., Eaton J., Goodson K., 3-D Numerical simulation of contact angle hysteresis for microscale two-phase flow. J. Multiphase Flow 2008;34:690-705.

[32] Gunstensen A.K., Rothman D.H., Zaleski S., Lattice Boltzmann model of immiscible fluids. Phys. Rev. A 1991;43:4320-4327.

[33] Swift M.R., Orlandini E., Osborn W.R., Yeomans J.M., Lattice Boltzmann simulations of liquid-gas and binary fluid systems. Phys. Rev. E 1996;54:5041-5052.

[34] He X., Luo L., Lattice Boltzmann model for the incompressible Navier-Stokes Equation. J. Stat. Phys. 1997;88:927-944.

[35] Lee T., Lin C.-L., A stable discretization of the lattice Boltzmann equation for simulation of incompressible two-phase flows at high density ratio. J. Comput. Phys. 2005;206:16-47.

[36] He X., Chen S., Zhang R., A lattice Boltzmann scheme for incompressible multiphase flow and its application in simulation of Rayleigh-Taylor instability. J. Comput. Phys. 1999;152:642-663.

[37] Inamuro T., Ogata T., Tajima S., Konishi N., A lattice Boltzmann method for incompressible two-phase flows with large density differences. J. Comput. Phys. 2004;198:628-644.

[38] Inamuro T., Ogata T., Ogino F., Numerical simulation of bubble flows by the lattice Boltzmann method. Future. Gener. Comp. Sy. 2004;20:959-964.

[39] Lee T., Fischer P.F., Eliminating parasitic currents in the lattice Boltzmann equation method for nonideal gas. Phys. Rev. E 2006;74:046709.

[40] Chen S., Doolen G.D., Lattice Boltzmann method for fluid flows. Annu. Rev. Fluid Mech. 1998;30:329-364.

[41] Prosperetti A., Tryggvason G., Computational Methods for Multiphase Flow. New York, NY: Cambrige University Press; 2007.

[42] Succi S., The Lattice Boltzmann Equation. New York, NY: Oxford Science Publications; 2001.

[43] Lee T., Lin C.-L., Chen L.-D., A lattice Boltzmann algorithm for calculation of the laminar jet diffusion flame. J. Comput. Phys. 2006;215:133-152.

[44] Day M.S., Bell J.B., Numerical simulation of laminar reacting flows with complex chemistry. Combust. Theor. Model 2000;4:535-556.

[45] Jacqmin D., An energy approach to the continuum surface tension method. AIAA 1996;96-0858.

[46] Lee T., Effects of incompressibility on the elimination of parasitic currents in the lattice Boltzmann equation method for binary fluids. Comput. Math. Appl. 2009;58:987-994.

[47] Capuani F., Pagonabarraga I., Frenkel D., Discrete solution of the electrokinetic equations. J. Chem. Phys. 2004;121:973-86.

[48] Lee T., Liu L., Lattice Boltzmann simulations of micron-scale drop impact on dry surfaces. J. Comput. Phys. 2010;(229):80458063.

[49] Deckwer W.-D., Bubble column reactors. Chichester: Wiley; 1992.

[50] Blanch H.W., Clark D.S., Biochemical Engineering. New York: Dekker; 1996.

[51] Moshtari B., Babakhani E.G., Moghaddas J.S., Experimental study of gas hold-up and bubble behavior in gas-liquid bubble column. Petroleum and Coal 2009;1:27-32.

[52] Clift R., Grace J.R., Weber M., Bubbles, Drops, and Particles. New York: Academic Press; 1978.

[53] Bhaga D., Weber M.E., Bubbles in viscous liquids: shapes, wakes and velocities. J. Fluid Mech. 1981;105:61-85.

[54] Kurtoglu I.O., Lin C.-L., Lattice Boltzmann study of bubble dynamics. Numer. Heat Transfer, Part B 2006;50:333-351.

[55] Hadamard J.S., Mouvement permanent lent d'une sphre liquide et visqueuse dans une liquide visqueuse. C. R., Acad. Sci. 1911;152:1735-1738.

[56] Rybczynski W., On the translatory motion of a fluid sphere in a viscous medium. Bull. Int. Acad. Pol. Sci. Lett., Sci. Math. Nat. Ser. A 1911;40-46.

[57] Mendelson H.D., The prediction of bubble terminal velocities from wave theory. AIChE J. 1967;13:250-252.

[58] Davies R.M., Sir Taylor G.I., The mechanics of large bubbles rising through extended liquids in tube. Proc R Soc Ser A 1950;200:375-390.

[59] Chen L., Garimella S., Reizes J., Leonard E., The development of a bubble rising in a viscous liquid. J. Comput. Phys. 1999;387:61-96.

[60] Tomiyama A., Celata G.P., Hosokawa S., Yoshida S., Terminal velocity of single bubble in surface tension force dominant regime. Int. J. of Multiphase Flow 2002;28:1479-1519.

[61] Van Sint Annaland M., Deen N.G., Kuipers J.A.M., Numerical simulation of gas bubbles behavior using a three-dimensional volume of fluid method. Chem. Eng. Sci. 2005;60:2999-3011.

[62] Van Sint Annaland M., Dijkhuizen W., Deen N.G., Kuipers J.A.M., Numerical simulation of behavior of gas bubbles using a 3D front-tracking method. AIChE J. 2006;52:99-110.

[63] Bonometti T., Magnaudet J., Transition from spherical cap to toroidal bubbles. Phys. Fluids 2006;33:052102.

[64] Smolianski A., Haario H., Luuka P., Numerical study of dynamics of single bubbles and bubble swarms. Appl. Math. Mod. 2008;32:641-659.

[65] Hua J., Stene J.F., Lin P., Numerical simulation of 3D bubble rising in viscous liquids using a front tracking method. J. Comput. Phys. 2008;227:3358-3382.

[66] Sankaranarayanan K., Shan X., Kevrekidis K., Sundaresan I.G., Bubble flow simulations with the lattice Boltzmann method. Chem. Sci. Eng. 1999;54:4817-4823.

[67] Shan X., Doolen G., Multicomponent lattice Boltzmann model with interparticle interaction. J. Stat. Phys. 1995;81: 379-393.

[68] Shan X., He X., Discretization of the velocity space in the solution of the Boltzmann equation. Phys. Rev. Lett. 1998;8:65-68.

[69] Takada N., Misawa M., Tomiyama A., Fujiwara S., Numerical simulation of two- and three-dimensional two-phase fluid motion by lattice Boltzmann method. Comput. Phys. Commun. 2000;129:233-246.

[70] Hirt C.W., Nichols B.D., Volume of fluid (VOF) method for the dynamics of free boundaries. J. Comput. Phys. 1981;39:201-225.

[71] Frank X., Funfschilling D., Midoux N., Li H.Z., Bubble in a viscous liquid: lattice Boltzmann simulation and experimental validation. J. Fluid Mech. 2006;546:113-122.

[72] Hua J., Lou J., Numerical simulation of bubble rising in viscous liquid. J. Comput. Phys. 2007;222:769-795.

[73] Holdych D.J., Rovas D., Georgiadis J.G., Bukius R.O., An improved hydrodynamics formulation for multiphase flow lattice-Boltzmann models. Int. J. Mod. Phys. C 1998;9:13931404.

[74] Bonometti T., Magnaudet J., An interface-capturing method for incompressible two-phase flows. Validation and application to bubble dynamics. Int. J. Multiphase Flow 2007;33:109-133.

[75] Bunner B., Tryggvason G., Dynamics of homogeneous bubbly flows Part 1. Rise velocity and microstructure of the bubbles. J. Fluid Mech. 2002;466:17-52.

[76] Rodrigue D., Generalized correlation for bubble motion. AIChE J. 2001;47:39-44.

[77] Amaya-Bower L., Lee T., Single bubble rising dynamics for moderate Reynolds number using Lattice Boltzmann method. Comput. Fluids 2010;39:1191-1207.

[78] He X.Y, Chen S., Doolen G.D., A novel thermal model for the Lattice Boltzmann method in incompressible limit. Comput. Phys. 1998;146:282-300.

[79] Qian Y., Chen S., Dissipative and dispersive behaviors of lattice based models for hydrodynamics. Phys. Rev. E 2000;61:2712-2716.

[80] Christopher G.F., Anna S.L., Microfluidic methods for generating continous droplets streams. J. Phys. D. Appli. Phys. 2007;40:R319-R336.

[81] Cubaud T., Tatineni M., Zhong X., Ho C.-H., Bubble dispenser in microfluidic devices. Phys. Rev. E 2005;519:359-376.

[82] Dai L., Cai W., Xin F., Numerical study of bubble formation of a gas-liquid flow in a T-junction microchannel. Chem. Eng. Technol. 2009;32:1984-1991.

[83] Garstecki P., Stone H.A., Whitesides G.M., Mechanins for flow-rate controlled breakup in confined geometries: A route to monodispersed emulsions. Phys. Rev. Lett. 2006;6:437-446.

[84] Sohrabi M., Danesh A., Tehrani D.H., Jamiolahmady M., Microscopic mechanism of oil recovery by near-miscible gas injection. Trans. Porous Med. 2008;72:351-367.

[85] Gauglitz P.A., St. Laurent C.M., Radke C.J., An experimental investigation of gas-bubble in constricted square capillaries. J. Pet. Technol. 1987;39:1137-1146.

[86] Lopes R.J.G., Quinta-Ferreira R.M., CFD modelling of multiphase flow distribution in trickle beds. Chem. Sci. Eng. 2009;147:342-355.

[87] Gaver D.P.I., Halpern D., Jensen O.E., Grotberg J.B., The steady motion of a semi-infinite bubble through a flexible wall channel. J. Fluid Mech. 1996;319:25-56.

[88] Prothero J., Burton A.C., The physics of blood flow in capillaries. I. The nature of the motion. Biophysical J. 1961;1:565-575.

[89] Saisorna S., Wongwises S., A review of two-phase gas-liquid adiabatic flow characteristics in micro-channels. Renew. Sust. Energ. Rev. 2008;1:824-838.

[90] Taylor G.I., Deposition of a viscous fluid on the wall of a tube. J. Fluid Mech. 1961;10:161-165.

[91] Aussillous P., Quéré D., Quick deposition of a fluid on the wall of a tube. Phys. Fluids 2000;12:2367-2371.

[92] Lee T., Lin C.-L., Pressure evolution lattice-Boltzmann-equation method for two-phase flow with phase change. Phys. Rev. E 2003;67:056703.

[93] Liu L., Lee T., Wall free energy based polynomial boundary conditions for non-ideal gas lattice Boltzmann equation. Int. J. Mod. Phys. C 2009;20:1749-1768.

[94] Madal T.K., Das G., Das P., Motion of Taylor bubbles and Taylor drops in liquid-liquid systems. Ind. Eng. Chem. Res. 2008;47:7048-7057.

[95] Qian Y.-H., Chen S.-Y., Dissipative and dispersive behavior of lattice-based models for hydrodynamics. Phys. Fluids A 2000;10:2712-2716.

[96] Thulasidas T.C., Abraham M.A., Cerro R.L., Bubble-train flow in capillaries of circular and square cross section. Chem. Sci. Eng. 1995;50:183-199.

[97] Thulasidas T.C., Abraham M.A., Cerro R.L., Flow patterns in liquids slugs during bubble-train flow inside capillaries. Chem. Sci. Eng. 1997;52:2947-2962.

[98] Clanet C., Heraud P., Searby G., On the motion of bubbles in vertical tubes of arbitrary cross-sections: some complements to the Dumitrescu-Taylor problem. J. Fluid Mech. 2004;519:359-376

[99] Li J., Bulusu V., Gupta N.R., Bouyancy-driven motion of bubbles in square channels. Chem. Sci. Eng. 2008;63:3766-3774.

[100] Bretherton F.P., The motion of long bubbles in tubes. J. Fluid Mech. 1961;10:166-188.

[101] Reinelt D.A., Saffman P.G., The penetration of a finger into a viscous fluid in a channel and tube. J. Sci. Stat. Comput. 1985;6:542-561.

[102] Ratulowski J., Chang H.-C., Transport of gas bubbles in capillaries. Phys. Fluids A 1989;10:1642-1655.

[103] Kolb W.B., Cerro R.L., The motion of long bubbles in tubes of square cross section. Phys. Fluids A 1993;7:1549-1557.

[104] Bugg J.D., Mack K., Rezkallah K.S., A numerical model of Taylor bubbles rising through stagnant liquids in vertical tubes. Int. J. Multiphase Flow 1998;24:271-281.

[105] Yang Z.L., Palm B., Sehgal B.R., Numerical simulation of bubbly two-phase flow in narrow channel. Int. J. Heat Mass Transfer 2002;45:631-639.

[106] Hazel A.L., Heil M., The steady propagation of a semi-infinite bubble into a tube of elliptical or rectangular cross-section. J. Fluid Mech. 2002;470:91-114.

[107] Wong H., Radke J., Morris S., The motion of long bubbles in polygonal capillaries. Part 2. Drag. fluid pressue and fluid flow. J. Fluid Mech. 1995;292:95-110.

[108] Zukoski E.E., Influency of viscosity, surface tension, and inclination angle on motion on long bubbles in closed tubes. J. Fluid Mech. 1966;25:821-837.

[109] Maneri C.C., Zuber N., An experimental study of plane bubbles rising at inclination. Int. J. Multiphase Flow 1974;1:623-645.

[110] Shosho C.E., Ryan M.E., An experimental study of the motion of long bubbles in inclined tubes. Chem. Sci. Eng. 2001;56:2191-2204.

[111] Norman C.E., Miksis M.J., Dynamics of a gas bubble rising in an inclined channel at finite Reynolds number. Phys. Fluids 2005;17:022102.

[112] DeBisschop K.M., Miksis M.J., Eckmann D.M., Bubble rising in an inclined channel. Phys. Fluids 2002;14:93-106.

[113] Xu J.H., Luo G.S., Li S.W., Chen G.C., Shear force induced monodispersed droplet formation in a microchannel device by controlling wetting propertities. Lab Chip 2005;6:131-136.

[114] Nisisako T., Torii T., Higuchi T., Droplet formation in a microchannel network. Lab Chip 2002;2:24-26.

[115] Fu T., Funfschilling D., Ma Y., Scaling the formation of slug bubbles in microfluidic flow-focusing devices. Microfluid Nanofluid 2009;8:467-475.

[116] Christopher G.F., Noharuddin N.N., Taylor J.A., Anna S.L., Experimental observations of the squeezing-to-dripping transition in the T-shaped microfluidic junctions. J. Phys. D. Appli. Phys. 2008;40:R319-R336.

[117] Santos R.M., Kawaji M., Numerical modeling and experimental investigation of gas-liquid slug formation in a microchannel T-junction. Int. J. Multiphase Flow 2009;36:314-323.

[118] van Steijn V., Kleijn C.R., Kreutzer M., Flows around confined bubbles and their importance in triggering pinch-off. Chem. Sci. Eng. 2009;62:7505-7514.

[119] van Steijn V., Kreutzer M., Kleijn C.R., μ-PIV study of the formation of segmented flow in microfluidic T-junctions. Phys. Rev. Lett. 2007;103:214501.

[120] Van der Graaf S., Nisisako T., Schron C.G.P.H., van der Sman R.G.M., Boom R.M., Lattice Boltzmann Simulations of droplet formation in a T-shaped channel. Langmuir 2006;22:4144-4152.

[121] De Menech M., Garstecki P., Jousse F., Stone H.A., Transition from queezing to dripping in a microfludic T-shape junction. J. Fluid Mech. 2008;595:141-161.

[122] Gupta A., Murshed S.M.S., Ranganathan K., Droplet formation and stability of flows in a microfluidic T-juntion. Appl. Phys. Lett. 2009;94:164107.

[123] Wagner A.J., Wilson L.M., Cates M.E., Role of inertia in two-dimensional deformation and breakdown of a droplet. Phys. Rev. E 2003;68:045301.